NOVEL SEMI-CONDUCTOR MATERIAL SYSTEMS: MOLECULAR BEAM EPITAXIAL GROWTH AND CHARACTERIZATION

Nader M. Elmarhoumi, B.S.

Dissertation Prepared for the Degree of

DOCTOR OF PHILOSOPHY

UNIVERSITY OF NORTH TEXAS

December 2013

APPROVED:

Terry D. Golding, Major Professor
Jose M. Perez, Co-Major Professor
Mohammad A. Omary, Committee Member
Yuri V. Rostovtsev, Committee Member
David R. Schultz, Chair of the Department of Physics
Mark Wardell, Dean of the Toulouse Graduate School

Elmarhoumi, Nader. *Novel Semi-Conductor Material Systems: Molecular Beam Epitaxial Growth and Characterization.* Doctor of Philosophy (Physics), December 2013, 138 pp., 14 tables, 70 figures, 90 numbered references.

Semi-conductor industry relies heavily on silicon (Si). However, Si is not a direct-band gap semi-conductor. Consequently, Si does not possess great versatility for multi-functional applications in comparison with the direct band-gap III-V semi-conductors such as GaAs. To bridge this gap, what is ideally required is a semi-conductor material system that is based on silicon, but has significantly greater versatility.

While sparsely studied, the semi-conducting silicides material systems offer great potential. Thus, I focused on the growth and structural characterization of ruthenium silicide and osmium silicide material systems. I also characterized iron silicon germanide films using extended x-ray absorption fine structure (EXAFS) to reveal phase, semi-conducting behavior, and to calculate nearest neighbor distances. The choice of these silicides material systems was due to their theoretically predicted and/or experimentally reported direct band gaps. However, the challenge was the existence of more than one stable phase/stoichiometric ratio of these materials. In order to possess the greatest control over the growth process, molecular beam epitaxy (MBE) has been employed. Structural and film quality comparisons of as-grown versus annealed films of ruthenium silicide are presented. Structural characterization and film quality of MBE grown ruthenium silicide and osmium silicide films via in situ and ex situ techniques have been done using reflection high energy electron diffraction, scanning tunneling microscopy, atomic force microscopy, cross-sectional scanning electron microscopy, x-ray photoelectron spectroscopy, and micro Raman spectroscopy. This is the first attempt, to the

best of our knowledge, to grow osmium silicide thin films on Si(100) via the template method and compare it with the regular MBE growth method. The pros and cons of using the MBE template method for osmium silicide growth are discussed, as well as the structural differences of the as-grown versus annealed films. Future perspectives include further studies on other semi-conducting silicides material systems in terms of growth optimization and characterization.

Copyright 2013

by

Nader M. Elmarhoumi

ACKNOWLEDGEMENTS

First and foremost; All Praise and Thanks be to GOD, THE ONE AND ONLY, without HIS Will, Help, Aid, and Support, nothing is possible. I would then like to deeply thank my beloved Mother, who provided me with the best upbringing, education, and support.

I would like to acknowledge and thank my Respected Committee Members whom I personally consider my dear friends; Prof. Dr. Terry Golding, for his mentorship, continuous dedication, help and support, Prof. Dr. Jose Perez, for his mentorship, heroic efforts, time, and sincere attention. I'm indebted to Prof. Dr. Yuri Rostovtsev, for his mentorship, invaluable support, generous time, and advice. Last, but surely not least, Prof. Dr. Muhammad Omary, for his mentorship, outstanding help, warm and sincere support. I would also like to acknowledge Dr. Golding's research group and collaborators at the University of North Texas – Denton and at Texas State University – San Marcos for their beneficial discussions and training.

I cannot thank enough Dr. Victor Prybutok (UNT's Toulouse Graduate School Associate Dean for Academic Affairs), Dr. Geoffrey Gamble (Senior Vice Provost at that time), and Dr. Jim Meernik (Dean of Toulouse Graduate School at that time), for their kind and sincere support. I will never forget Dr. Prybutok's generous help, and commitment to my success. I consider him my Mentor-at-Large. As for Dr. Gamble, I thank him for the person he is and the personality he has, which indeed is a key reason for reaching this step in my professional life.

I certainly did not mention many people that are important in my life. Therefore, I would like to acknowledge and thank my family, friends, and all those individuals whom in one way or another had a positive impact on me and helped me reach where I am now. Thank you.

TABLE OF CONTENTS

Page

ACKNOWLEDGEMENTS iii

LIST OF TABLES viii

LIST OF ILLUSTRATIONS x

1. PHYSICS OF SEMI-CONDUCTOR SILICIDES 1

1.1 Physical Background, Story, and Motivation 1

1.2 General Material Aspects 6

1.2.1 Fe-Si (β-$FeSi_2$) Semi-conductor Material System 6

1.2.2 Ru-Si (Ru_2Si_3) Semi-conductor Material System 7

1.2.3 Os-Si (Os_2Si_3 and $OsSi_2$) Semi-conductor Material System 9

1.3 Thermodynamics of Silicidation 10

1.3.1 Fe-Si (β-$FeSi_2$) Semi-conductor Material System 11

1.3.2 Ru-Si (Ru_2Si_3) Semi-conductor Material System 14

1.3.3 Os-Si (Os_2Si_3 and $OsSi_2$) Semi-conductor Material System 14

1.4 Kinetics of Silicidation 17

1.4.1 Fe-Si (β-$FeSi_2$) Semi-conductor Material System 17

1.4.2 Ru-Si (Ru_2Si_3) Semi-conductor Material System 18

1.4.3 Os-Si (Os_2Si_3 and $OsSi_2$) Semi-conductor Material System 19

2. ELECTRONIC BAND STRUCTURE OF SEMI-CONDUCTORS 20

2.1 Theoretical Considerations 20

2.2 Fe-Si (β-$FeSi_2$) Semi-conductor Material System 27

2.3 Ru-Si (Ru_2Si_3) Semi-conductor Material System 30

2.4 Os-Si (Os_2Si_3 and $OsSi_2$) Semi-conductor Material System 32

3. TECHNIQUES AND THEIR FOUNDATION 35

3.1 Molecular Beam Epitaxy 35

3.2 Reflection High Energy Electron Diffraction 39

3.3 X-ray Absorption Spectroscopy / X-ray Absorption Fine Structure 41

3.4 Atomic Force Microscopy 46

3.5 X-ray Photoelectron Spectroscopy 50

3.6 Raman Spectroscopy.. 52

3.7 Scanning Tunneling Microscopy 54

3.8 Scanning Electron Microscopy / Cross-sectional Scanning Electron Microscopy 56

4. MOLECULAR BEAM EPITAXIAL GROWTH OF IRON SILICON GERMANIDE AND CHARACTERIZATION.. 58

4.1 Experimental Methods and Equipment.. 58

4.1.1 Molecular Beam Epitaxy (MBE) 58

4.1.2 X-ray Absorption Spectroscopy – X-Ray Absorption Fine Structure......... 60

4.2 Growth of Iron Silicon Germanide Thin Films by MBE 63

4.3 Results and Discussion 65

XAFS of $Fe(Si_{1-x}Ge_x)_2$ thin film samples[84-87] 65

4.4 Conclusions 71

5. MOLECULAR BEAM EPITAXIAL GROWTH OF RUTHENIUM SILICIDE AND CHARACTERIZATION.. 73

5.1 Experimental Methods and Equipment 74
5.1.1 Molecular Beam Epitaxy (MBE) Facility and *In Situ* Characterization Techniques 74
5.1.2 Atomic Force Microscopy (AFM) 76
5.1.3 X-ray Photoelectron Spectroscopy (XPS) 76
5.1.4 Micro Raman Spectroscopy 76
5.2 Molecular Beam Epitaxial Growth and Characterization of Ruthenium Silicide (Ru_2Si_3) on Si (100) 77
5.3 Reflection High Energy Electron Diffraction (RHEED) 78
5.4 *In Situ* Scanning Tunneling Microscopy (STM) 80
5.5 *Ex situ* Cross-sectional Scanning Electron Microscopy (X-SEM) 81
5.6 *Ex situ* Atomic Force Microscopy (AFM) 84
5.7 *Ex situ* X-ray Photoelectron Spectroscopy (XPS) 85
5.8 Micro Raman Spectroscopy 90
6. MOLECULAR BEAM EPITAXIAL GROWTH OF OSMIUM SILICIDE AND CHARACTERIZATION 93
6.1 Template and Regular MBE Growth and Characterization of osmium silicide thin films on Si(100) 94
6.2 Reflection High Energy Electron Diffraction (RHEED) 95
6.3 *In situ* Scanning Tunneling Microscopy (STM) and *In situ* Atomic Force Microscopy 97
6.4 *Ex situ* Cross-sectional Scanning Electron Microscopy (X-SEM) 100

6.5 *Ex situ* Atomic Force Microscopy (AFM) 106

6.6 *Ex situ* X-ray Photoelectron Spectroscopy (XPS) 109

6.7 Micro Raman Spectroscopy 118

7. A BIRD'S EYE VIEW AND SUMMARY OF CONCLUSIONS 121

7.1 Overview 121

7.2 Summary of Analysis 123

7.3 Summary of Conclusions 128

7.4 Significance of Results and Future Implications 129

REFERENCES 132

LIST OF TABLES

Page

Table 1.1 Condensed basic information of the semi-conducting silicides[5], adapted from Borisenko[2] showing the silicides of choice in this work. 5

Table 1.2 Semi-conducting silicides and their germanide counter parts.[2] Many of the silicides are of similar structure and space group as their germanides. 6

Table 1.3 Atomic positions in orthorhombic $FeSi_2$,[6] primitive translation vectors are used. 7

Table 1.4 Nearest-neighbor interatomic distances in units of nm in the orthorhombic β-$FeSi_2$ for *a=0.9863, b=0.7791, c=0.7833 nm*.[2]... 7

Table 1.5 Atomic positions in orthorhombic Ru_2Si_3 (in units of the primitive translational vectors).[8] 9

Table 1.6 Nearest neighbor interatomic distances in orthorhombic Ru_2Si_3, in units of nm, for *a=1.1436 nm, b=0.9238 nm, and c=0.5716 nm.* 9

Table 1.7 Atomic positions in the orthorhombic $OsSi_2$ in units of the primitive translational vectors.[10] 10

Table 1.8 Nearest neighbor interatomic distances in units of nm in orthorhombic $OsSi_2$, for *a=1.014 nm, b=0.811 nm, c=0.822 nm*. 10

Table 1.9 Parameters of thermodynamics of silicidation in the Fe-Si material system. [a]Reference [12]. [b]Reference [7]. [c]Reference [13]. [d]Reference [14] 12

Table 1.10 The growth parameters of Fe-Si material system. * Shows the value from the experimental data in the reference. ** Shows the value by rapid thermal processing 18

Table 2.1 Bang gaps nature and energy value in orthorhombic Ru_2Si_3 32

Table 2.2 Band-gaps nature and energy values of $OsSi_2$ as reported from theoretical calculations and experimental results. 33

Table 4.1 Nearest neighbor distances of $FeSi_2$ phases and iron silicide stoichiometries in comparison with our $Fe(Si_{1-x}Ge_x)_2$ nearest neighbor distances in very close agreement with those of β-$FeSi_2$. 70

Table 4.2 Absorption edge energies (E_0) and nearest neighbor distances (d_{nn}) of *samples x, y, and z,* showing slight increase in the absorption edges of the samples with increasing Ge content. While their nearest neighbor distances slightly decrease with increasing Ge content. 71

LIST OF ILLUSTRATIONS

Page

Figure 1.1 Energy vs. momentum (wave number) showing the indirect band-gap of Si vs. the direct band-gap of GaAs 2

Figure 1.2 Projections of orthorhombic Ru_2Si_3 unit cell on the *xy, xz,* and *yz* planes.[8] The numbers inside the circles indicates the atomic site distance from the plane in the perpendicular direction. 8

Figure 1.3 The phase diagram of the Fe-Si material system.[12] Temperature (^{0}C) vs. Atomic per cent silicon. It shows the complexity and the various phases of the Fe-Si system. 13

Figure 1.4 The phase diagram of the Ru-Si material system.[12] It shows its most stable silicon-rich phase Ru_2Si_3 which crystallizes below 1000 ^{0}C. 15

Figure 1.5 The phase diagram of the Os-Si material system.[12] It shows its three stable phases, namely the disilicide $OsSi_2$, the monosilicide OsSi, and the Silicon-rich Os_2Si_3 phase. 16

Figure 2.1 The energy spectrum of Li from an atom (a), to a molecule (b), to a solid (c)[37]. . 21

Figure 2.2 The distribution of electrons in the bands of (a) a metal, (b) an insulator, and (c) a semiconductor[37]. 23

Figure 2.3 Energy vs. momentum in (a) a direct gap semiconductor and (b) an indirect gap semiconductor with a conduction band valley at k = <000>[39]. 25

Figure 2.4 A direct band gap in which the lowest point in the conduction band is at the same **k**-value as the highest point in the valence band. A direct optical transition

is vertically drawn without any significant change in **k**, since the photon has a very small wave vector. The threshold frequency ω_g for absorption by the direct transition determines the energy gap $E_g = \hbar\omega_g$. The figure and caption are adapted from Kittel[38]. 26

Figure 2.5 An indirect band gap in which the band edges of the conduction and valence bands are widely separated in k-space involve indirect transition which includes a photon as well as a phonon. The threshold energy for the indirect process is greater than the true band gap. The absorption threshold for the indirect transition between the band edges is at $\hbar\omega = E_g + \hbar\,\Omega$ where Ω is the frequency of an emitted phonon of wave vector $\mathbf{K} = -\mathbf{k}_c$. At higher temperatures phonons are already present; if a phonon is absorbed along with a photon, the threshold energy is $\hbar\omega = E_g - \hbar\,\Omega$. The figure and caption is adapted from Kittel[38]. 27

Figure 2.6 The electronic band structure of β-$FeSi_2$ as calculated by the LMTO method,[40] showing the direct/quasi-direct nature of its bandgap. 29

Figure 2.7 (a) The band structures of orthorhombic Ru_2Si_3, as calculated by the LMTO method,[55] showing its clear direct transition at the Γ point. (b) The band structures of orthorhombic Ru_2Ge_3, as calculated by the LMTO method.[55] 31

Figure 2.8 The band structure of $OsSi_2$ as calculated by the LMTO method,[59] showing a direct transition at the Y point. 34

Figure 3.1 A schematic diagram for an MBE growth chamber with one Knudsen effusion cell and one e-beam evaporator[5] 37

Figure 3.2 Schematic diagram of the three primary modes of epitaxial growth: (a) Frank van der Merwe (layer-by-layer), (b) Stranski-Krastanov (layer-plus-island), and (c) Volmer-Weber (island-like growth)). Θ is the number of monolayers (ML)[62] 38

Figure 3.3 RHEED pattern for Si buffer layer during MBE growth illustrating a typical Si 2x1-reconstruction 41

Figure 3.4 The XAS spectrum of pure osmium (Os). The XAS plot shows the absorption versus energy of Os as well as the XANES and the EXAFS regions in the Os XAFS spectrum. 45

Figure 3.5 A Schematic diagram showing the three main AFM modes; (a) Contact mode (static mode), (b) Tapping mode (dynamic mode), and (c) Non-contact mode (also a dynamic mode)[71]. 48

Figure 4.1 State of the art UHV MBE system employed to grow these $Fe(Si_{1-x}Ge_x)_2$ samples is designed by Hans Gossmann and donated by Lucent Technologies..... 59

Figure 4.2 The DCM beam line facility at synchrotron facility of the center for advanced microstructures and devices (CAMD) 61

Figure 4.3 XAFS of $Fe(Si_{1-x}Ge_x)_2$ ($0 \leq x \leq 0.15$) films with different thicknesses without the XAFS of the pure metallic Fe reference. 66

Figure 4.4 XAFS of $Fe(Si_{1-x}Ge_x)_2$ ($0 \leq x \leq 0.15$) films with different thicknesses in comparison with the XAFS of the pure metallic Fe reference. 67

Figure 4.5 The Fourier Transform of the EXAFS of the $Fe(Si_{1-x}Ge_x)_2$ thin films samples without the Fourier Transform of the pure metallic Fe reference. 68

Figure 4.6 The Fourier Transform of the EXAFS of the $Fe(Si_{1-x}Ge_x)_2$ thin films samples with the Fourier Transform of the pure metallic Fe reference. 69

Figure 5.1 The ONR MBE system with Si, Os, and Ru e-beam sources, a Ge effusion cell, and an O plasma source. 75

Figure 5.2 The ONR MBE System is shown in relation to the *in situ* XPS/UPS/AES/LEED analysis chamber, STM/SPM/AFM analysis chamber system, and an oxide MBE system. 75

Figure 5.3 RHEED pattern of diruthenium trisilicide template layer at 800 ^{0}C showing a significant difference in the RHEED pattern reconstruction from a typical Si 2x1 – reconstruction shown in Figure 5.4. 78

Figure 5.4 RHEED pattern of Si after Si buffer layer showing a typical Si 2x1 – reconstruction. 79

Figure 5.5 RHEED pattern of diruthenium trisilicide as-grown film showing three dimensional crystalline growth pattern with symmetry every 90 degree azimuth. 79

Figure 5.6 RHEED pattern of annealed diruthenium trisilicide film showing that the annealed samples appear to regain two dimensional film nature. 79

Figure 5.7 A 2 μm x 2 μm STM image of as as-grown diruthenium trisilicide film showing textured grains of around 0.5 μm in size. 80

Figure 5.8 A 0.5 μm x 0.5 μm STM image of annealed diruthenium trisilicide film a significantly smoother surface with smaller grains in comparison with as-grown film. 81

Figure 5.9 X-SEM of as-grown diruthenium trisilicide showing thicknesses ranging from 25 nm to 125 nm showing hillock-like surface and structure. 82

Figure 5.10 X-SEM of annealed diruthenium trisilicide showing thicknesses around 40 nm showing comparatively smoother surface than the as-grown films. 83

Figure 5.11 AFM of as-grown diruthenium trisilicide films. RMS surface roughness = 22.9 nm 84

Figure 5.12 AFM of annealed diruthenium trisilicide films. RMS Surface roughness = 8.8 nm 85

Figure 5.13 Pre-sputtering stoichiometric ratios and binding energies of as-grown diruthenium trisilicide films showing a bit far ratio of ruthenium to silicon from the desired stoichiometric ratio of 2:3. The oxygen presence and silicon dioxide binding energy peak, clearly indicate that very surface of the films have been oxidized due exposure to air... 86

Figure 5.14 Post-sputtering stoichiometric ratios and binding energies of as-grown diruthenium trisilicide films showing the Ru:Si ratio in close agreement with the desired stoichiometric ratio of Ru_2Si_3. Ar-sputtering is only around 30 A^0 deep. 87

Figure 5.15 Pre-sputtering survey spectrum, stoichiometric ratios and binding energies of annealed diruthenium trisilicide films showing an off Ru:Si ratio in comparison with stoichiometrically desired ratio of 2:3. The oxygen presence and silicon dioxide binding energy peak, clearly indicate that very surface of the films have been oxidized due exposure to air. 89

Figure 5.16 Post-sputtering stoichiometric ratios and binding energies of annealed diruthenium trisilicide films showing the Ru:Si ratio in close agreement with the desired stoichiometric ratio of Ru_2Si_3. Ar-sputtering is also around 30 A^0 deep. 90

Figure 5.17 Micro Raman Spectroscopy of as-grown and annealed diruthenium trisilicide films showing signature peaks at Raman shifts less than 500 cm^{-1}...................... 91

Figure 5.18 A clearer view of the shifts less than 500 cm^{-1} of the Raman Spectroscopy of as-grown and annealed diruthenium trisilicide films showing distinct active Raman shifts from pure Si, at around 190, 220, 235, 370, and 485 cm^{-1}. 91

Figure 6.1 RHEED pattern of as-grown osmium silicide grown by the template method showing 3d-growth and great similarity to that of Ru_2Si_3. Chapter 1 mentions that Ru_2Si_3 and Os_2Si_3 are isostructural[2]. 95

Figure 6.2 RHEED pattern of annealed osmium silicide grown by the template method showing 2d-growth and great similarity with that of annealed Ru_2Si_3 as in the previous chapter. Ru_2Si_3 and Os_2Si_3 are isostructural[2]. 96

Figure 6.3 RHEED pattern of as-grown osmium silicide by the regular method showing three dimensional growth and with distinct difference to typical Si-2x1 RHEED pattern reconstruction.. 96

Figure 6.4 RHEED pattern of annealed osmium silicide grown by the regular method showing streaks revealing that the film regained 2d-growth. However, certainly different from the annealed film grown by the template method. 96

Figure 6.5 A 2 µm x 2 µm *in situ* STM image of as-grown osmium silicide grown by the template method showing hillock-like surface and structure with uniformity for the textured grains. 98

Figure 6.6 A 2 µm x 2 µm *in situ* AFM image of annealed osmium silicide grown by the template method showing an obvious reduction in the size and height of the hillocks together with smaller grain sizes. 98

Figure 6.7 A 2 µm x 2 µm *in situ* AFM image of as-grown osmium silicide grown by the regular method showing more of an island-like growth with less uniformity than the as-grown films by the template method. 99

Figure 6.8 A 2 µm x 2 µm *in situ* AFM image of annealed osmium silicide grown by the regular method showing an overall smoother surface and structure in comparison with the as-grown of the same method. Annealing of films grown by the regular method leads to an overall better quality film. 99

Figure 6.9 (a), (b), (c), (d), and (e) Cross-sectional SEM of as-grown osmium silicide film grown by the template method showing clear hillock-like structure with no interaction between the film and the Si substrate below. Thicknesses of various parts of the film are around 8.5, 10, 17, 13, 41, 55 nm. 102

Figure 6.10 (a), (b), and (c) Cross-sectional SEM of as-grown osmium silicide film grown by the regular method showing no interaction of the film with the Si substrate below. Thicknesses of various parts of the film are around 13, 16, 21, 37, 47, and 67 nm. 103

Figure 6.11 (a), (b), and (c) Cross-sectional SEM of annealed osmium silicide film grown by the template method, showing a less hillock height in comparison with the as-grown by the same method. Also, a clear interaction between the film and the Si substrate below is shown. Thicknesses of various parts of the films are around 39, 47, and 58 nm. 104

Figure 6.12 (a), (b), and (c) Cross-sectional SEM of annealed osmium silicide film grown by the regular method shows comparatively smoother (lesser thickness) than annealed films grown by the template method. Also, a clear interaction between the film and the Si substrate is evident in annealed films of grown by the template and the regular methods.. 105

Figure 6.13 AFM of as-grown osmium silicide film grown by the template method. RMS surface roughness = 11.8 nm. 107

Figure 6.14 AFM of annealed osmium silicide film grown by the template method. RMS surface roughness = 11.4 nm. 107

Figure 6.15 AFM of as-grown osmium silicide film grown by the regular method. RMS surface roughness = 10.5 nm... 108

Figure 6.16 AFM of annealed osmium silicide film grown by the regular method. RMS surface roughness = 4.6 nm.. 108

Figure 6.17 (a) and (b) Pre-sputtering stoichiometric ratios and binding energies of as-grown osmium silicide films by the template method showing the oxidation of the surface of the films as confirmed by the SiO_2 binding energy peak. The Os:Si

cannot be confirmed here unless the oxygen is removed from the elemental percentages, as it is shown in Figure 6.19 and Figure 6.21. 111

Figure 6.18 (a) and (b) Post sputtering stoichiometric ratios and binding energies of as-grown osmium silicide films by the template method showing no oxygen peak confirming that the surface oxidation in the pre-sputtered films was due to exposure to air. Ar sputtering is only around 30 A^0 deep into the film. Also, the Os:Si ratios are close to 4, as desired and maintained during growth by the Os and Si flux controls. This Si rich ratio results in the growth of single phase Os_2Si_3[90]. 112

Figure 6.19 (a) and (b) Pre-sputtering stoichiometric ratios and binding energies of annealed osmium silicide films by the template method showing surface oxidation as well as an off Os:Si ratio, with a very much Si rich film, this may be attributed to the interaction of the annealed film with the Si substrate below as evident from the cross-sectional SEM images in section 6.4 of this chapter. 113

Figure 6.20 (a) and (b) Post sputtering stoichiometric ratios and binding energies of annealed osmium silicide films by the template method showing an off Os:Si ratio that is very much Si rich. This is consistent with the pre-sputtered annealed films grown by the same method shown in Figure 6.19. 114

Figure 6.21 (a) and (b) Pre-sputtering stoichiometric ratios and binding energies of as-grown osmium silicide films by the regular method showing oxidation of the surface of the film. However, excluding oxygen, yields the desired Si rich Os:Si ratio of 4 in order to obtain single phase Os_2Si_3[90].. 115

Figure 6.22 (a) and (b) Post sputtering stoichiometric ratios and binding energies of as-grown osmium silicide films by the regular method showing no surface oxidation as well as comparatively close agreement with the desired Si rich Os:Si ratio. This is consistent with the pre-sputtered as-grown films shown in Figure 6.21 if oxygen is removed from the elemental percentage. 116

Figure 6.23 Pre-sputtering stoichiometric ratios and binding energies of annealed osmium silicide films by the regular method. Again, pre-sputtered films show surface oxidation, once again, annealed films by both growth methods show a clear off Os:Si ratio which is very Si rich due to the film-substrate interaction during annealing. 116

Figure 6.24 Post puttering stoichiometric ratios and binding energies of annealed osmium silicide films by the regular method showing no surface oxidation, yet reveals a consistent off Os:Si ratio of annealed films, which is greatly attributed to the film interaction with the Si substrate during the annealing process........................ 117

Figure 6.25 Micro Raman Spectroscopy of as-grown and annealed osmium silicide films MBE grown by the template method showing signature peaks in the region less than 500 cm^{-1} that are distinct from pure Si. 119

Figure 6.26 Micro Raman Spectroscopy of as-grown and annealed osmium silicide films MBE grown by the regular method showing active Raman shifts less than 500 cm^{-1} which are clearly different from those of pure Si. 119

Figure 6.27 A clearer view of the Raman spectra at shifts less than 500 cm^{-1} of the as-grown and annealed osmium silicide films grown by the MBE template method;

Annealing the sample results in several sharp peaks at 126, 140, 162, 184 and 196 cm^{-1}. The peaks are significantly sharper –better film quality- in the annealed films grown by the template method in comparison with annealed ones grown by the regular method. 120

Figure 6.28 A clearer view of the Raman spectra at shifts less than 500 cm^{-1} of the as-grown and annealed osmium silicide films grown by the regular MBE method; The peaks of the annealed template-grown films appear in the regular-grown films in both the as-grown and the annealed. The sharp peaks are at 126, 140, 162, 184 and 196 cm^{-1}. The peaks of the as-grown films by the regular method are certainly sharper -better film quality- than the as-grown ones by the template method. 120

CHAPTER 1

PHYSICS OF SEMI-CONDUCTOR SILICIDES

In this chapter, we discuss the physics of what, why, and how of the semi-conductor material systems of choice in this work. Just like every piece of art has a story, every state-of-the-art research and study has its story. The physical background and the motivation behind this work are in section 1.1. In section 1.2, the general material aspects of the silicides of choice are presented, in terms of crystal structure, lattice parameters, space groups, inter-atomic distances, density … etc. Section 1.3 focuses on the thermodynamics of silicidation of these silicides, their phase diagrams, and how the different stable and meta-stable phases transform, transition, and exist. Kinetics of silicidation is in section 1.4. Most interestingly, the basic physical quantities and relationships of the quantum mechanics of an electron, electronic band structure, and the theoretical and experimental reports of band-gap natures and the band-gap energy values of the silicides of choice is spread out in chapter 2.

1.1 Physical Background, Story, and Motivation

The semi-conductor industry heavily relies on silicon for most of its applications due to the low cost of the material and the advanced manufacturing technology and processes that are readily available for silicon. However, life is not perfect and so is silicon. As shown in Figure 1.1, silicon has an indirect band-gap. Consequently, Si as a material doesn't possess great versatility for multifunctional applications in comparison with the direct band-gap III-V semi-conductors such as GaAs. Considering momentum, the photon emission/absorption requires conservation of energy and momentum (wave number). Chapter 2 has further explanation

about the origin and the physics of the electronic band structure of semi-conductors and the differences between direct and indirect bandgaps from a physical perspective.

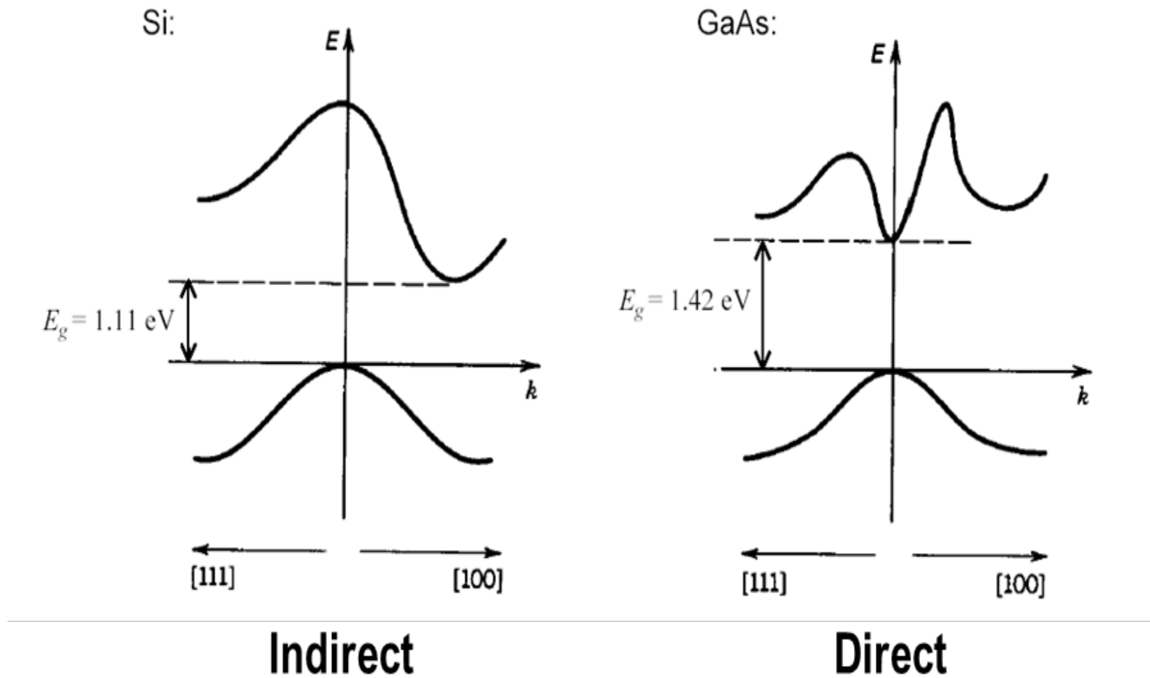

Figure 1.1 Energy vs. momentum (wave number) showing the indirect band-gap of Si vs. the direct band-gap of GaAs

At this point, one can articulate the statement of the problem and the motivation. In essence, what is ideally required is a Si based semi-conductor material system that possesses a direct-band gap and therefore has significantly greater versatility. This would certainly be instrumental to certain important semi-conductor industry applications such as optical contacts for silicon-based integrated circuits, fiber optics, and thermal sensing in the near infrared region, etc. A lot of research has been employed to bridge this gap using various approaches. However, one approach that has not been extensively studied is the semi-conducting silicides material systems.[1]

Semi-conducting silicides and their associated germanides offer significant potential to realize these goals. Silicides are not all semi-conducting. To the contrary, there are more than one hundred and eighty (180) silicides which are chemical compounds of silicon with different metals. Generally, most silicides are metallic with high thermal stability, resistance to oxidation, and low resistivity. These properties result in the extensive use of silicides for interconnections and contacts – Ohmic contacts and Schottky barriers – in silicon-based integrated circuits. However, only a few are semi-conducting. There are around a dozen semi-conducting silicides with band-gaps ranging from 0.07 to 2.3 eV with the possibility of ternary silicides. Some of the semi-conducting silicides are direct/quasi-direct band-gap semi-conductors. These semi-conductor silicides include: (i) β-$FeSi_2$ which has a direct (quasi-direct) band-gap of around 0.8 eV;[2] (ii) Ru_2Si_3 which has a band-gap ranging from 0.44 to 1.1 eV according to experimental results, and a direct band-gap at 0.4 eV according to theoretical predictions; (iii) Os_2Si_3 which has an experimentally reported band-gap of 0.95 and 2.3 eV depending on the source; and (iv) $OsSi_2$ which has a direct band-gap of 1.8 eV according to experimental data.[3] It is worth mentioning that most of the semi-conducting silicides have been sparsely studied except for β-$FeSi_2$ due to reports of light emission, as it has been used to produce light emitting diodes.[4] Semi-conducting silicides may provide additional choices to III–V and II–VI material systems for optoelectronic and multi-functional applications. However, the ultimate usefulness of these materials will depend on the ability to control the phase and alloy content of the metal silicide. For instance, there are three stoichiometries for iron silicide: Fe_2Si, FeSi, and $FeSi_2$ where $FeSi_2$ also has three known phases. Therefore, the growth of crystalline materials under ultra-high vacuum (UHV) conditions, which is known as molecular beam epitaxy (MBE), generally gives the

greatest control of the crystalline phase of that material. Since there are multiple stable crystal structures for most of the metal silicides, growth of heterostructures and super-lattices by MBE shows the greatest promise. This technique also can be used to perform band-gap engineering (tuning of the band-gap of a semiconductor by substitutionally alloying one of the constituent elements with a different element). More in depth information about MBE, its growth methods, and equipment used is in the subsequent chapters of this study. Table 1.1 shows condensed basic information about the various semi-conducting silicides and their band-gaps while grouping them into different groups based on their structure and space group. Table 1.2 shows the semi-conducting silicides and their germanide counter parts. In Table 1.1, Group A and group C, namely, Fe-Si (β-$FeSi_2$), Ru-Si (Ru_2Si_3), and Os-Si ($OsSi_2$ and Os_2Si_3) semi-conductor systems will be further presented and discussed in terms of general material aspects, thermodynamics and kinetics of silicidation, electronic band structure, and molecular beam epitaxial growth and structural characterization.

Group	Phase	Structure	Space Group	Lattice	Lattice Parameters			Experimental Bandgap	Type of Bandgap (Experimental)	Theoretical Bandgap	Type of Bandgap (Theoretical)
					a	b	c				
A	β-$FeSi_2$	β-$FeSi_2$	Cmca	Orthorhombic	0.98792	0.77991	0.78388	0.87	Direct	0.78	Quasi-direct
	$OsSi_2$	β-$FeSi_2$	Cmca	Orthorhombic	1.0150	0.8117	0.8223	1.4		0.95	Indirect
								1.8		1.14	Direct
B	$CrSi_2$	$CrSi_2$	$P6_222$	Hexagonal	0.4431		0.6364	0.35	Indirect	0.21-0.38	Indirect
								0.5	Direct	0.37-0.47	Indirect
								0.67	Indirect		
								0.98	Direct		
	$MoSi_2$	$CrSi_2$	$P6_222$	Hexagonal	0.4642		0.6529	0.07	Indirect		
	WSi_2	$CrSi_2$	$P6_222$	Hexagonal	0.4614		0.6414	0.07	Indirect		
C	Ru_2Si_3	Ru_2Si_3	Pbcn	Orthorhombic	1.1057	0.8934	0.5533	0.44		0.40	Direct
								0.7			
								1.09			
	Os_2Si_3	Ru_2Si_3	Pbcn	Orthorhombic	1.1124	0.8932	0.5570	2.3			
								0.95	Direct		
D	OsSi	FeSi	$P2_13$	Cubic	0.4729			0.34			
	Os_2Si_3	Ru_2Si_3	Pbcn	Orthorhombic	1.1124	0.8932	0.5570	2.3			
								0.95	Direct		
	$OsSi_2$	β-$FeSi_2$	Cmca	Orthorhombic	1.0150	0.8117	0.8223	1.4		0.95	Indirect
								1.8		1.14	Direct
E	Ir_3Si_5		$P2_1/C$	Monoclinic	0.6406	1.4162	1.1553	1.2	Direct		
	Mg_2Si	CaF_2	Fm3m	Cubic	0.63512			0.78	Indirect		
	$BaSi_2$	$BaSi_2$	Pnma	Orthorhombic	0.892	0.680	1.158	0.48			
								1.3			

Table 1.1 Condensed basic information of the semi-conducting silicides[5], adapted from Borisenko[2] showing the silicides of choice in this work.

Phase	Structure	Space Group	Lattice
β-$FeSi_2$	β-$FeSi_2$	Cmca	Orthorhombic
β-$FeGe_2$	β-$FeSi_2$	Cmca	Orthorhombic
$BaSi_2$	$BaSi_2$	Pnma	Orthorhombic
$BaGe_2$	$BaSi_2$	Pnma	Orthorhombic
Ru_2Si_3	Ru_2Si_3	Pcbn	Orthorhombic
Ru_2Ge_3		Pcbn	Orthorhombic
Os_2Si_3	Ru_2Si_3	Pbcn	Orthorhombic
Os_2Ge_3	Ru_2Si_3	Pbcn	Orthorhombic
$OsSi_2$	β-$FeSi_2$	Cmca	Orthorhombic
$OsGe_2$	$OsGe_2$	C2/m	Monoclinic (β=119^{0}10')

Table 1.2 Semi-conducting silicides and their germanide counter parts.[2] Many of the silicides are of similar structure and space group as their germanides.

1.2 General Material Aspects

1.2.1 Fe-Si (β-$FeSi_2$) Semi-conductor Material System

This semi-conductor silicide belongs to the *Cmca* space group. It has an orthorhombic crystal structure.[6] It remains stable up to around 960 ^{0}C. The primitive cell of the crystalline structure of β-$FeSi_2$ contains 24 atoms. It is a base-centered orthorhombic structure. Its density is 4.93 g/cm^3.[7] There are two sets of 8 iron and 16 silicon atoms grouped together, namely Fe-1, Fe-2, Si-1, and Si-2. These two sets have slightly different distances. The range of distances between the Fe-1 and Si atoms is between 0.234 and 0.239 nm, and the distances between the Fe-2 and Si atoms are between 0.234 and 0.244 nm. The angles of the Si--Fe-1--Si range from 62.5^0 to 99.5^0 while the angles of the Si--Fe-2--Si range from 61.8^0 to 99.5^0. Table 1.3 shows the atomic positions in the β-$FeSi_2$ primitive cell, and Table 1.4 shows the nearest-neighbor interatomic distances.

Atom	Inequivalent Site	*x-value*	*y-value*	*z-value*
Fe-1	8d	0.21465	0.0	0.0
Fe-2	8f	0.0	0.19139	0.81504
Si-1	16g	0.37177	0.27465	0.44880
Si-2	16g	0.12729	0.04499	0.27392

Table 1.3 Atomic positions in orthorhombic $FeSi_2$,[6] primitive translation vectors are used.

Atom	Fe-1	Fe-2	Si-1	Si-2
Fe-1	0.3957	0.2967	0.2338	0.2339
Fe-2		0.4022	0.2333	0.2335
Si-1			0.2529	0.2499
Si-2				0.2449

Table 1.4 Nearest-neighbor interatomic distances in units of nm in the orthorhombic β-$FeSi_2$ for *a=0.9863, b=0.7791, c=0.7833 nm*.[2]

1.2.2 Ru-Si (Ru_2Si_3) Semi-conductor Material System

Ru_2Si_3 is of the orthorhombic structure and the *Pbcn* space group below the temperature of 1000^0C. Around 1000^0C it undergoes a phase transition to a tetragonal structure of the $P\bar{4}c2$ space group after the Si atoms displace from their positions corresponding to the *Pbcn* symmetry and pass through an intermediate orthorhombic *Pb2n* configuration. This transition is reversible. We are concerned with the orthorhombic Ru_2Si_3 of the *Pbcn* space group in the scope of this study. Its density is 6.96 g/cm^3.[8] It is worth mentioning that orthorhombic Ru_2Si_3 belongs to the chimney-ladder compounds,[8] with a large and complex unit cell composed of 16 Ru atoms and 24 Si atoms – a total of 40 atoms. There are three sets of ruthenium and silicon atoms (Ru-1, Ru-2, Ru-3, Si-1, Si-2, Si-3). Figure 1.2 shows the plane projections of atoms in the unit cell (The numbers inside the circles indicates the atomic site distance from the plane in the perpendicular direction).

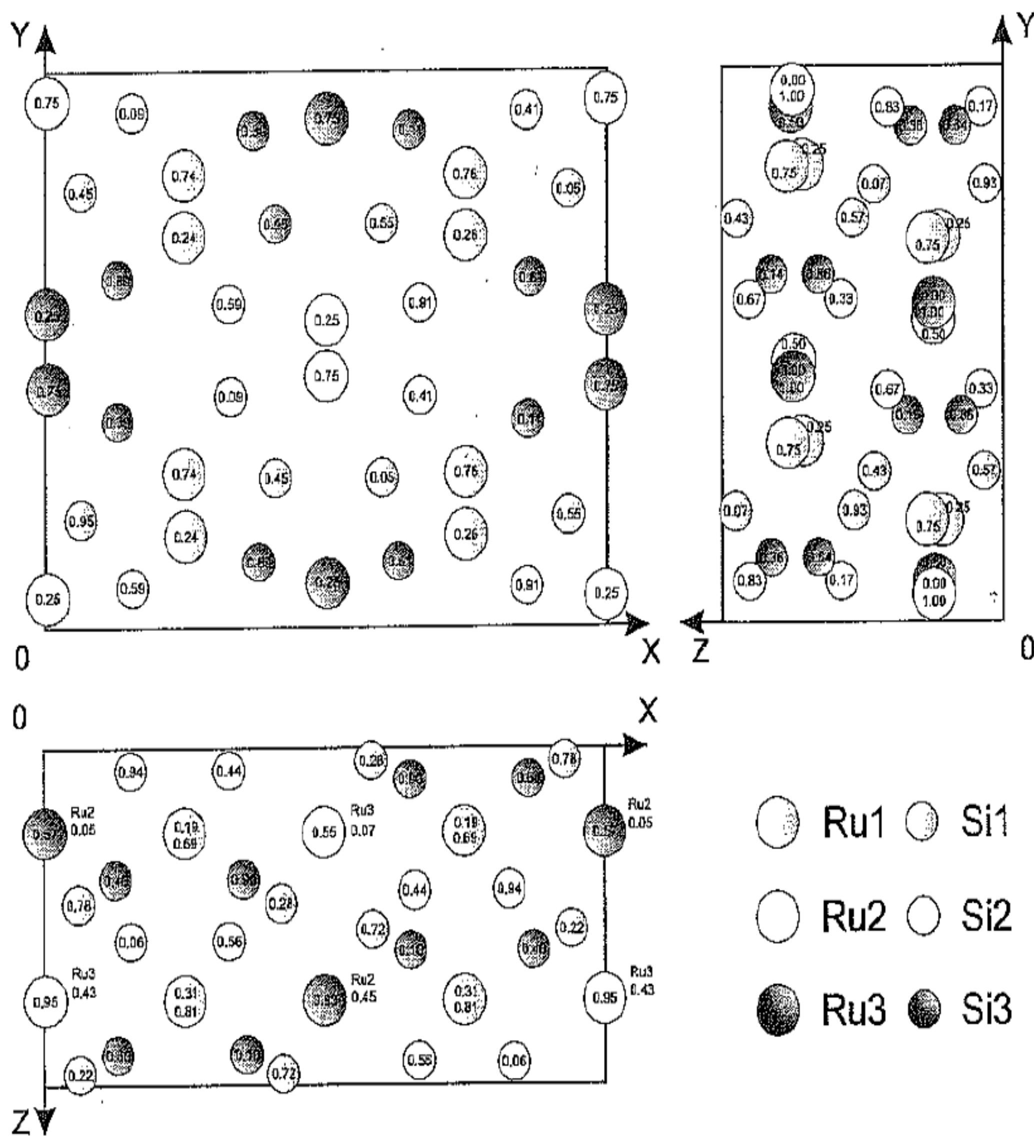

Figure 1.2 Projections of orthorhombic Ru_2Si_3 unit cell on the *xy, xz,* and *yz* planes.[8] The numbers inside the circles indicates the atomic site distance from the plane in the perpendicular direction.

Every ruthenium and silicon atom has four ruthenium atoms as its neighbor. The average distance between the ruthenium and the silicon neighbors with respect to the three silicon sites (Si-1, Si-2, and Si-3) is 0.242, 0.245, and 0.242 nm respectively. It appears that the nearest neighbor distances between ruthenium and silicon and between silicon and silicon are

of the same order in the orthorhombic Ru_2Si_3. However, there is no fixed bond length between the ruthenium atoms. Table 1.5 shows the atomic positions in the primitive cell, and Table 1.6 shows the nearest neighbor interatomic distances.

Atom	Inequivalent Site	*X-value*	*Y-value*	*Z-value*
Ru-1	8d	0.2472	0.1864	0.2401
Ru-2	4c	0.0	0.0451	0.25
Ru-3	4c	0.0	0.5748	0.25
Si-1	8d	0.4275	0.2841	0.4537
Si-2	8d	0.3253	0.4350	0.0934
Si-3	8d	0.1366	0.3994	0.3946

Table 1.5 Atomic positions in orthorhombic Ru_2Si_3 (in units of the primitive translational vectors).[8]

Atom	Ru-1	Ru-2	Ru-3	Si-1	Si-2	Si-3
Ru-1	0.2991	0.3011	0.2968	0.2476	0.2375	0.2418
Ru-2		0.2881	0.4202	0.2379	0.2334	0.3597
Ru-3			0.3072	0.2326	0.3852	0.2319
Si-1				0.2766	0.2659	0.2956
Si-2					0.3000	0.2689
Si-3						0.3299

Table 1.6 Nearest neighbor interatomic distances in orthorhombic Ru_2Si_3, in units of nm, for *a=1.1436 nm, b=0.9238 nm, and c=0.5716 nm.*

1.2.3 Os-Si (Os_2Si_3 and $OsSi_2$) Semi-conductor Material System

Os_2Si_3: The structure of this semi-conducting silicide is orthorhombic and its space group is the *Pbcn*. It is iso-structural to the Ru_2Si_3.[8] However, there are no accurate data on its atomic positions. It has eight formula units in its unit cell. Its lattice parameters are *a=1.1124 nm, b=0.8932 nm,* and *c=0.5570 nm* [Ref B1.13]. Its density is 11.15 g/cm^3.[9]

$OsSi_2$: The structure of this semi-conducting silicide is also orthorhombic and its space group is the *Cmca*. It is iso-structural to the β-$FeSi_2$ [Ref B1.40]. Its density is 9.66 g/cm^3.[9] Table 1.7 shows the atomic positions in its primitive cell and Table 1.8 shows the nearest neighbor interatomic distances.

Atom	Inequivalent Site	*X-value*	*Y-value*	*z-value*
Os-1	8d	0.2142	0.0	0.0
Os-2	8f	0.0	0.1881	0.1812
Si-1	16g	0.3699	0.2208	0.0597
Si-2	16g	0.1280	0.0534	0.7252

Table 1.7 Atomic positions in the orthorhombic $OsSi_2$ in units of the primitive translational vectors.[10]

Atom	Os-1	Os-2	Si-1	Si-2
Os-1	0.4175	0.3046	0.2439	0.2462
Os-2		0.2442	0.2493	0.2474
Si-1			0.2641	0.2547
Si-2				0.2510

Table 1.8 Nearest neighbor interatomic distances in units of nm in orthorhombic $OsSi_2$, for *a=1.014 nm, b=0.811 nm, c=0.822 nm*.

1.3 Thermodynamics of Silicidation

Before dwelling into the phase diagrams of the silicides of choice and the existence of the various phases of these silicides at different temperatures and their level of stability, it is essential to stress the fact that the silicide formation in general can be described by a chemical reaction between silicon (Si) and metal (M). This chemical reaction can be shown using the following chemical notation and scheme:[2]

The reaction above is also termed a direct reaction. Other than direct reactions, silicides can also form due to chemical reactions between either the metal or silicon with an existing silicide phase. Consequently, the chemical reaction can be shown using the following extended chemical notations and schema:[2]

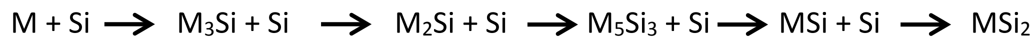

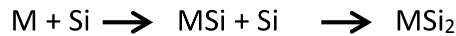

1.3.1 Fe-Si (β-$FeSi_2$) Semi-conductor Material System

The Fe-Si material system phase diagram is quite a complex one due to the presence of various phases within the metal-rich and silicon-rich regions. There are four main phases that are present in this system, namely Fe_3Si, Fe_5Si_3, FeSi, and $FeSi_2$. The Fe_3Si is a metal-rich phase. The Fe_5Si_3 is an intermediate phase. The FeSi is a monosilicide. The $FeSi_2$ is a disilicide. The disilicide $FeSi_2$ has three known phases,[7,11] namely the tetragonal α-$FeSi_2$, the orthorhombic β-$FeSi_2$, and the cubic γ-$FeSi_2$. Both the α-$FeSi_2$, and the γ-$FeSi_2$ are metallic leaving the orthorhombic β-$FeSi_2$ to be the only semi-conductor phase of the Fe-Si system. It is worth mentioning that the metallic α-$FeSi_2$ phase is only stable at higher temperatures of around 950 ^{0}C till the melting point. The semi-conducting β-$FeSi_2$ phase can be formed from the high-

temperature metallic phase below 950 ^{0}C following this scheme:[7]

$$\alpha\text{-}FeSi_2 \longrightarrow \beta\text{-}FeSi_2 + Si$$

Also, the β-$FeSi_2$ phase can transition into the α-$FeSi_2$ above 970 ^{0}C following this scheme:[6]

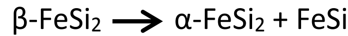

$$\beta\text{-}FeSi_2 \longrightarrow \alpha\text{-}FeSi_2 + FeSi$$

It is of interest to know that the semi-conducting β-$FeSi_2$ phase is stoichiometric and stable at temperatures below 950 ^{0}C while the metallic cubic γ-$FeSi_2$ is meta-stable appearing only at low temperatures.[7] Table 1.9 shows the parameters of thermodynamics of silicidation in the Fe-Si system, and Figure 1.3 shows the phase diagram of the Fe-Si system.[12]

Thermodynamic Parameter	**Fe**	**Fe_3Si**	**Fe_5Si_3**	**FeSi**	**$FeSi_2$**
Melting point T_m(^{0}C) [a]	1538	1240	1203	1410	1212
Enthalpy of melting (kJ/mole)[b]		57.01		70.41	88.70
Enthalpy of formation (kJ/mole of atoms)[c]		25.8	30.6[d]	39.3	30.6

Table 1.9 Parameters of thermodynamics of silicidation in the Fe-Si material system. [a]Reference [12]. [b]Reference [7]. [c]Reference [13]. [d]Reference [14]

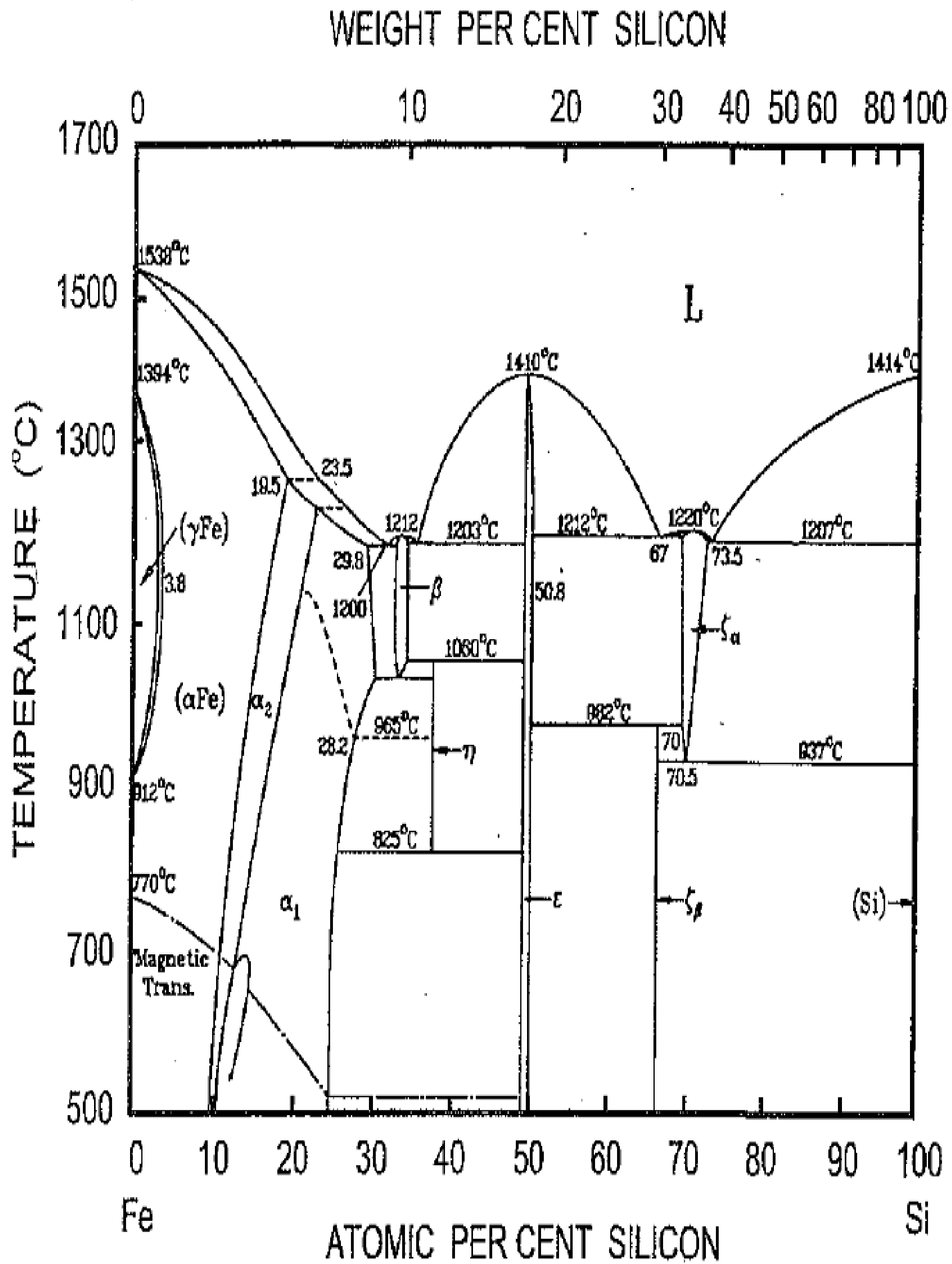

Figure 1.3 The phase diagram of the Fe-Si material system.[12] Temperature (^{0}C) vs. Atomic per cent silicon. It shows the complexity and the various phases of the Fe-Si system.

1.3.2 Ru-Si (Ru_2Si_3) Semi-conductor Material System

The phase diagram of this material system is shown in Figure 1.4. The phase diagram[12] together with earlier studies[7] shows the formation of the metal-rich and intermediate phases such as Ru_2Si, Ru_5Si_3, Ru_4Si_3, the monosilicide RuSi, as well as the most stable silicon-rich phase Ru_2Si_3. The Ru_2Si_3 phase crystallizes below 1000 ^{0}C. It has an orthorhombic lattice with a *Pbcn* space group.[15] This Ru_2Si_3 phase is a semi-conducting phase that can transform into a tetragonal structure of the same stoichiometry at higher temperatures.

1.3.3 Os-Si (Os_2Si_3 and $OsSi_2$) Semi-conductor Material System

This material system has three stable phases, namely the disilicide $OsSi_2$, the monosilicide OsSi, and the Silicon-rich Os_2Si_3 phase. It is worth mentioning that the disilicide $OsSi_2$ phase has an orthorhombic structure. There is also a metastable $OsSi_2$ phase that has a monoclinic structure as shown in the phase diagram in Figure 1.5.

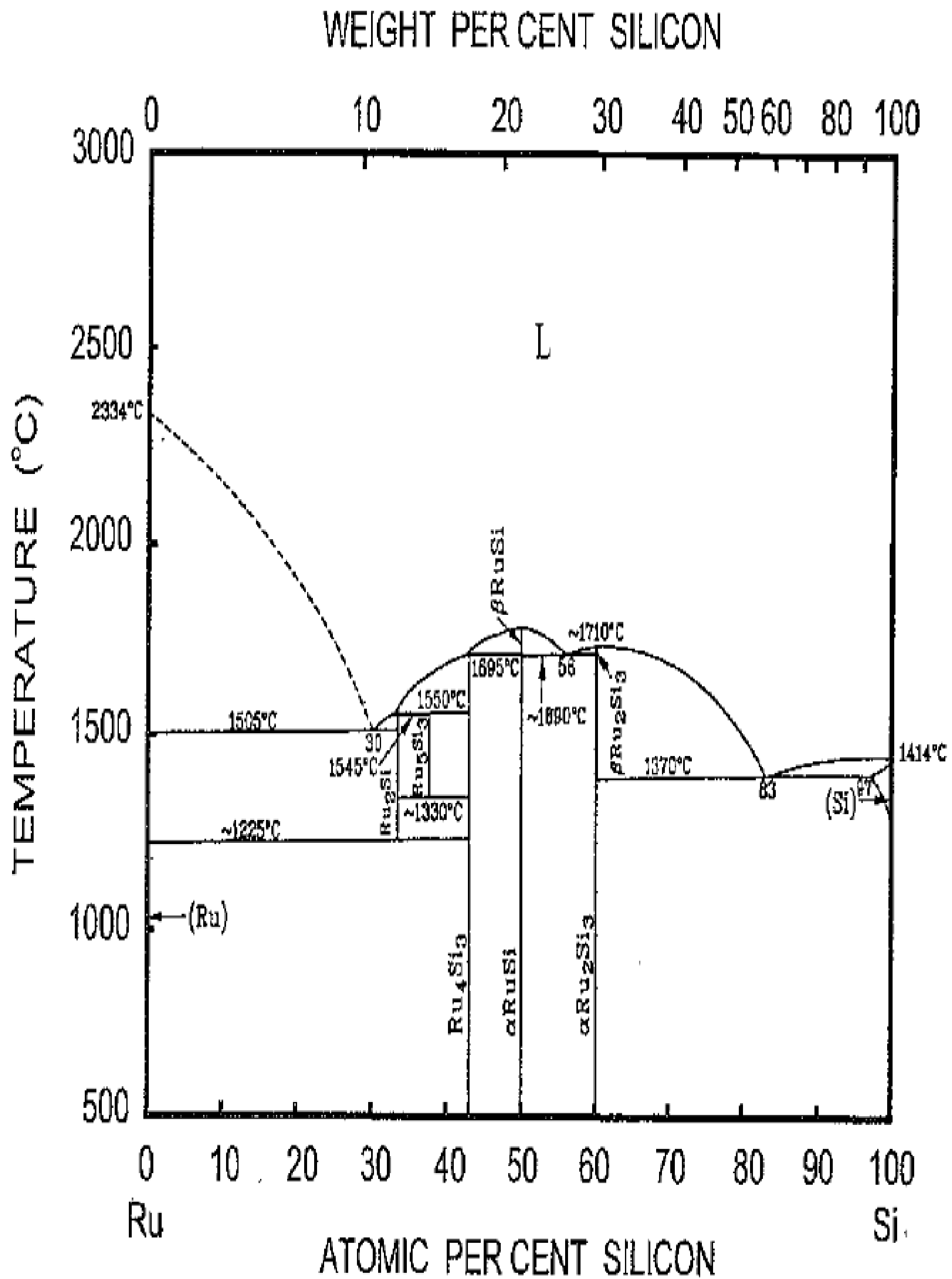

Figure 1.4 The phase diagram of the Ru-Si material system.[12] It shows its most stable silicon-rich phase Ru_2Si_3 which crystallizes below 1000 ^{0}C.

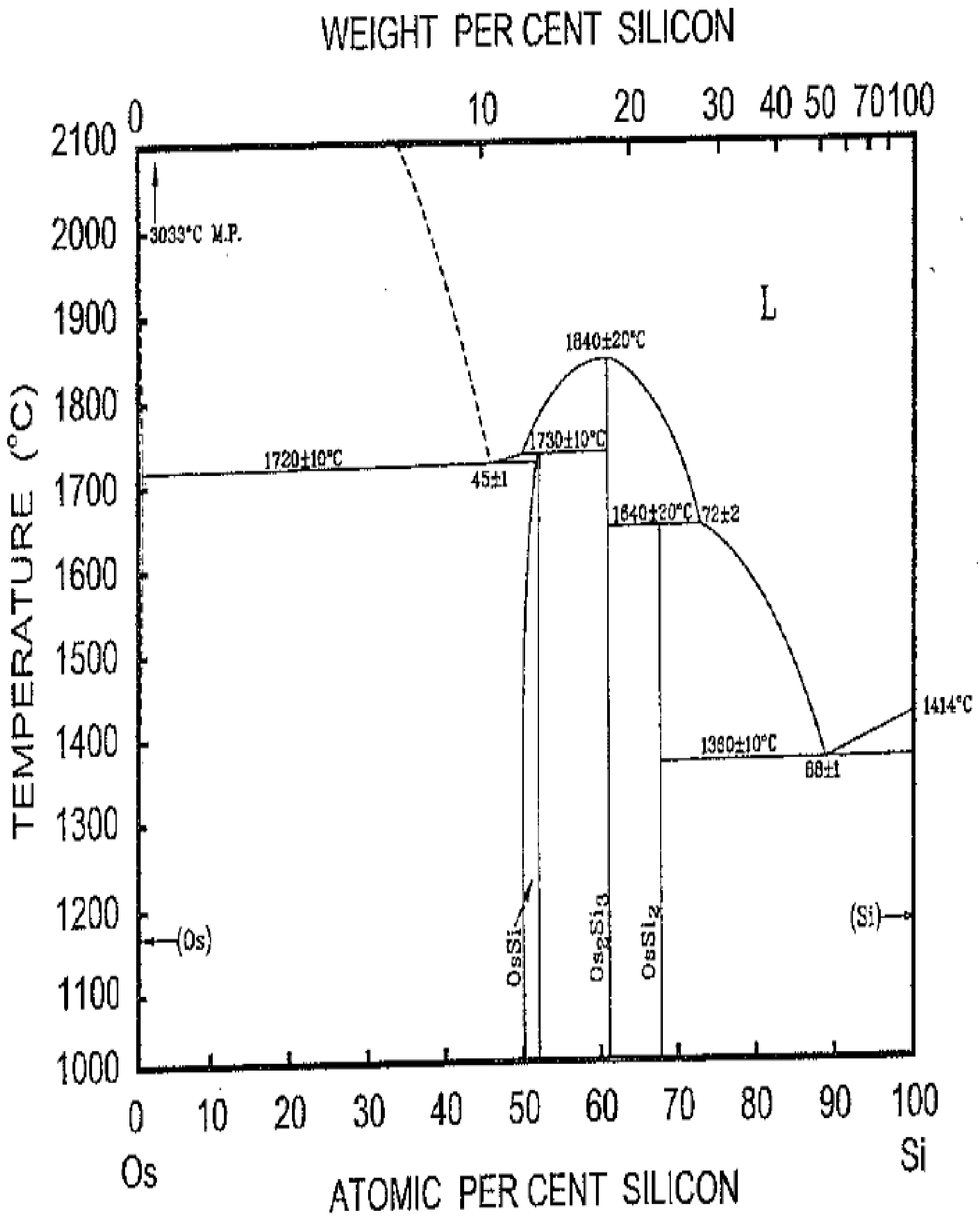

Figure 1.5 The phase diagram of the Os-Si material system.[12] It shows its three stable phases, namely the disilicide $OsSi_2$, the monosilicide OsSi, and the Silicon-rich Os_2Si_3 phase.

1.4 Kinetics of Silicidation

Needless to mention, that lowering the free energy of any system is the way for such a system to reach a state of equilibrium. In the world of thin films, heating of such system makes its atoms move, diffuse, and react with one another to form chemical compounds; especially if these thin film were originally formed at low temperatures (room temperature or below). Consequently, certain phases of a particular system can nucleate first before others. Silicides are no different in this regard. Thin silicide films can form by the simultaneous co-deposition of the metal and silicon atoms, such simultaneous co-deposition result in the existence interfaces between the virgin agglomerated grains inside the film. Certainly, raising the temperature of this system would allow solid state reactions to happen at these interfaces resulting in the production of such silicide. Also, thin silicide films can form through layer-by-layer deposition of the metal and the silicon resulting in the existence of interfaces between the pure metal layer and the silicon film and between the metal film and the silicon substrate.

As illustrated in section 1.3, the phase diagram of a metal-silicon system has many stable phases. Therefore, to predict (theoretically) or to find out (experimentally) which of these phases nucleates first, and which ones form later, is definitely an interesting matter. In the next few sections, the silicides of choice in this study will be discussed.

1.4.1 Fe-Si (β-$FeSi_2$) Semi-conductor Material System

According to the most reliable published data about thin film structures in this metal-silicon material system, for example,[16] the monosilicide FeSi is the phase that nucleates and grows at first. The disilicide β-$FeSi_2$ phase grows from the monosilicide FeSi in the temperature

range[17] of 450-530 ^{0}C through a process that is nucleation-controlled.[18,19] Then, the disilicide β-$FeSi_2$ further grows via a process that is primarily diffusion-controlled. Heating up the iron silicide thin film structure to above 900 ^{0}C initiates the transformation of the semi-conducting disilicide β-$FeSi_2$ into its disilicide metallic phase α- $FeSi_2$.[20-23] Also in cases of rapid thermal processing the same general sequence of phase changes and transformation is conserved, [19,23,24] as shown in the following example of chemical notation and scheme:

Table 1.10 shows the growth parameters of the iron silicide phases on different silicon substrates, the temperature range of their formation, and their respective activation energies from the mentioned and tabulated references.

Phase	Substrate	Temperature range (^{0}C)	Activation energy E_a (eV)	References
FeSi	Si(100)	450-525	1.67	25
	Si(111)	290-410	1.5	16
	Si(111)	500-625**	1.36	24
β-$FeSi_2$	Si(111)	450-530	1.8	16
	Si-amorphous	525-625	1.5	26
	Si(111)	675-750**	2.3*	24

Table 1.10 The growth parameters of Fe-Si material system. * Shows the value from the experimental data in the reference. ** Shows the value by rapid thermal processing

1.4.2 Ru-Si (Ru_2Si_3) Semi-conductor Material System

Starting out with a pure ruthenium film and a silicon substrate, the pure metal film gets converted into the silicide when processed at 485-500 ^{0}C. Diffusion is the mechanism controlling the growth of this silicide layer. The mobile species during the thin silicide film

formation are mostly silicon atoms.[27] This silicide phase is the semi-conducting Ru_2Si_3. It is also worth mentioning that this is the only silicide phase produced when annealing a pure ruthenium metal film on a silicon substrate through the whole temperature range of 375-1000 ^{0}C.[28-30] According to Petersson et al., the activation energy is 1.8 eV, in the temperature range of 375-450 ^{0}C.[28]

1.4.3 Os-Si (Os_2Si_3 and $OsSi_2$) Semi-conductor Material System

Starting out with an osmium film and a silicon substrate, the silicon-rich di-osmium tri-silicide Os_2Si_3 phase is formed at first at a temperature of 600 ^{0}C where the growth process is limited to diffusion.[28,31] The activation energy is 1.8 eV in the temperature range of 450-525 ^{0}C. In the temperature range of 730-750 ^{0}C, Os_2Si_3 transforms into $OsSi_2$. However, interestingly enough, according to Chang et al. both silicide phases do exist in a multiphase silicide layer even after annealing at 1000 ^{0}C due to the pure osmium metal film being contaminated with oxygen.[31] It is worth mentioning that there is an osmium metal atom motion in temperature range of 750-1000 ^{0}C.[28] However, silicon atoms are mostly the mobile species in the formation of both of these silicide phases, namely Os_2Si_3 and $OsSi_2$. The problem with this metal-silicon material system is that the osmium films do not adhere well to the silicon and consequently peel off if the pure osmium film is thicker than 30 nm.

CHAPTER 2

ELECTRONIC BAND STRUCTURE OF SEMI-CONDUCTORS

2.1 Theoretical Considerations

Silicon is an indirect band-gap semi-conductor. However, some of the semi-conducting silicides are direct band-gap semi-conductors. While the previous statement seems very simple and straight forward, it is actually a striking fact, observation, and the main motivation behind the study of these silicides of choice. Before dwelling into the electronic band structure of the selected silicides in the following sub-sections, a brief mention of a few of the very basic physical quantities in the quantum mechanics of electrons, how a band structure appears from the periodic assembly of atoms in a solid, the differences between conductors, insulators, and semi-conductors, and the essential need for theoretical simulation methods are discussed. Standard textbooks have expanded details.[32-36]

The time-independent Schrodinger equation reads:

$$\mathbf{H}\Psi_n(\mathbf{r}) = E_n\Psi_n(\mathbf{r})$$

where **H** is the Hamiltonian operator of an electron, Ψ_n is the wave function of an electron in an eigen-state n, E_n is the eigen value of the energy of an electron. The Hamiltonian operator **H** has both the kinetic energy term and the potential energy term:

$$\mathbf{H} = \mathbf{P}^2/2m + \mathbf{V}(\mathbf{r})$$

where **P** is the momentum of an electron, and **V**(**r**) is the potential energy term.

According to Pauli's exclusion principle and the principles of quantum mechanics, a maximum of two electrons of opposite spin (spin up and spin down) can occupy an eigen-state. The eigen values of the energy as a function of the wave vector **k**, are the energy bands, and

the $E_n(\mathbf{k})$ function is called the electronic band structure of the crystal, where the wave vector $\mathbf{k} = \mathbf{P}/\hbar$.

In order to better illustrate this, the energy spectrum of the lithium (Li) atom, Li molecule, and Li solid are shown in Figure 2.1.

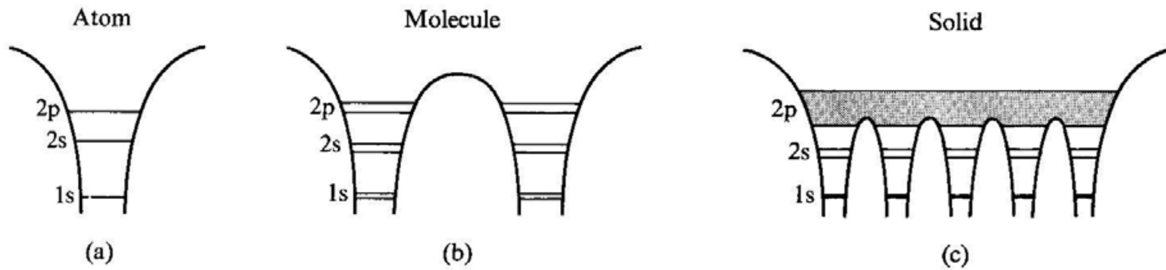

Figure 2.1 The energy spectrum of Li from an atom (a), to a molecule (b), to a solid (c)[37].

The Li atom has three electrons. At low temperatures these three electrons are distributed in the 1S and the 2S states in the following manner, as shown in Figure 2.1 (a)[37]:

2 electrons occupy the 1S state

The third electron occupies the 2S state

Figure 2.1 (b) shows the energy spectrum of the Li_2 molecule in which the energy states split into doublets of slightly different energies from each other, as a result of the interaction between the individual Li atoms. As more Li atoms come together and interact, further splitting of the energy states occurs. So, in a solid in which there are many atoms, of the order of 10^{23}, the quantum states split many times that the supposedly discrete quantized energy spectrum looks like a continuous energy spectrum due to the very small difference in energy between the split quantum states within that level[37]. At this point, one can start speaking about the origin of the band gap, since all of these energy states E_n mentioned earlier collectively make up a series

of energy bands, each of which are separated by a gap. Now, as far as the bulk material's energy band structure or the electronic band structure of the crystal $E_n(\mathbf{k})$, it is the energy, $E(\mathbf{k})$ of the electron states as a function of the wave vector, ($\mathbf{k}$).

It is worth mentioning that $E_n(\mathbf{k})$ normally does not have a simple analytical solution or form and thus the need for the use of quantum mechanical calculations and theoretical simulation methods such as the Linear Muffin-Tin Orbitals (LMTO) method and others in order to illustrate the band structure[2].

Based on the band structure, materials in general are divided, more or less, into three types in terms of their electrical behavior and nature. Materials can be conductors, insulators, or semi-conductors depending on the band structure and how full/empty particular bands are, since the very reason for electron flow is the existence and accessibility of an empty state to a previously bound electron. Fully conducting materials (metals) allow free electron flow (electric current) upon applying an electric field. On the contrary, insulators resist the flow of electrons. As a matter of fact, the difference in resistivities between a good conductor and a good insulator is rather striking. The electrical resistivity of a pure metal is around 10^{-10} ohm.cm at a temperature of 1 K, while that of a good insulator is around 10^{22} ohm.cm. Such a drastic difference of 10^{32} can be the widest among all common physical properties of solids[38].

Figure 2.2 shows the band structure and the differences in electrons distribution in the bands between fully conducting materials (metals or conductors), insulators, and semi-conductors. Metals, as shown in Figure 2.2 (a), have electrons that are partially occupying one of the bands which mean that one band is partially full. This is the key reason why the highly energetic electrons need only a small amount of energy to enter and occupy new energy states

and consequently move freely about the solid[37]. Whereas in insulators, as shown in Figure 2.2 (b), electrons fully occupy one band which is called the valence band leaving the band above it in energy which is called the conduction band completely empty. The fundamental energy gap, also called band gap, between the top of the valence band and the bottom of the conduction band is too wide for electrons to easily jump across which is the key reason why insulators resist the flow of electrons even upon applying an electric field.

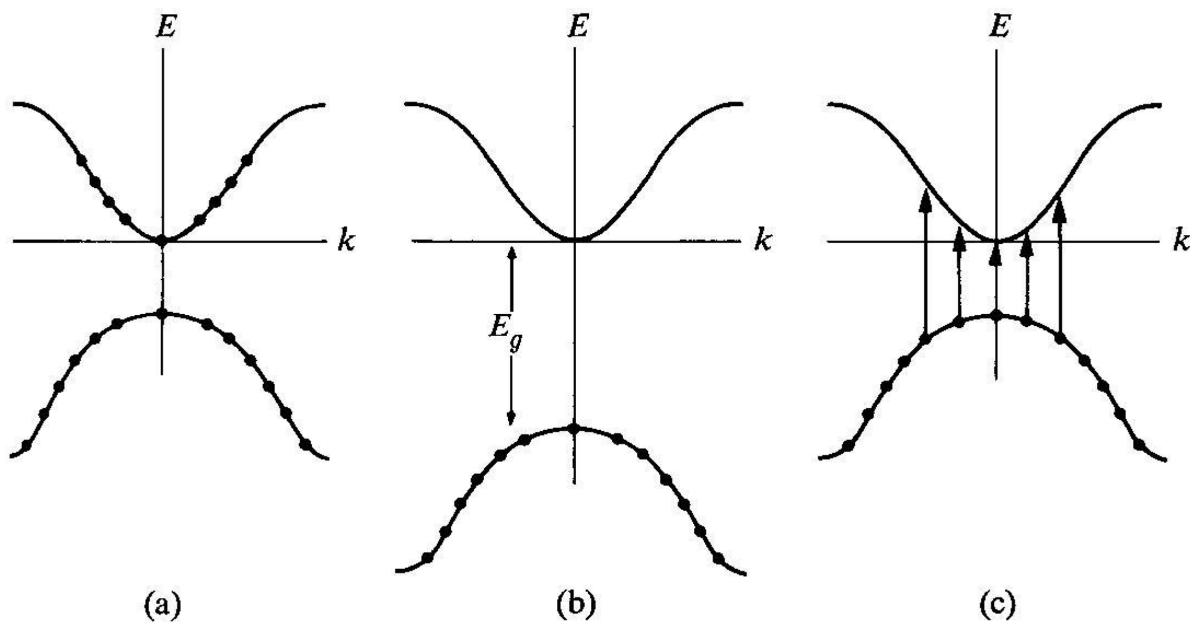

Figure 2.2 The distribution of electrons in the bands of (a) a metal, (b) an insulator, and (c) a semiconductor[37].

In semi-conductors however, it is interesting since semi-conductors are just like insulators[37] in the sense that the valence band is full of electrons while the conduction band is completely empty at absolute zero temperature[38], but the fundamental energy gap is not too wide to prevent electron from jumping across as shown in Figure 2.2 (c). Apart from narrow-band gap and wide-band gap semi-conductors, the band gap of a semi-conductor is normally

around 1 eV. Since the band gap of semi-conductors is small enough and as the temperature of the semi-conductor is raised, electrons become thermally excited and jump across from the valence band to the conduction band. When that happens, both the valence band (now with electrons and holes) and the conduction band (now with electrons) become partially full and hence the semi-conductor material now behaves as a conductor[38].

The band gap is the difference in energy between the lowest point in the conduction band, called the conduction band edge, and the highest point in the valence band, called the valence band edge[38]. If the valence band edge and the conduction band edge are at the same point in k-space, then the band gap is a direct band gap. On the contrary, an indirect band gap is when the valence band edge and the conduction band edge are not at the same point in k-space. Figure 2.3 (a) and (b) illustrate this difference respectively[39].

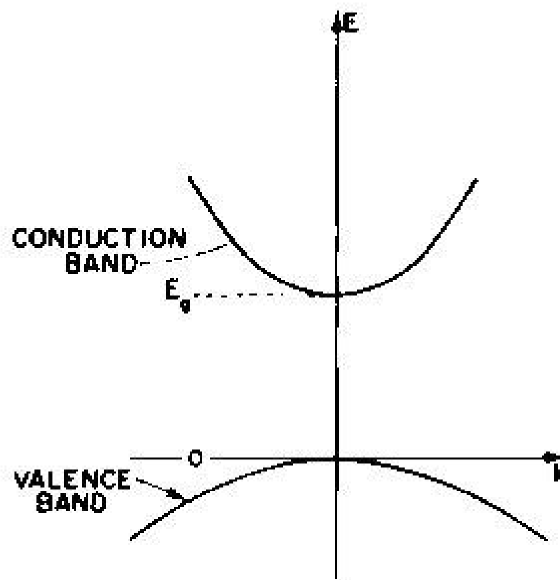

Figure 2.3 (a)

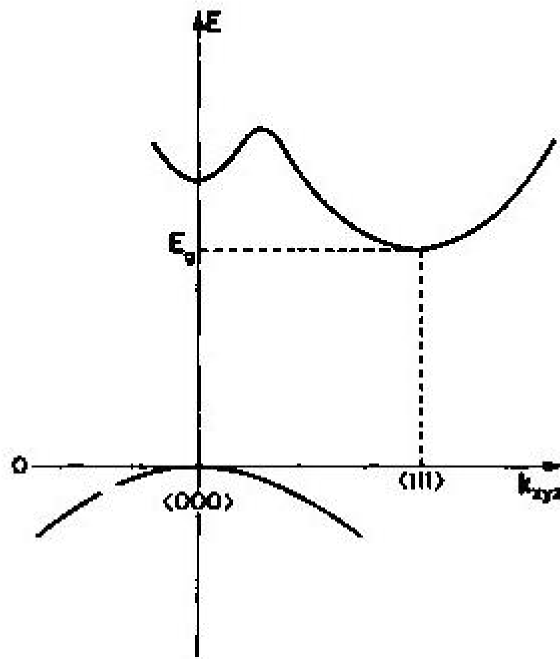

Figure 2.3 (b)

Figure 2.3 Energy vs. momentum in (a) a direct gap semiconductor and (b) an indirect gap semiconductor with a conduction band valley at k = <000>[39].

One of the best ways to measure the band gap is optical absorption[38]. In direct band gaps, there is a direct absorption process in which there are three types of matter are involved, a photon, an electron and a hole. A photon is absorbed by the crystal creating an electron in the conduction band and a hole in the valence band. In this case, the band gap:

$$E_g = \hbar\omega_g$$

Where E_g is the band gap measured and ω_g is the frequency of the threshold for continuous optical absorption. Figure 2.4 clearly shows that.

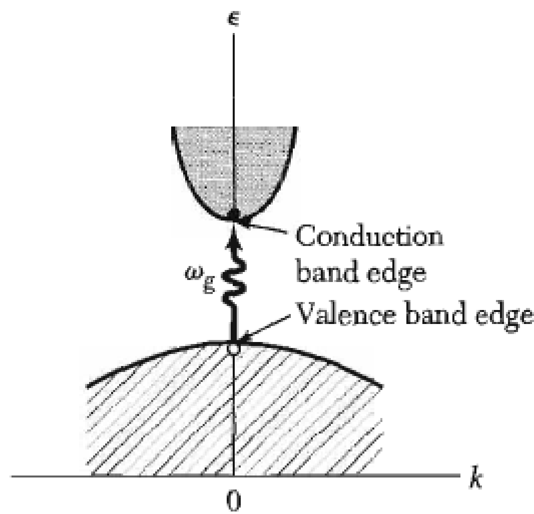

Figure 2.4 A direct band gap in which the lowest point in the conduction band is at the same **k**-value as the highest point in the valence band. A direct optical transition is vertically drawn without any significant change in **k**, since the photon has a very small wave vector. The threshold frequency ω_g for absorption by the direct transition determines the energy gap $E_g = \hbar\omega_g$. The figure and caption are adapted from Kittel[38].

However, in an indirect band gap, there is an indirect absorption process as shown in Figure 2.5. The lowest point in the conduction band and the highest point in the valence band are separated by a substantial wave vector $\mathbf{k}_c$[38]. Here, there are more than three types of matter are involved, a photon, an electron, a hole, and a phonon. Due to conservation laws, a direct photon transition at the energy of the minimum gap cannot satisfy the requirement to conserve the wave vector since the photon wave vectors are negligible[38]. So, a phonon of wave vector **K** and frequency Ω is created[38] satisfying the following:

$$\mathbf{K}(\text{photon}) = \mathbf{k}_c + \mathbf{K} \approx 0$$ [38]

$$\hbar\omega = E_g + \hbar\,\Omega$$ [38]

It is worth noting that the phonon energy $\hbar\,\Omega$ is much less than E_g[38] The phonon energy is generally around 0.01 to 0.03 eV. The possibility of having a phonon absorbed in the process

of photon absorption can occur if the temperature is high enough that the phonon is thermally excited within the crystal[38].

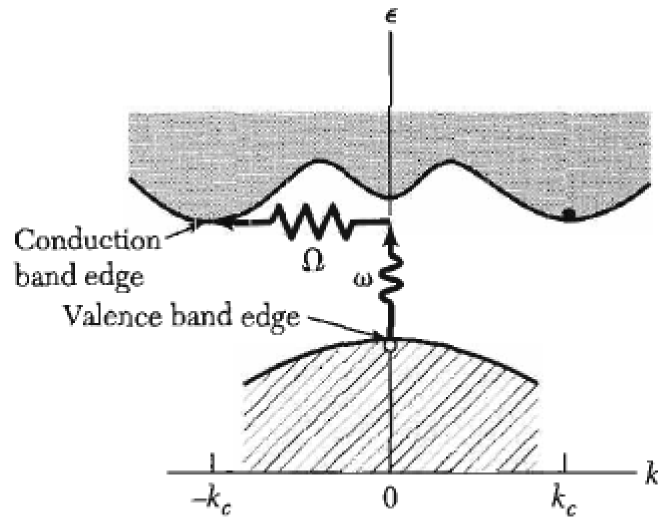

Figure 2.5 An indirect band gap in which the band edges of the conduction and valence bands are widely separated in k-space involve indirect transition which includes a photon as well as a phonon. The threshold energy for the indirect process is greater than the true band gap. The absorption threshold for the indirect transition between the band edges is at $\hbar\omega = E_g + \hbar\Omega$ where Ω is the frequency of an emitted phonon of wave vector $\mathbf{K} = -\mathbf{k}_c$. At higher temperatures phonons are already present; if a phonon is absorbed along with a photon, the threshold energy is $\hbar\omega = E_g - \hbar\Omega$. The figure and caption is adapted from Kittel[38].

2.2 Fe-Si (β-$FeSi_2$) Semi-conductor Material System

The semi-conducting β-$FeSi_2$ silicide is the most studied semiconducting silicide due to the prospects of this material for optoelectronic applications due to the assumption that it has a direct band-gap of around 0.8 eV. While there are a lot of data on this, it is still difficult to define the exact nature and value of β-$FeSi_2$ silicide's energy gap clearly. According to Filonov et al., the band structure of this material is shown in Figure 2.6, as calculated by the Linear Muffin-Tin Orbitals (LMTO) method.[40] In this calculation an input of a base-centered orthorhombic unit

cell with a *Pbcn* space group had been used for the β-$FeSi_2$.[40]

Sometimes one can speak in terms of a quasi-direct band-gap when speaking about the nature of the band-gap in the β-$FeSi_2$ band structure, because there is a direct band-gap at the Λ point which is in the middle between the Γ and the Z points as one can point out in the band structure in Figure 2.6. The energy value of this direct gap is 0.742 eV. However, at the Y point, there is also a conduction band minimum which is only 8 meV higher than the one at the Λ point, which corresponds to a direct gap of 0.82 eV at the Y point. Consequently, due to the small difference in energy of the conduction band minima at the Y and Λ points, it becomes not easy to exactly characterize and define the nature of the gap. Hence, one can speak in terms of a quasi-direct band-gap. It is worthwhile mentioning that theoretical calculations of the nature and value of the energy gap of this material vary amongst each other as published in references[41-45] other than the one above by Filonov et al.[40] which is a good representation of the band structure, especially taking into consideration the nature and values of the energy gaps reported experimentally which are mentioned below.

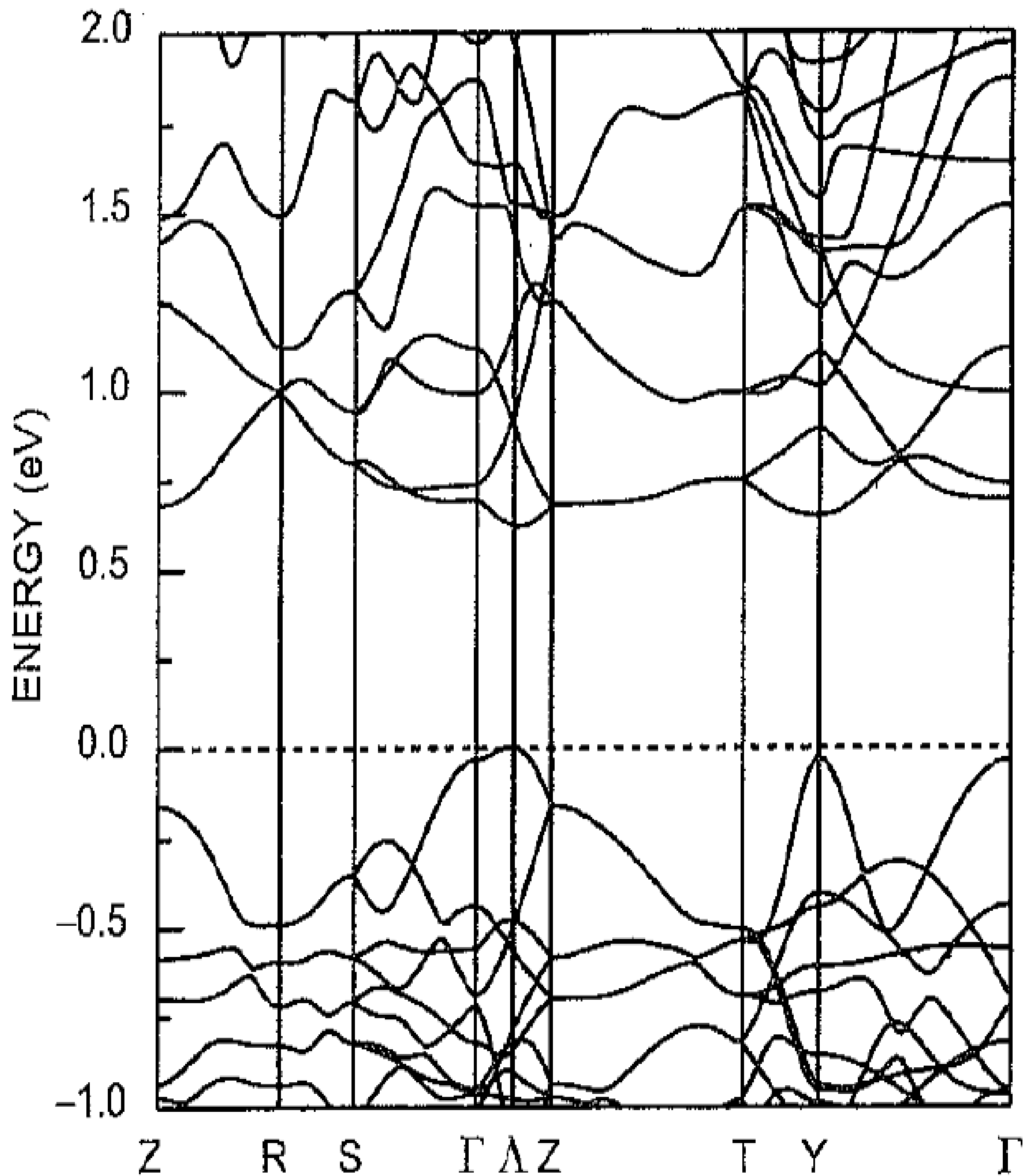

Figure 2.6 The electronic band structure of β-$FeSi_2$ as calculated by the LMTO method,[40] showing the direct/quasi-direct nature of its bandgap.

Experimental reports of band-gap energy values and nature of β-$FeSi_2$ also vary quite a bit amongst each other. For example, optical absorption measurements confirmed the direct

transition in the range of 0.7-1.0 eV. Also, experimentally, Filonov et al. shows indirect absorption edge energies in the range of 0.53-0.81 eV.[40] Additionally, optical data show direct energy gaps of 0.89 eV according to Ozvold et al.,[46] 0.90 eV according to Giannini et al.,[47] 0.92 eV according to Lefki et al.[48] Resistivity measurements show the energy gap values of 0.98 eV according to Isoda et al.,[49] 0.88±0.04 eV according to Ware et al.,[50] and 0.95 eV according to Kojima et al.[51]

At this point, the band-gap value and nature of β-$FeSi_2$ according to the vast majority of the theoretical and experimental studies, report that there is a direct energy gap of 0.87 eV.

2.3 Ru-Si (Ru_2Si_3) Semi-conductor Material System

As outlined in section 1.2.2, Ru_2Si_3 is part of a family known as the Chimney-Ladder compounds. These materials exist in two phases: (i) a low temperature orthorhombic structure with a *Pbcn* space group; (ii) and a high temperature tetragonal structure with a $P\bar{4}c2$ space group.[52] The low temperature orthorhombic structures are studied more due to their prospects for applications. As for orthorhombic Ru_2Si_3, it is a direct band-gap semi-conductor according to Wolf et al., Henrion et al., and Filonov et al.[53-55] Figure 2.7 shows the band structures.[55]

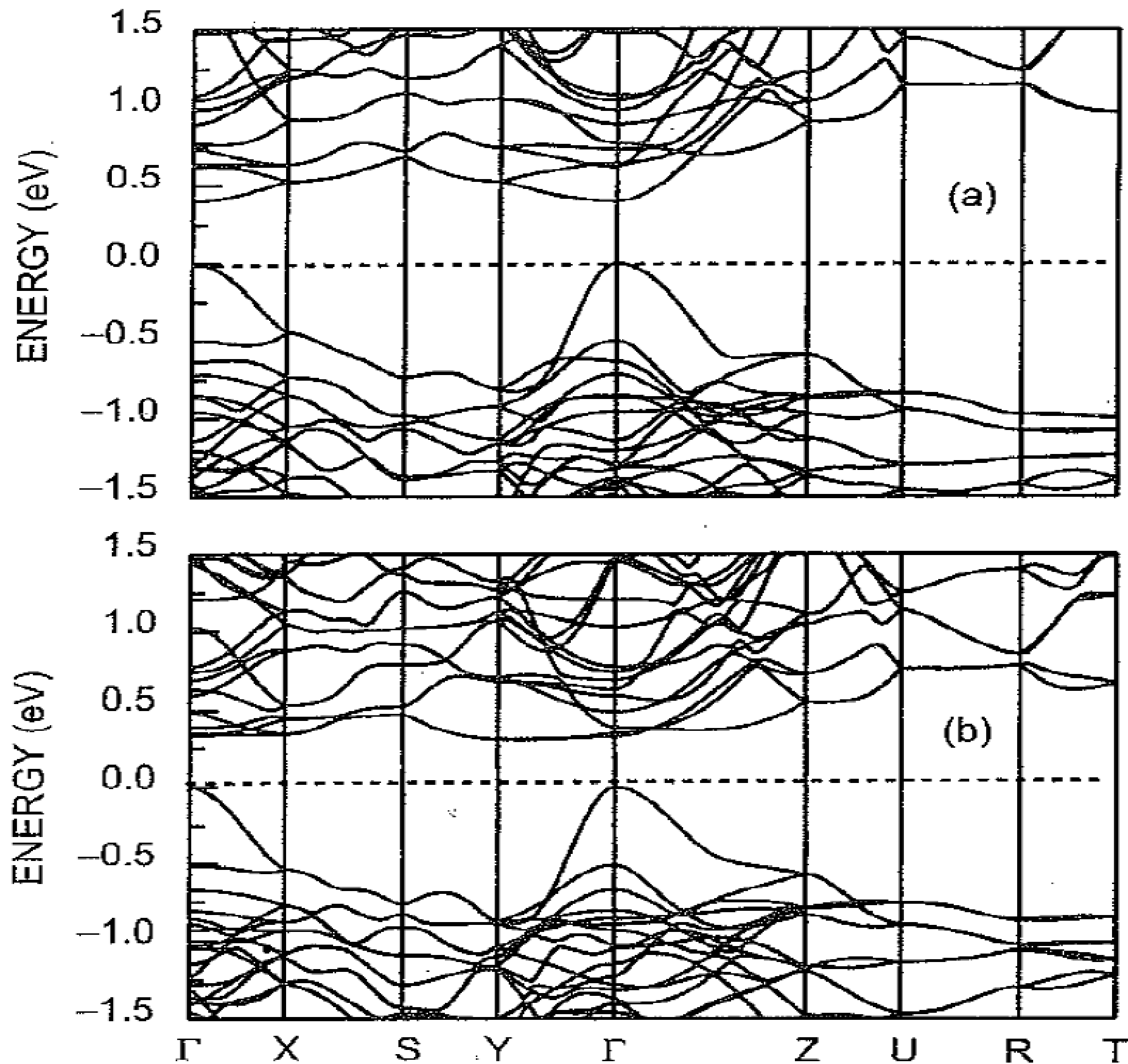

Figure 2.7 (a) The band structures of orthorhombic Ru_2Si_3, as calculated by the LMTO method,[55] showing its clear direct transition at the Γ point. (b) The band structures of orthorhombic Ru_2Ge_3, as calculated by the LMTO method.[55]

While Figure 2.7 shows the band structures for both orthorhombic Ru_2Si_3, and Ru_2Ge_3 for comparison purposes,[55] this work is only focused on and concerned with Ru_2Si_3. As indicated in Figure 2.7 (a), there is a direct transition at the Γ point. Table 2.1 shows the band-gap energy values and their nature for orthorhombic Ru_2Si_3 as calculated theoretically by the LMTO and the Full-Potential Linear Augmented-Plane-Waves (FLAPW) methods, and experimentally by

temperature dependent Resistivity measurements. Both theoretical calculations and experimental observations are according to the mentioned and tabulated references in the table. It is worth mentioning that the high-energy tetragonal Ru_2Si_3 has an experimental (Resistivity measurements) band-gap of 0.44 eV.[52]

Theoretical Calculations			**Experimental Temperature Dependent Resistivity Measurements**	
Method	E_g (eV)	References	E_g (eV)	References
LMTO	0.41-direct	Filonov et al.[55]	0.70	Susz et al.[52]
LMTO	0.42-direct	Henrion et al.[54]	1.08	Vining et al.[56]
FLAPW	0.42-direct	Wolf et al.[53]	1.19	Ohta et al.[57]

Table 2.1 Bang gaps nature and energy value in orthorhombic Ru_2Si_3

2.4 Os-Si (Os_2Si_3 and $OsSi_2$) Semi-conductor Material System

Os_2Si_3 is iso-structural to orthorhombic Ru_2Si_3. It belongs to the same *Pbcn* space group. Its band structure is also similar to that of orthorhombic Ru_2Si_3, as shown in Figure 2.7 (a). According to theoretical calculations using the LMTO method,[55] it is a direct band-gap semi-conductor with a direct transition at the Γ point. The energy value of this theoretical band-gap is 0.95 eV. Experimentally, according to temperature dependent resistivity measurements, it is a semi-conductor which has a band-gap[58] of 2.3 eV which is not only the highest among all semi-conductor silicides, putting orthorhombic Os_2Si_3 as a wide-band-gap semi-conductor, but also it is more than twice as much as the theoretically calculated one, as mentioned above.

$OsSi_2$ is iso-structural to orthorhombic β-$FeSi_2$. It belongs to the *Cmca* space group. Theoretical calculations by the LMTO method[42] of this material's band-gap identified it as a semi-conductor with an indirect gap of 0.06 eV. However, other theoretical calculations by the same LMTO method,[59] finds it to have an indirect band-gap of 0.95 eV and a direct transition at the Y point, with an energy gap value of 1.14 eV. Figure 2.8 shows the band structure of $OsSi_2$ as calculated by the LMTO method.[59]

The later theoretical calculations by Filonov et al. are closer to the experimentally reported band-gaps of this material.[59] Experimental reports identify this material as a semi-conductor over a wide temperature range. Electrical and optical measurements show that energy gap is 1.4 eV according to Schellenberg et al.,[58] and 2.0 eV according to Mason et al.[3] Table 2.2 shows the band-gaps nature and energy values of $OsSi_2$ as reported from theoretical calculations and experimental results with the tabulated reference for each one.

LMTO calculations		**Optical (Reflectance) measurements at room temperature**		**Temperature dependent Resistivity measurements**	
E_g (eV)	References	E_g (eV)	References	E_g (eV)	References
0.06-indirect	[42]	2.0	[3]	1.8	[3]
0.95-indirect	[59]			1.4	[58]
1.14-direct	[59]				

Table 2.2 Band-gaps nature and energy values of $OsSi_2$ as reported from theoretical calculations and experimental results.

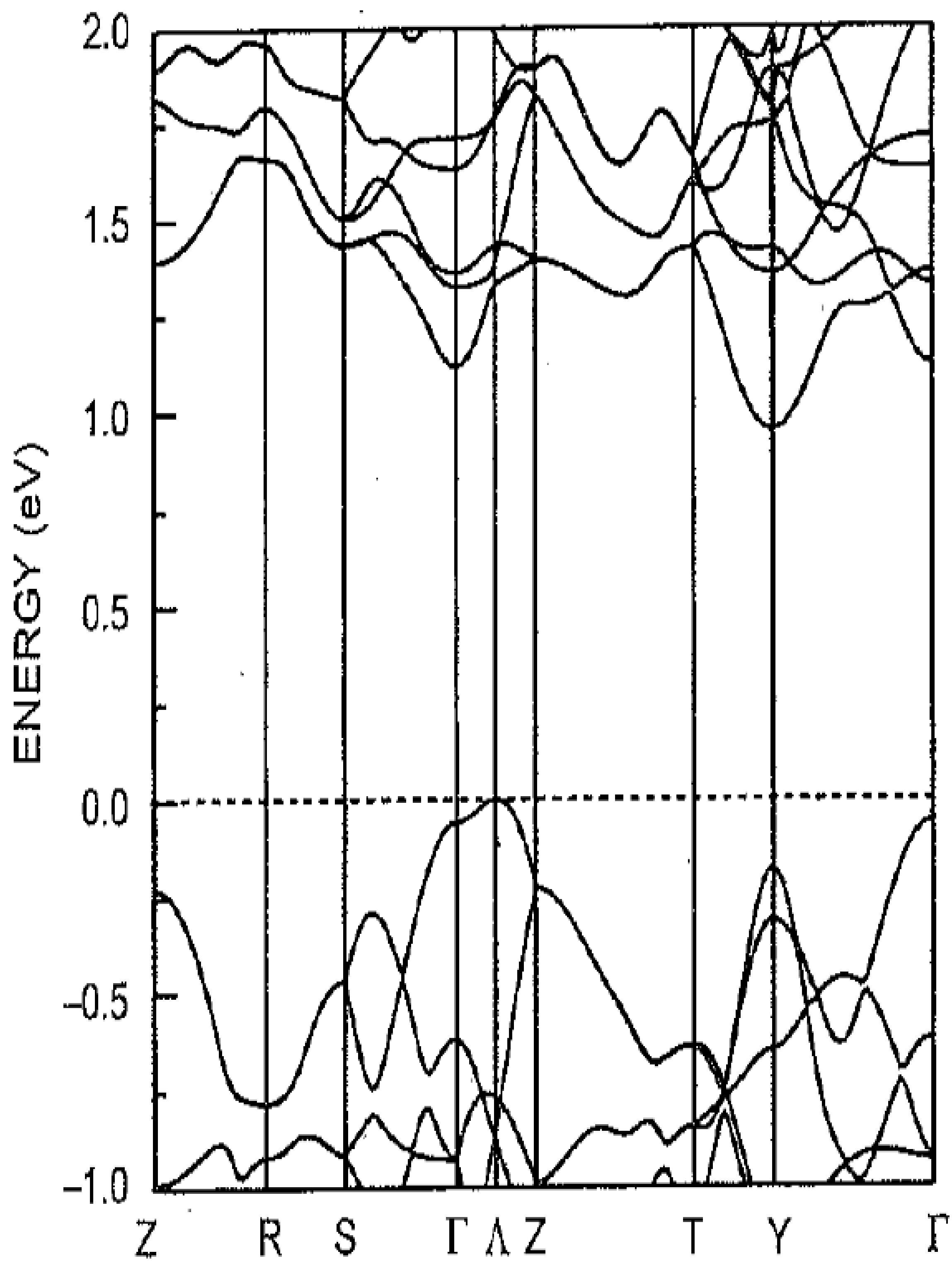

Figure 2.8 The band structure of $OsSi_2$ as calculated by the LMTO method,[59] showing a direct transition at the Y point.

CHAPTER 3

TECHNIQUES AND THEIR FOUNDATION

3.1 Molecular Beam Epitaxy

Molecular beam epitaxy (MBE) is a technique used for the growth of high quality epitaxial layers[60]. MBE was developed by Alfred (Al) Cho of Bell Laboratories in the late 1960's. The most important key factor that differentiates MBE from other growth methods is the fact that it allows for precise control of the growth of a single crystal layer in a non-equilibrium environment inside what is called the MBE chamber. The term non-equilibrium environment, from a physics perspective, means that the nature of the MBE growth method is not limited by thermodynamic equilibrium. This fact is contrary to how other growth methods such as liquid phase epitaxy and vapor phase epitaxy are, in which growth proceeds in accordance to thermodynamic equilibrium[61]. In other words, MBE is distinct from other vacuum deposition methods and techniques because of the incomparable precision allowed through manipulating the various growth conditions[5] regardless of thermodynamic equilibrium.

MBE was first used for the growth of gallium arsenide (GaAs) epitaxial layers and later through the years, it became a preferred growth method in industry as well as academia. MBE is employed for the growth of many materials including metallic, semi-conducting, and insulating materials as well as high quality multi-layer devices[5].

The process by which different elements are deposited on the substrate is evaporation. Evaporation of the elements from their respective sources can be either via heating the effusion cells containing the desired elements, or by directing an electron beam (e-beam) onto the source containing the desired elements causing their evaporation. A schematic diagram for

an MBE growth chamber with one Knudsen effusion cell and one e-beam evaporator for Si is shown in Figure 3.1.

The elements/compounds are evaporated into atomic or molecular beams directed at the substrate. The substrate is temperature controlled crystalline material. All of this occurs in an ultra-high vacuum (UHV) environment inside the MBE chamber[5]. These incident beams of atoms or molecules on the crystalline substrate continue its crystal structure making up an epitaxial layer. If the crystal structure of the new epitaxial layer is the same as that of the substrate, then the process is called homoepitaxy. Whereas, if the crystal structure of the new epitaxial layer is different from that of the substrate, then the process is called heteroepitaxy[5].

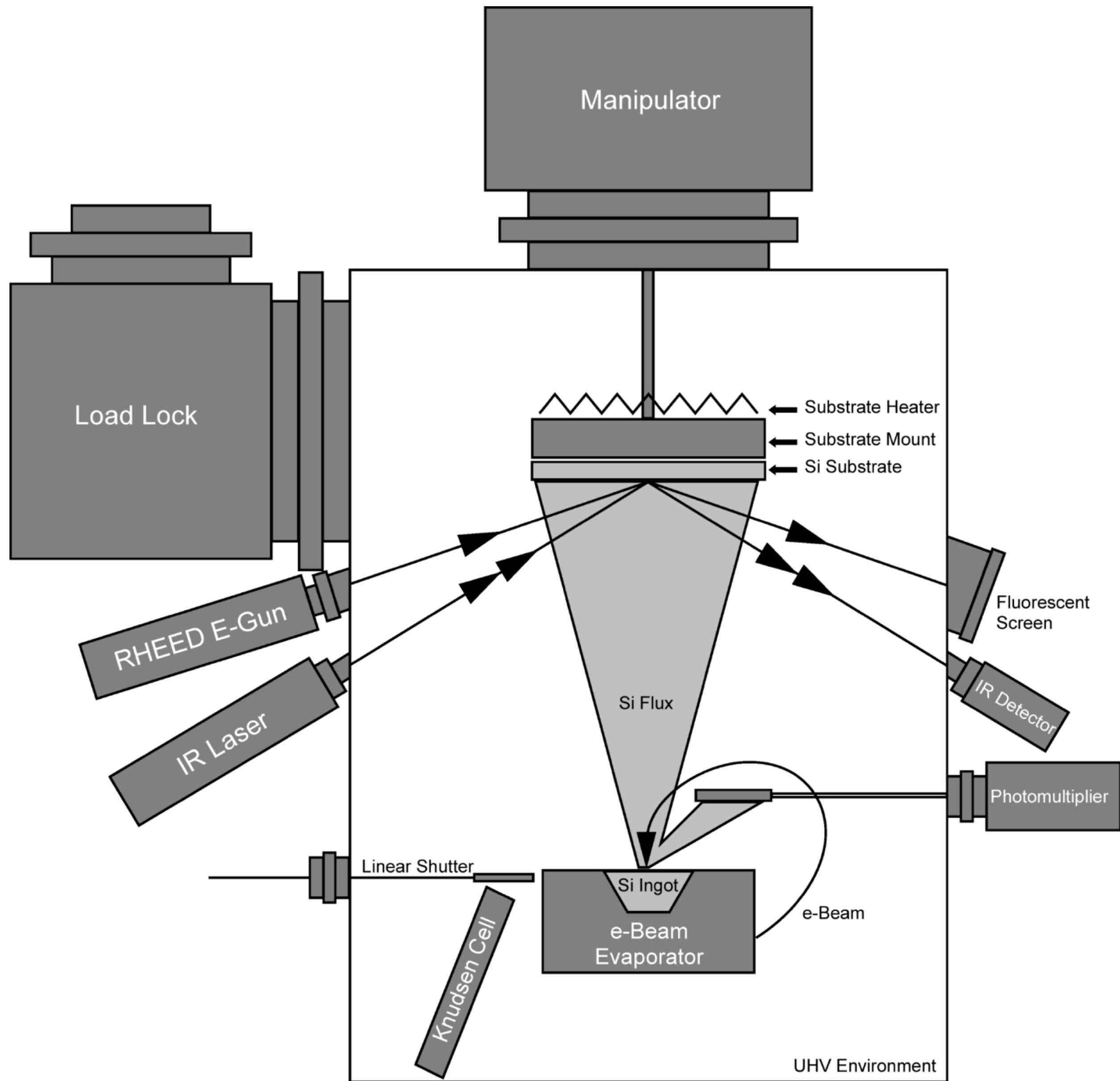

Figure 3.1 A schematic diagram for an MBE growth chamber with one Knudsen effusion cell and one e-beam evaporator[5]

Heteroepitaxy involves such important considerations such as lattice mismatch and strained layers. This depends on whether the grown epitaxial layer is coherent or incoherent with the substrate. Also, there are several MBE growth modes but primarily there are three main growth modes: (a) island-like growth which is termed Volmer-Weber mode, (b) layer-by-

layer growth which is termed Frank van der Merwe growth mode, and (c) layer-plus-island growth which is termed the Stranski-Krastanov (SK) growth mode which is a mixture of the two previous growth modes. Figure 3.2 illustrates these growth modes at various amounts of surface coverage (Θ). The Volmer-Weber mode is simply where the bonding of the film is stronger than the bonding to the surface of the substrate resulting in the island-like growth[5]. The Frank van der Merwe growth mode results in single layers being formed and filled before a new layer is started. This is because the epitaxial film preferentially bonds to the substrate. If it happens and molecules start new layers before the previous layer is complete, these molecules are able to move around and relocate themselves into the previous unfilled layer, due to thermal energy[39].

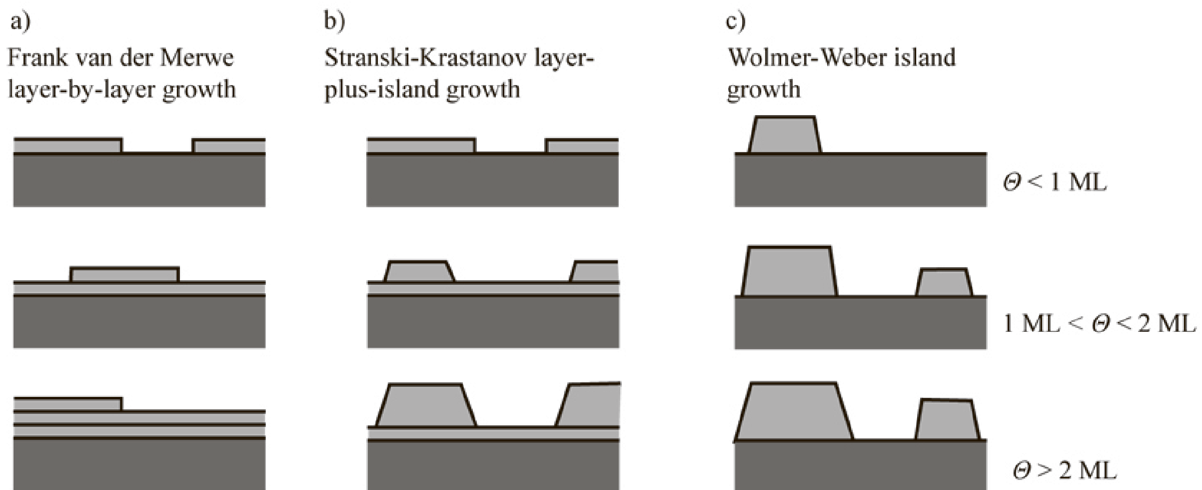

Figure 3.2 Schematic diagram of the three primary modes of epitaxial growth: (a) Frank van der Merwe (layer-by-layer), (b) Stranski-Krastanov (layer-plus-island), and (c) Volmer-Weber (island-like growth)). Θ is the number of monolayers (ML)[62]

The Stranski-Krastanov growth mode is an interesting combination of both of the previous growth modes where at the beginning, layer-by-layer growth occurs, but due to the

film strain being high, this results in subsequent island growth at or after what is commonly referred to as the critical thickness or critical height is achieved. This is due to the elastic energy being accumulated in the growing film. At that particular critical thickness, the free energy of the film can be lowered if the film breaks into isolated islands, so the tension resulting from the accumulated elastic energy can be relaxed laterally. This critical height/thickness depends on several physical aspects such as the size of the lattice mismatch, Young's moduli, and surface tensions. The mode of MBE growth of a certain material system depends on the many adjustments to the growth conditions that can be controlled. One has to remember that MBE is very distinct from other vacuum deposition techniques due its extremely slow growth rate in an UHV environment while allowing for the precise control over virtually all of the growth conditions.

3.2 Reflection High Energy Electron Diffraction

Reflection high energy electron diffraction (RHEED) is a standard *in situ* technique for monitoring MBE growth due to its natural compatibility with MBE[63]. RHEED is a distinguished technique as it is a strictly surface sensitive characterization technique using electrons with high energy, whereas low energy electron diffraction (LEED) for example, is also a surface sensitive characterization technique using low energy electrons. Therefore, RHEED is extensively used to determine two-dimensional versus three-dimensional epitaxial growth, periodicity, and surface roughness[63].

There are three main components of a basic RHEED system[64] and they are: (a) an electron source (gun), (b) a photo-luminescent detector screen and (c) a sample with a clean

surface. The idea is quite simple; a high energy electron beam is generated by the RHEED electron gun whereby this electron beam strikes the surface of the sample at a grazing (low) angle to the crystal surface, causing it to diffract with the surface atoms. The diffraction pattern is viewed on a display screen. This diffraction pattern provides direct information about the surface reconstruction as well as the shape of the surface. Surface reconstruction analysis via RHEED is explained later in this section.

It should be noted that energy of the electron beam generated by the RHEED gun is typically between 5-100 keV. The angle of incidence of the high energy electron beam onto the sample crystalline surface is less than 3^0. Because of the small angle of incidence, the component of the electron momentum perpendicular to the crystal surface is small, resulting in the electrons interacting only with the very surface of the sample (the first one or two atomic layers). In other words, the grazing angle of the incident electrons on the crystal surface allows them to escape the bulk of the sample and to reach the detector. Consequently, the atoms at the sample surface diffract (scatter) these incident electrons due to the wave-like properties of electrons.

The diffracted electrons undergo constructive interference at specific angles. The diffracted electron waves created by constructive interference hit the screen, creating specific diffraction patterns according to the particular surface features of the sample. The factors affecting the pattern of the diffracted electron include the crystal structure, spacing of the atoms at the sample surface and the wavelength of the incident electrons. If the electrons interact with a two-dimensional lattice, this results in the extension of the reciprocal lattice points into rods, which are perpendicular to the real surface[63]. These rods are often termed,

streaks. However, if the electrons interact with three-dimensional (rough or hillock-like surface) then the diffraction pattern would remain as points and would not be extended into streaks. Thus, a streaked diffraction pattern on the RHEED screen is indicative of a two-dimensional growth and surface while a dotty pattern indicates three dimensional growth and surface.

RHEED can be used to observe reconstructions of crystalline surfaces[63]. Reconstruction of a surface is the reordering of the surface atoms within the outer layers. This reordering can change the periodicity of the outer layer, and hence a change in the reciprocal lattice rods and modification in the diffraction pattern shown on the RHEED screen. If the surface reconstructs to a lower symmetry than the bulk crystal, then this will create extra diffraction lines in the viewed RHEED pattern. In that case, images of the RHEED pattern at different azimuths need to be observed in order to determine surface symmetry. Figure 3.4 shows a RHEED pattern for Si buffer layer during MBE growth illustrating a typical Si 2x1-reconstruction.

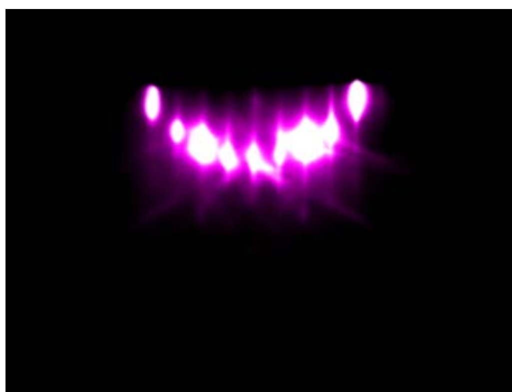

Figure 3.3 RHEED pattern for Si buffer layer during MBE growth illustrating a typical Si 2x1-reconstruction

3.3 X-ray Absorption Spectroscopy / X-ray Absorption Fine Structure

X-ray absorption spectroscopy (XAS)[65,66] is a unique structural technique which is

extensively used to determine the local structure of a material system whether these materials are solids (condensed matter), liquids, or gases. Determination of the local structure of a material system is with respect it to its local geometry, such as local coordination of atoms and nearest neighbor distances, as well as local electronic structure, such as phase and metallic versus semi-conducting behavior, etc. XAS is also very sensitive to elemental selectivity due to the physical premise upon which XAS operates, which is explained later in this section. XAS employs a tunable x-ray source that can provide intense x-ray beams, and hence XAS are most likely to be conducted at synchrotron facilities. The method to tune the photon energy of the used x-rays for XAS is via a monochromator. This monochromator is a crystal, sometimes a double-crystal monochromator is used for x-ray beam tuning. Tuning of the photon energy of the x-ray beam is a critical step in XAS, in order to be able to eject photoelectrons out of the core central atom of the material to be characterized.

The physical premise upon which x-ray absorption spectroscopy is based is quite interesting. Every element/material has its own unique set of absorption edges that depends on the binding energies of its electrons. When the incident photon energy of the x-ray beam is very closely tuned to and matches the binding energy of an electron with in an atom in the sample, the number of photons absorbed by the sample increases significantly. This very fact leads to an absorption edge on the XAS spectra. So, an x-ray beam that is incident on and very closely tuned to an absorption edge of a particular material/element, leads to the absorption of these photons which consequently ejects a core photoelectron from the absorbing atom within that material/element. As a result, the absorbing atom now is excited due to the presence of a core hole instead of the ejected photoelectron. According to the law of conservation of energy,

the energy of the incident photon equals the energy of the ejected photoelectron plus the binding energy of that core electron. The notation given to this absorption edge depends on the state of the core electron, for example, if the excited core electron is in the 1S state, then absorption edge is given the notation K-edge according to the principal quantum numbers, and so on. It is inevitable for the ejected photoelectron to start interacting with the other electrons belonging to the other neighboring non-excited atoms.

One can view this whole process in terms of waves, due to the wave-like nature of electrons. The ejected photoelectron can be described as a wave while the neighboring non-excited atoms can be described as scattering points. At this point, backscattering of the outgoing photoelectron by neighboring atoms results in sinusoidal oscillations of what is called the absorption coefficient (μ). These sinusoidal oscillations are an interference pattern where the peaks correspond to areas of constructive interference while dips correspond to areas of destructive interference. μ is given by the following equation:

$$\mu = [- \ln (I_t/I_0)] / \chi$$

Where I_t is the number of x-ray photons that are transmitted through a sample, I_0 is the number of x-ray photons shone on the sample, and χ is the thickness of the sample.

Hence, the wavelength of the ejected photoelectron that is now backscattered by neighboring atoms of that material/element depends on and is a function of certain key physical quantities of both the backscattering atoms and of the incident photon. These key physical quantities are the phase and energy of the backscattered wave belonging to the backscattering atom, and the energy of the incident photon. Due to the wave-like nature of

electrons, it is worth mentioning that the phase and amplitude of the backscattered wave depend on the type of the backscattering atom and the distance by which the backscattering atom is neighboring the central atom. Now, it becomes evident that the XAS spectra formed by these sinusoidal oscillations, resulting from the backscattering of the outgoing photoelectron by neighboring atoms, depends on the absorbing atomic species; their type, chemical coordination and local bonding environment, nearest neighbor distances, and local electronic structure. Thus, XAS spectra provide unique elementally sensitive information pertaining to the material/element being characterized.

Figure 3.5 illustrates a XAS spectrum of pure osmium (Os). The XAS plot shows the absorption versus energy of Os. There are two regions on the spectrum, the first one is x-ray absorption near edge structure (XANES) and the second is extended x-ray absorption fine structure (EXAFS). X-ray absorption fine structure (XAFS) is the combination of both of these two regions. The XANES features only around 50 eV from the absorption edge of a material/element, while EXAFS features 50 – 1000 eV above the absorption edge. XANES primarily provides sensitive information pertaining to the bonding environment and oxidation state, while EXAFS provides more sensitive, in depth and elementally specific information pertaining to local structure, nearest neighbor distances, etc. as mentioned earlier in this section.

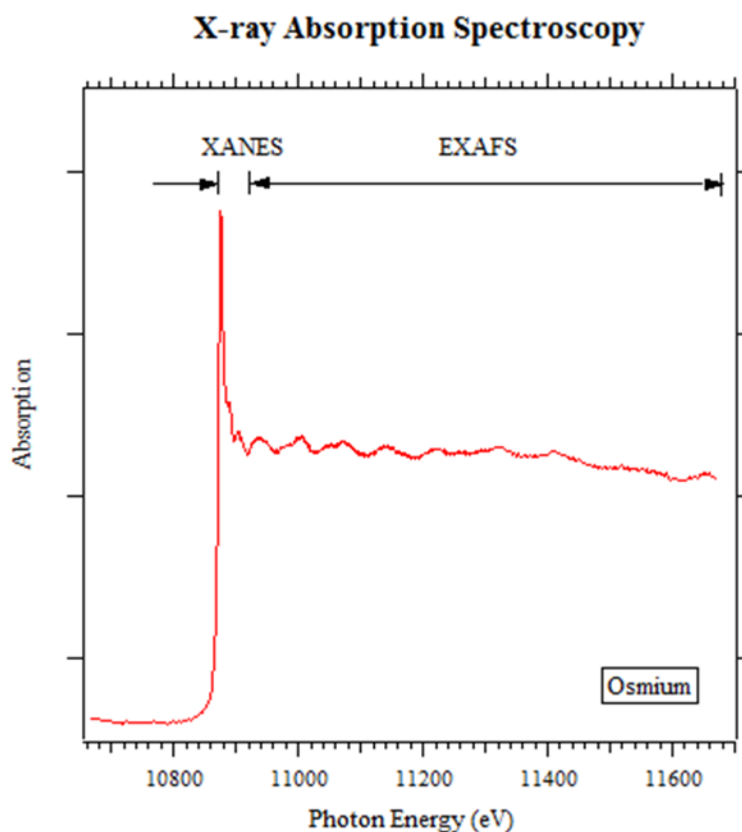

Figure 3.4 The XAS spectrum of pure osmium (Os). The XAS plot shows the absorption versus energy of Os as well as the XANES and the EXAFS regions in the Os XAFS spectrum.

It should be noted that the Fourier transform of the EXAFS data gives the nearest neighbor distances of the backscattering atom[67].

While x-ray diffraction (XRD) and XAS/XAFS are both structural characterization techniques that employ the use of x-rays, XAS is an interdisciplinary technique that is unique because of its sensitivity to the details of the local structure in many different material systems, in comparison with XRD. These material systems can be condensed matter (solids), liquids, or gases.

3.4 Atomic Force Microscopy

Atomic force microscopy (AFM) is a very high resolution imaging technique that is not used for imaging but also for measuring the roughness of a surface, and also can manipulate matter at the nano-scale. AFM was introduced by Quate and Gerber in 1986. In very layman terms, AFM provides information about the surface of a material by feeling its surface by a probe. In the following lines, the mechanical probe's components, the different mechanisms of feeling the surface, and the method(s) of detecting the probe deflection, are explained.

The AFM's mechanical probe is a cantilever with a tip at its very end which is used to scan the surface. The cantilever can be made out of silicon or silicon nitride in most cases and is held by a holder chip or a plate specially designed for AFMs[68]. The tip is a sharp and curved piece; its radius of curvature is a few nanometers. The idea behind how an AFM works is quite simple. As the tip is brought close to the sample's surface, the tip will move causing the cantilever to deflect. This cantilever deflection is caused and a function of the interaction between the tip and the surface of the sample. Then AFM measures that deflection. This can be physically understood by Hooke's law[69]. The idea is for AFM to measure this deflection at many points on the surface, which can later be plotted and mapped out. The forces between the tip and the sample's surface that cause the deflection of the cantilever can be of many types depending on the physics of the situation. For instance, the forces can be Van der Waals forces, chemical bonding, electrostatic forces, etc. As the tip scans the sample's surface, if the tip is maintained at a constant distance from the surface, which will inevitably cause damage to the sample's surface and to the tip. Since the sample's roughness might cause the tip to hit a part of the surface causing this damage. Consequently, there are three main safe mechanisms, or

modes, by which AFM perform its function while preventing to a great extent any damage to the tip or to the sample's surface being characterized. They are called; (a) contact (static) mode, (b) tapping (dynamic) mode, and (c) non-contact (also dynamic) mode[70]. Figure 3.6 (a), (b), and (c)[71] shows the three main AFM modes.

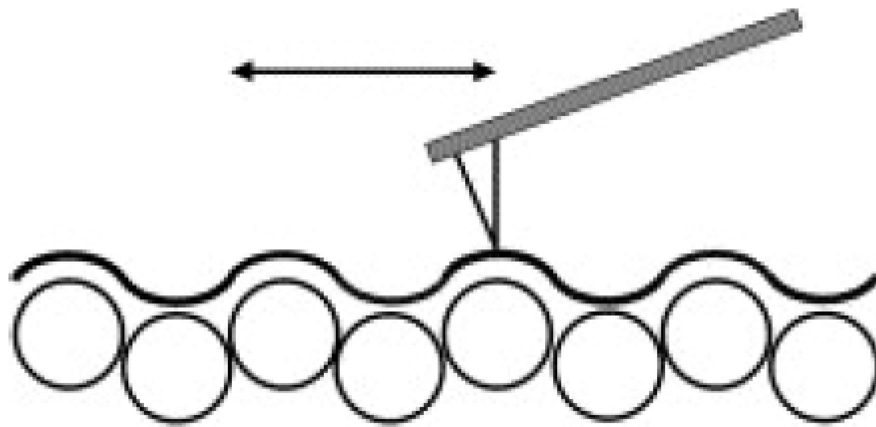

(a) Contact mode

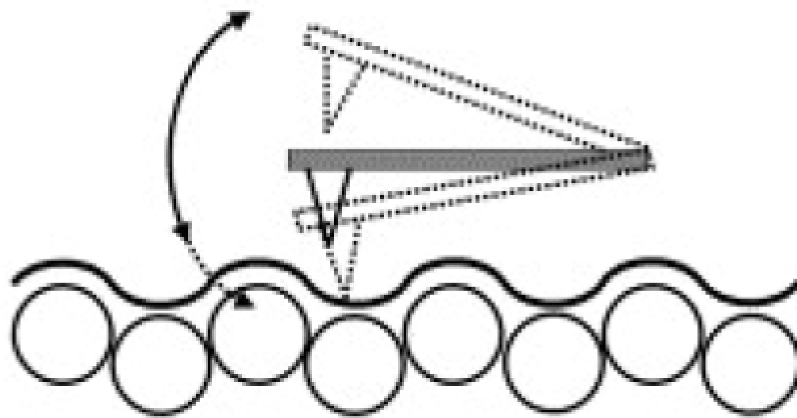

(b) Tapping mode

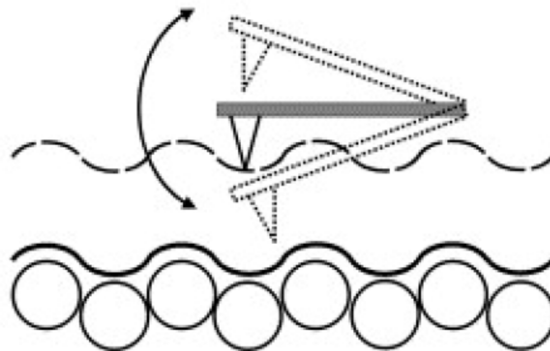

(c) Non-contact mode

Figure 3.5 A Schematic diagram showing the three main AFM modes; (a) Contact mode (static mode), (b) Tapping mode (dynamic mode), and (c) Non-contact mode (also a dynamic mode)[71].

The contact mode is where the tip is always in contact with the surface of the sample

and in layman terms, dragged across the surface to scan it and provide its information. This mode is used when the force between the tip and the surface is repulsive. The tapping mode[72] is where the cantilever is designed to move up and down in an oscillatory motion with a particular frequency. This frequency is near the cantilever's resonance frequency. The piece of equipment by which this is achieved is a piezoelectric element placed in the tip holder. The oscillation amplitude is ranges from 100 to 200 nm. As the tip gets close to the sample's surface, the forces between the tip and the surface cause the amplitude of the cantilever's oscillation to decrease. In other words, this change in the amplitude of oscillation as a result of the tip coming to contact with the surface of the sample, due to the forces between them, is recorded, imaged, and mapped out through the scan. It should be noted that the tapping mode is very gentle in comparison with the contact mode which can cause damage to the AFM tip and/or the surface of the sample. The non-contact mode[73] is also a dynamic mode where the AFM tip does not come in contact with the sample surface. Just like the tapping mode, the cantilever is designed to oscillate either at or above its resonant frequency. However, unlike the tapping mode, the cantilever's amplitude of oscillation is less than 10 nm and can even be a few picometers. The forces between the tip and the sample's surface, mostly Van der Waals forces, are strong enough to cause the cantilever's amplitude of oscillation to decrease. Once this decrease occurs, the AFM system keeps a fixed frequency by adjusting the average distance from the tip to the surface. The measurement and the recording of this distance at each data point enable the scanning software to establish to image the sample's surface and gather information about its roughness, etc. It should be noted that the non-contact mode is also non-damaging neither to the AFM tip nor to the sample's surface. There are various methods of

measuring and detecting the probe's deflection, the most common one is called beam deflection measurement which involves a solid state diode laser reflected off the cantilever. Other methods include piezoelectric detection, piezoresistive detection, and laser Doppler vibrometry.

3.5 X-ray Photoelectron Spectroscopy

X-ray photoelectron spectroscopy (XPS) has an exciting history since it goes back to H.R. Hertz when he discovered the photoelectric effect in 1887. Some years later, Albert Einstein was able to explain this phenomenon in 1905. But it wasn't until 1954 when a Sweden scientist Kai Siegbahn revealed the true potential of XPS when he recorded a high-energy-resolution spectrum of sodium chloride (NaCl) after making significant improvements on XPS equipment[74]. Kai Siegbahn named XPS, electron spectroscopy for chemical analysis (ESCA). In 1969, Siegbahn worked with a few engineers from Hewlett-Packard (HP) to commercialize XPS and produce the first commercial XPS with a monochromatic x-ray source. He later received the Nobel Prize in 1981 for his work on the development of XPS as a characterization technique.

The physical premise upon which XPS is based is significant. It is the photoelectric effect. When x-rays of known photon energies/wavelengths are incident and penetrate the sample. The binding energy of the emitted electron from the sample can be calculated by the law of conservation of energy given by the following equation:

Binding energy of the emitted electron = Energy of incident photon - (Kinetic energy of the emitted electron + ϕ)

Where; ϕ is the work function. It is essentially a correction factor due to the fact that

the photoelectron loses a very small portion of its energy when it gets absorbed by the XPS detector.

It should be noted that the XPS detector is positioned around one meter away from the sample being characterized. This simple fact is a very important reason why XPS is a surface-only sensitive technique. While incident x-rays have a penetration depth range of 1-5 micrometers into the bulk of the sample, those emitted photoelectrons which are deep into the sample are in reality never detected by the XPS detector since they never actually escape the sample itself. One has to realize that the XPS detector only detects those emitted photoelectrons which succeed in escaping from the sample, travel through the vacuum of the XPS equipment, and finally reach the detector to be absorbed. During this process, distance, and path, the photoelectron can go through various impedes in the sample itself such as entrapments in other excited states within the sample, inelastic collisions, or being recaptured. As the depth of emitted photoelectron within the sample increases, all of the above mentioned factors exponentially impede and actually prevent the deeper photoelectrons from escaping the sample. One has to remember that after escaping the sample, the photoelectron still has to possess enough energy in order to travel through the vacuum of the XPS equipment until it reaches the detector and get absorbed (i.e. detected).

An XPS spectrum is usually a plot between the number of detected electrons, as the ordinate, their binding energies, as the abscissa. Elemental selectivity and sensitivity arises from the fact that every element produces signature XPS peaks at signature values of binding energies. This provides clear elemental identification of the existence of that element on the characterized sample's surface. It is worth mentioning that these signature peaks are directly

related to the energy states of the electrons within the atoms such as 1s, 2s, 2p, etc. Ultra high vacuum environments and conditions are employed in XPS setups in order to minimize errors while counting the number of detected electrons and precisely provide percentages of a particular element within the surface being characterized.

XPS characterization can be done to the surface of the samples either in their as received condition which typically involve certain contaminants and surface oxidation due to exposure to the normal atmospheric air environment, or after some treatment to the sample's surface via various methods such as ion beam etching to remove these contaminants from the surface and hence being able to do a depth profile to expose the chemistry of the bulk of the sample.

XPS can characterize and provide elemental composition and chemical and electronic state of the surfaces of many materials such as semi-conductors, glass, ceramics, paper, teeth, etc.

3.6 Raman Spectroscopy

Historically, Raman Effect, which is the basis of Raman spectroscopy[75], was named after Sir C.V. Raman. Sir Raman discovered this effect using sunlight as the light source. His experiment was basically passing sunlight through a monochromator (filter) to get a monochromatic light then passed this monochromatic light in a crossed filter to block it. He noticed that a small amount of this monochromatic light changed its wavelength and passed through the other filter. He won the Nobel Prize for this discovery in 1930.

Raman spectroscopy is an extremely useful technique for the characterization of semi-

conductors. It is very useful to characterize thin films as well as bulk materials. Raman spectroscopy is essentially a scattering technique, and not an absorption technique, that depends on the interaction between electrons and phonons in the local semi-conductor environments.

The physical concept behind Raman spectroscopy, which is Raman Effect, is quite interesting. If a laser, as a source of light, is directed at a molecule. This light will inevitably interact with the chemical bonds and the electrons in the so-called electron cloud of that molecule. This interaction will result in the scattering of this light, what is commonly called a spontaneous Raman Effect. In essence, a light photon excites the molecule from its ground state to a so-called virtual state. This virtual state is not by any means a real discrete energy level, or else the process would be that of absorption. Eventually, the molecule will relax again by emitting a photon. This relaxation will take the molecule to a different state (vibrational or rotational)[75] than its original ground state. Due to this difference in energy between these two states and because energy has to conserved, a shift in that emitted photon's wavelength/frequency occurs in comparison with the excitation photon wavelength/frequency. This shift is termed, Raman shift. Raman shifts can be due to either Stokes Raman scattering or anti-Stokes Raman Scattering. Both of these scattering processes are inelastic, since Raman scattering, by definition, is an inelastic type of scattering due to the transfer of energy that occurs between the photons of the light source and the molecules during their interaction, as explained in the following lines.

A Stokes Raman scattering is where the new energy state of the molecule, after relaxing, is of higher energy than the molecule's original state. In this case, the emitted photon, due to

the molecule's relaxing, will be of lower frequency than the original photon of the light source causing the excitation of the molecule. The reason is the law of conservation of energy. This type of Raman shift in the detected frequency of the photon is then called a Stokes shift. An anti-Stokes Raman scattering is where the new energy state of the molecule, after its relaxing, is of lower energy than its original state. In that case, the emitted photon, due to the molecule's relaxation, will be of higher frequency than the original photon of the light source causing the molecule's excitation. The reason is again, the law of conservation of energy. That type of Raman shift in the detected frequency of the photon is then called an anti-Stokes shift.

The following equation relates the Raman shift, which is a direct outcome of a typical plot of Raman spectra, to the wavelengths of the excitation and that of the Raman spectrum:

$$\Delta\omega = (1/\lambda_0 - 1/\lambda_1)$$

Where $\Delta\omega$ is the Raman shift in units of wavenumber, λ_0 is the wavelength of excitation, and λ_1 is the wavelength of the Raman spectrum.

Typically the source of light used nowadays is a laser. A Raman set up consists of laser, as the light source, a lens, a monochromator, and a detector. The laser is directed on the sample to be characterized. Then the light from the sample's illuminated area passes through the lens for its collection and then through the monochromator to filter out the elastic scattering, which is termed Rayleigh scattering. So that only the Raman scattered light (inelastic scattering) goes through the detector.

3.7 Scanning Tunneling Microscopy

The scanning tunneling microscope[76] (STM) was developed by Gerd Binnig and Heinrich

Rohrer at IBM-Zurich in 1981. Their development of STM earned them the Nobel Prize in 1986. STM is an extremely versatile imaging technique for surfaces at the atomic level. The fact that it's versatile made it usable in many different environments unlike some other techniques where UHV is a condition for their operation. STM can be even used in water, as well as air, and in other environments containing other liquids or gases. STM can operate over a very wide temperature range, from near absolute zero temperature (0 K) to a few hundred ^{0}C[77].

As the name suggests, the physical premise upon which STM rests, is the tunneling effect. More precisely, quantum tunneling. Quantum tunneling in an STM works when a voltage is applied to its scanning tip, and the tip approaches very closely the surface of the sample to be characterized. With the tip being conducting and very close to the surface, a potential difference arises between the tip and the surface. This potential difference leads to a tunneling current through the vacuum that goes from the surface to the tip. This tunneling current depends on and a function of three major factors: (a) the position of the tip, (b) the applied voltage to the tip, and (c) the local density of states of the surface of the sample being characterized[77]. When tunneling occurs between the tip and the surface, the tip's position and voltage applied can be varied for scanning purposes.

STM can operate in two main modes: (a) constant height mode and (b) constant current mode. Constant height mode is when the voltage applied to the tip and height of the tip from the sample's surface are both held constant. The changing variable in this mode is the current. The current adjusts and changes, as it is scanning over the surface, in order to preserve constant voltage. Imaging is done based upon the changing current[78]. Constant current mode is when the changing variable is the height of the tip from the surface. The height is adjusted and

changed by the voltage controlling the height control system which is piezoelectric[62]. Imaging is done based upon the change in the height of the tip from the sample's surface as the tip scans its topography[78]. It should be noted that STM can provide images with resolution around 0.1 nm laterally and 0.01 nm depth-wise[79]. However, the resolution depends on tip's radius of curvature. Tips are normally made out of platinum-iridium, gold, and tungsten[79]. Tips are made so sharp for precise measurements and imagery, to the extent that there is only one atom of the tip's material at its apex[80].

3.8 Scanning Electron Microscopy / Cross-sectional Scanning Electron Microscopy

The historical breakthrough of the scanning electron microscope goes back to 1937, when Manfred von Ardenne invented a microscope that uses a narrow focused beam of electrons to scan a tiny raster area with high magnification. He was also able to get rid of the chromatic aberration. He was able to discuss not only the theory of SEM[81] but also the SEM's detection modes as well as building the first known high magnification SEM. Ardenne' efforts together with the efforts of other groups such as the Zworykin's and the Cambridge groups led to the making of the first commercial SEM in 1965. SEMs are very powerful magnification tools. A SEM can magnify 10 times up to 500,000 times and has enough resolution to clarify details which are 1 nm or less, as well as detailed 3d imaging because of the focused electron beam used.

The physical premise upon which SEM relies is quite simple yet detailed. As a focused beam of electrons scans a sample, it interacts with the sample atoms. This interaction results in more than one type of signals which are detected by their appropriate detector/detecting

mode. The most common type of signal/imaging and detecting mode is by secondary electrons. This happens when the focused beam of electron interacts with the atoms of the sample's surface, exciting them, and leading to the emission of secondary electrons from the atoms at or near the surface of the sample. These secondary electrons are detected by the so-called secondary electron imaging (SEI) detection mode. Another signal/imaging type is by backscattered electrons (BSE). This happens when the focused electron beam interacts with the sample by getting reflected via elastic scattering. This mode is very useful in identifying the elements in the sample because of the signature intensity of the BSE signal detected as it relates to the atomic number of sample being characterized. Therefore, BSE imaging gives information about the elements in the sample. Another important SEM imaging mode is the one by characteristic x-rays coming out of the sample. This happens when the incident focused beam of electrons knocks out a core electron. Consequently, the core hole left behind will be filled by an electron from the sample of a higher energy than the liberated core electron. This results in the releasing of energy and the production of characteristic x-rays that are signature of the composition of the sample being characterized.

CHAPTER 4

MOLECULAR BEAM EPITAXIAL GROWTH OF IRON SILICON GERMANIDE AND CHARACTERIZATION

In this chapter, the structure of iron silicon germanide $Fe(Si_{1-x}Ge_x)_2$ thin films is reported. The Office of Naval Research (ONR) supported the work presented in this chapter, (Contract No. N00014-03-1-0820). The iron silicon germanide thin films are grown by molecular beam epitaxy. The phase and important structural aspects of these films is determined using synchrotron-based x-ray absorption fine structure spectroscopy. Since the β-$FeSi_2$ phase of iron di-silicide is a quasi-direct band gap semiconductor; therefore, it shows promise for optoelectronic applications. According to theoretical predictions, by incorporating Ge into the lattice of β-$FeSi_2$, the lattice constant increases, resulting in a reduction in its band gap with increasing Ge content.[82] The x-ray absorption spectroscopy results and nearest neighbor distances show that the samples are not metallic. Further, the results are consistent with the structure of the crystalline growth of the semiconducting β-$FeSi_2$. It has been also observed that the absorption edge (E_0) slightly increases with increasing Ge content while the nearest neighbor distances slightly decrease with increasing Ge content.

4.1 Experimental Methods and Equipment

4.1.1 Molecular Beam Epitaxy (MBE)

The growth of crystalline materials under ultra-high vacuum (UHV) conditions, which is known as molecular beam epitaxy (MBE), generally gives the best purity and greatest control of the crystalline phase of that material. Since there are multiple stable crystal structures for most of the metal silicides, for instance, there are three stable stoichiometries for iron silicide: Fe_2Si,

FeSi, and $FeSi_2$, and iron disilicide has three known phases, therefore growth of hetero-structures and super-lattices by MBE shows the greatest promise. This technique also can be used to perform band gap engineering (*i.e.*, the tuning of the band gap of a semiconductor by substitutionally alloying one of the constituent elements with a different element).

The state of the art UHV MBE system employed to grow these $Fe(Si_{1-x}Ge_x)_2$ samples is designed by Hans Gossmann and donated by Lucent Technologies. Some of the technical details of which are summarized using a schematic diagram as illustrated in Figure 4.1.

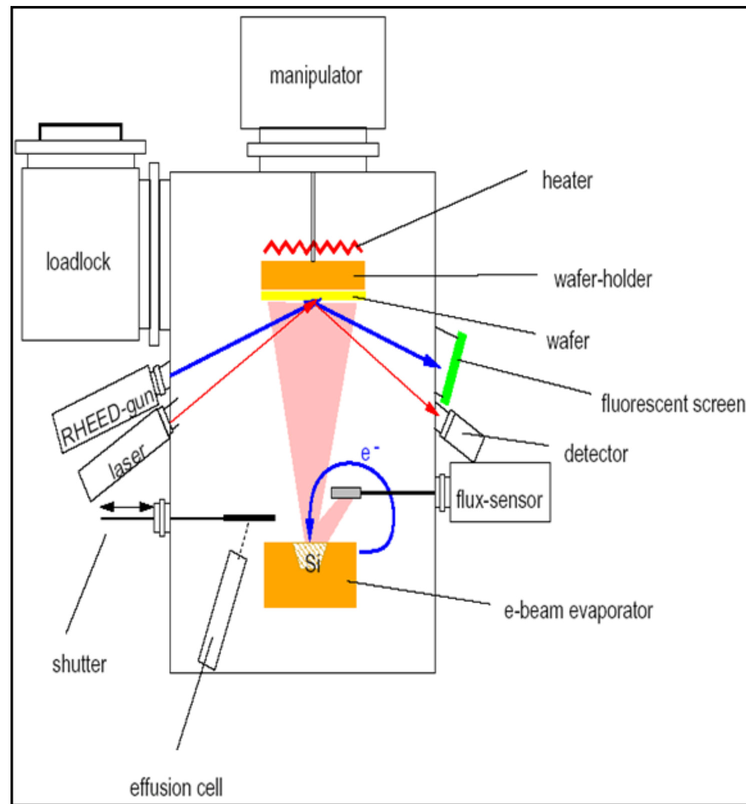

Figure 4.1 State of the art UHV MBE system employed to grow these $Fe(Si_{1-x}Ge_x)_2$ samples is designed by Hans Gossmann and donated by Lucent Technologies.

The Si source is an electron beam (e-beam) deposition source, and so is the Fe source, while the Ge source is a Knudsen effusion cell deposition source. The purity of both the Si and the Ge sources is 6N. The Si source is in a 44 cubic centimeter ingot. A PBN liner is used to evaporate the Ge from its effusion cell. The purity of the Fe source is 3N8, it is in the form of granules. The Fe source is in a 15 cubic centimeter crucible made out of Tungsten. The Fe, Si, and Ge sources are calibrated using Reflection High-Energy Electron Diffraction (RHEED) intensity oscillations as well as Rutherford Backscattering Spectrometry (RBS). Fe and Si are each evaporated from its own respective source in the same stoichiometric ratio of the desired material to be grown. The Fe and Si fluxes are monitored, controlled and stabilized (in the range of ±5%) via optical means, a photo multiplier tube (PMT) signal.

4.1.2 X-ray Absorption Spectroscopy – X-Ray Absorption Fine Structure

The x-ray absorption spectroscopy (XAS) measurements were performed at the synchrotron facility of Louisiana State University, called the Center for Advanced Microstructures and Devices (CAMD) in Baton Rouge, Louisiana, using the double crystal monochromator (DCM) beam line. Images of the DCM beam line are shown in Figure 4.2.

X-ray Beam Line

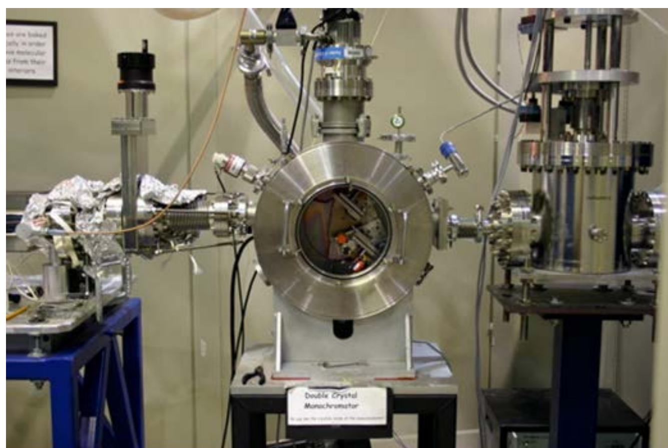

Monochromator

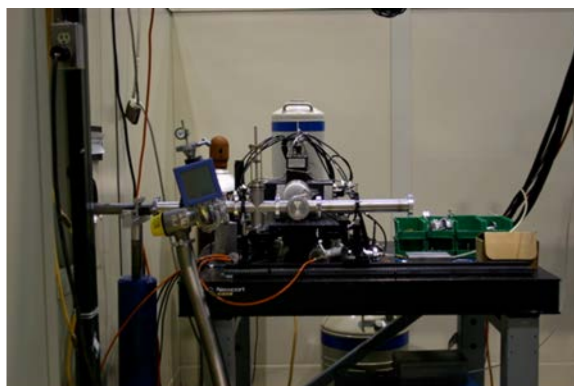

Sample Stage and Detector

Figure 4.2 The DCM beam line facility at synchrotron facility of the center for advanced microstructures and devices (CAMD)

The facility of the DCM beam line has been operational since the fall of 1994. At first, it used the DCM from the Laboratório Nacional de Luz Síncrotron (LNLS) and then later used the DCM from Bonn University. The DCM beam line can collect data of energies as low as 932.5 eV and as high as 20,000 eV. The 932.5 eV corresponds to the Cu LIII edge, and the 20,000 eV corresponds to the Mo K edge. The DCM beam line uses a variety of crystals for its operation. These various crystals have their particular (*2d*) and operate in their particular energy range. Some of these crystals are: the KAP (001) crystal has a (*2d=26.632 Å*) and operates in the energy range of 510 – 1800 eV, the YB_{66} (400) crystal has a (*2d=11.72 Å*) and operates in the energy range of 1170 – 4090 eV, the InSb (111) crystal has a (*2d=7.481 Å*) and operates in the energy range of 1830 – 6400 eV, the Si (111) crystal has a (*2d=6.271 Å*) and operates in the energy range of 2180 – 7640 eV, the Ge (220) crystal has a (*2d=4.00 Å*) and operates in the energy range of 3420 – 11980 eV, the Si (220) has a (*2d=3.840 Å*) and operates in the energy range of 3560 – 12470 eV, and the Ge (422) has a (*2d=2.306 Å*) and operates in the energy range of 5930 – 20770 eV. The Lemmonier-Bonn monochromator is vacuum compatible and its angular range is around 12.5^{o} – 72°. The DCM beam line has a magnet that supplies a radiation of 2mrad to it. The DCM beam line operates in the region of soft x-rays, it has a differential ion pump which allows the beam line's operation within 7 – 13 μm Kapton™ window. There is a photon beam position monitor which controls the position of the beam at all times. The DCM beam line's functionality is very good in the range of 1 keV – 12 keV, the upper limit of this range depends on the drop in the intensity of the source beyond 10 keV, its resolution is 0.5 eV at lower energies while its resolution is 2 eV at higher ones.

The modes of x-ray absorption measurements are transmission mode, fluorescence mode and electron yield mode. According to the measurement mode, the appropriate detector is used. Some of these detectors are: Peltier-cooled Si (Li) detector, 13-element Ge diode array fluorescence detector, and a Lytle fluorescence and electron yield detector.

X-ray absorption fine structure (XAFS) were conducted on the samples in fluorescence and not in transmission due to the relatively thicker Si substrate in comparison with the thin films grown which would have resulted in an attenuation of the detected signal. The Ge (220) crystal monochromator was used which corresponds to a range of energy operation of 3420 eV – 11980 eV and a 2d = 4 Å. A pure metallic Fe thin film sample was used as a reference. Edge energies were set to 7112.00 eV, relative energy boundaries ranged from 200 eV below the edge to 800 eV above the edge. Region step sizes were: 3.0, 0.3, 1.0, and 2.0 eV. Integration times ranged from 3 s to 5 s. Kapton tape was used to mount all samples and the sample holder was made of quartz, to avoid any metallic contributions, while doing the XAFS characterization measurements.

4.2 Growth of Iron Silicon Germanide Thin Films by MBE

The $Fe(Si_{1-x}Ge_x)_2$ samples were grown on double sided polished Si (100) ±0.25° substrates. Both *n*- and *p*-type Si substrates were used. The Si substrate was heated to the desired temperature according to the growth recipe by a substrate heater which is a filament made out of graphite and has a shape of a disk. The intensity of electric current that operates the substrate heater is optimized using a controlled power supply. In order to control the temperature of the Si substrate (T_{sub}) during growth, a temperature calibration is needed, since

the sample thickness changes due to thermal expansion. The substrate temperature calibration is achieved by an infrared (IR) diode laser, which reflects off the front and back surfaces of the Si substrate. Due to interference, these collected reflections form intensity oscillations. The data from the heater can be fit to linear curve. These data points are used to control the T_{sub} during growth.

Before entering the Si substrate into the load-lock of the MBE system, the Si substrates were cleaned by the Shiraki method.[83] The Si substrate is then loaded into the MBE system UHV growth chamber. At first, the Si substrate is heated to a temperature of 800 °C for approximately 45 minutes to remove the oxide layer. The growth recipe of the $Fe(Si_{1-x}Ge_x)_2$ samples starts at this point. While T_{sub} is at 500 °C, Si is e-beamed onto the Si substrate at a rate (r) of 1 Å/s to form a Si buffer layer of 50 nanometers in thickness. On top of the Si buffer layer, a $FeSi_2$ template layer is grown. It will be argued in the results and discussion section of this chapter that the structure of this template layer as well as the overall $Fe(Si_{1-x}Ge_x)_2$ thin film is actually the semiconducting beta (β)-phase of $FeSi_2$ (i.e. β-$FeSi_2$). The growth of the template layer is done by co-e-beaming Fe and Si at the desired stoichiometric ratio of (1:2), while T_{sub} is at 600 °C, to form a thin β-$FeSi_2$ layer composed of only several monolayers. A subsequent 5 minute anneal of this layer at 750 °C is done to achieve the desired $FeSi_2$ (β-$FeSi_2$) template layer. On top of the template layer, a 50 nanometer buffer layer of $FeSi_2$ (β-$FeSi_2$) is grown by stoichiometric co-e-beaming of Fe and Si at the stoichiometric ratio, while T_{sub} ranges between 600 and 700 °C and r is at 1.2 Å/s. After this buffer layer is grown, Ge is introduced to the Fe and Si combination in order to epitaxially grow $Fe(Si_{1-x}Ge_x)_2$. Before Ge is introduced, the Ge effusion cell was kept at a temperature ranging from 1385 to 1405°C. Before opening the Ge

shutter its flux is set to the desired stoichiometric ratio of (Fe:Si:Ge :: 1:2−2*x*:2*x*). While T_{sub} and *r* are at the same 600-700 °C and 1.2 Å/s respectively, the co-deposition of Fe, Si, and Ge is held at the above mentioned stoichiometric ratio until the growth of $Fe(Si_{1-x}Ge_x)_2$ thin films is achieved. The thicknesses of these thin films ranged between 2205 and 7791 Å.

4.3 Results and Discussion

XAFS of $Fe(Si_{1-x}Ge_x)_2$ thin film samples[84-87]

Figure 4.3 and Figure 4.4 show the EXAFS plot of the series of $Fe(Si_{1-x}Ge_x)_2$ thin film samples, with different thicknesses between *T=2205and 7791 Å*). Figure 4.3 doesn't include the XAFS of Fe reference to better illustrate the similarities and differences between the XAFS of the $Fe(Si_{1-x}Ge_x)_2$ thin film samples. Figure 4.4 includes the EXAFS of the Fe reference. As Figure 4.3 shows, the oscillations are almost the same among all the $Fe(Si_{1-x}Ge_x)_2$ thin film samples which means that they are all in the same phase.

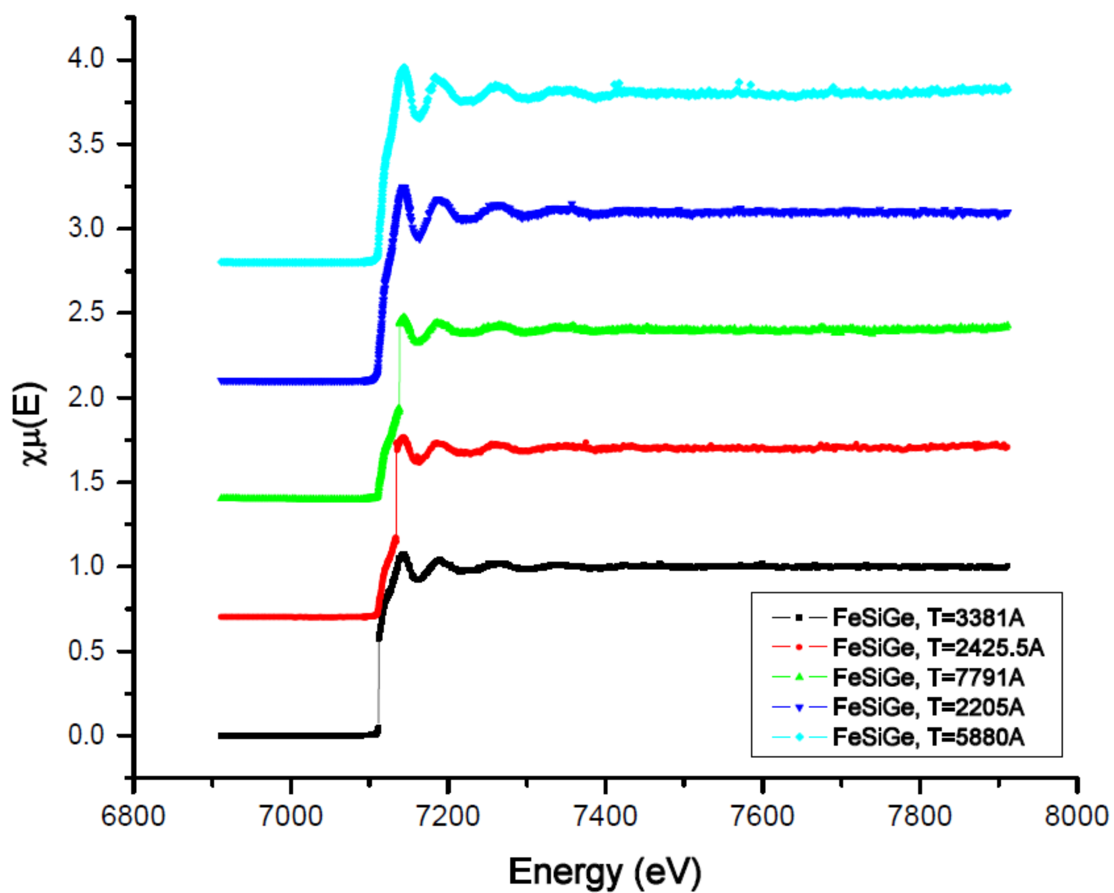

Figure 4.3 XAFS of $Fe(Si_{1-x}Ge_x)_2$ ($0 \le x \le 0.15$) films with different thicknesses without the XAFS of the pure metallic Fe reference.

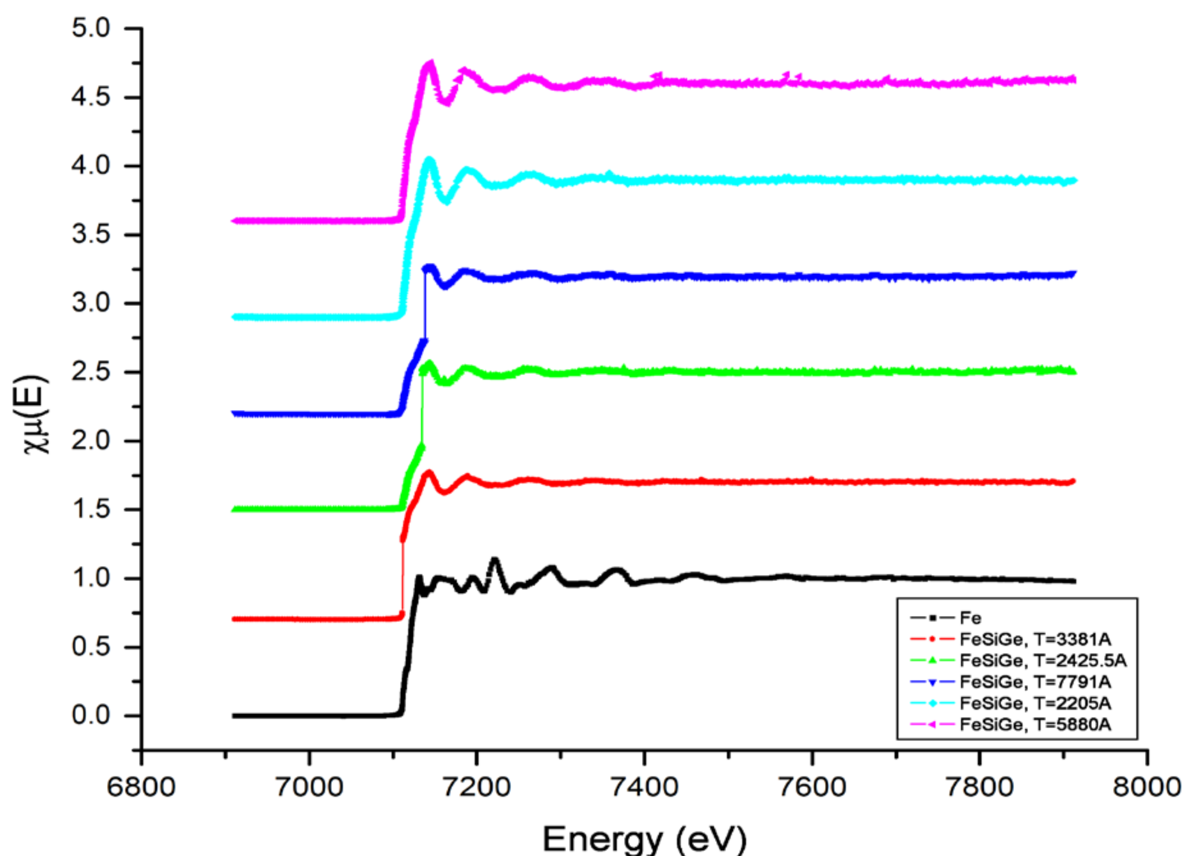

Figure 4.4 XAFS of $Fe(Si_{1-x}Ge_x)_2$ ($0 \le x \le 0.15$) films with different thicknesses in comparison with the XAFS of the pure metallic Fe reference.

However, it is clear that the absorption oscillation intensity and period are different for metallic Fe and $Fe(Si_{1-x}Ge_x)_2$ films together with a shift (up to 17.68 eV in the sample with the highest Ge exposure) from the absorption edge energy (E_0) of Fe, as shown in Figure 4.4. This tells us two important facts about these samples, firstly, there is no agglomerated metallic Fe in the $Fe(Si_{1-x}Ge_x)_2$ thin films, secondly, the samples are not in the metallic phase. Taking the Fourier transform of an EXAFS plot would result in a graph for which the peaks correspond to the number of nearest neighbors to the scattered photoelectron and the radial distances

between them which are called nearest neighbor distances (d_{nn}). As shown in Figure 4.5, the Fourier transforms of the EXAFS plots for the $Fe(Si_{1-x}Ge_x)_2$ thin film samples were taken, so we can get the number of the nearest neighbors & the nearest neighbor distances (d_{nn}), we can clearly observe that the 1st, 2nd, and 3rd d_{nn} are very close in their values with slight variations due to the variation in the Ge content as explained later in this section.

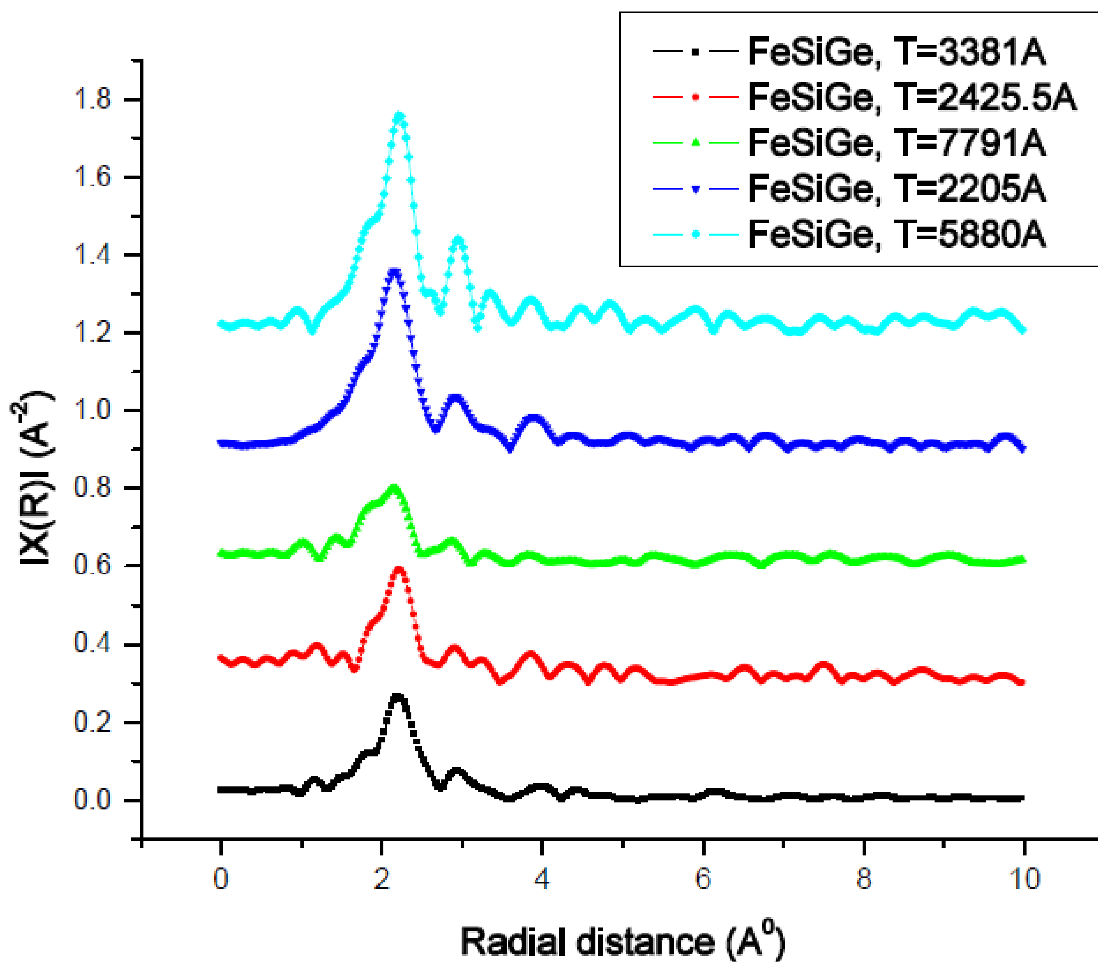

Figure 4.5 The Fourier Transform of the EXAFS of the $Fe(Si_{1-x}Ge_x)_2$ thin films samples without the Fourier Transform of the pure metallic Fe reference.

A confirmation that the $Fe(Si_{1-x}Ge_x)_2$ thin film samples are not in the metallic phase like pure metallic Fe is shown in Figure 4.6. Figure 4.6 clearly illustrates the significant difference of the 1st, 2nd, and 3rd d_{nn} of the $Fe(Si_{1-x}Ge_x)_2$ thin film samples versus those of the pure metallic Fe reference.

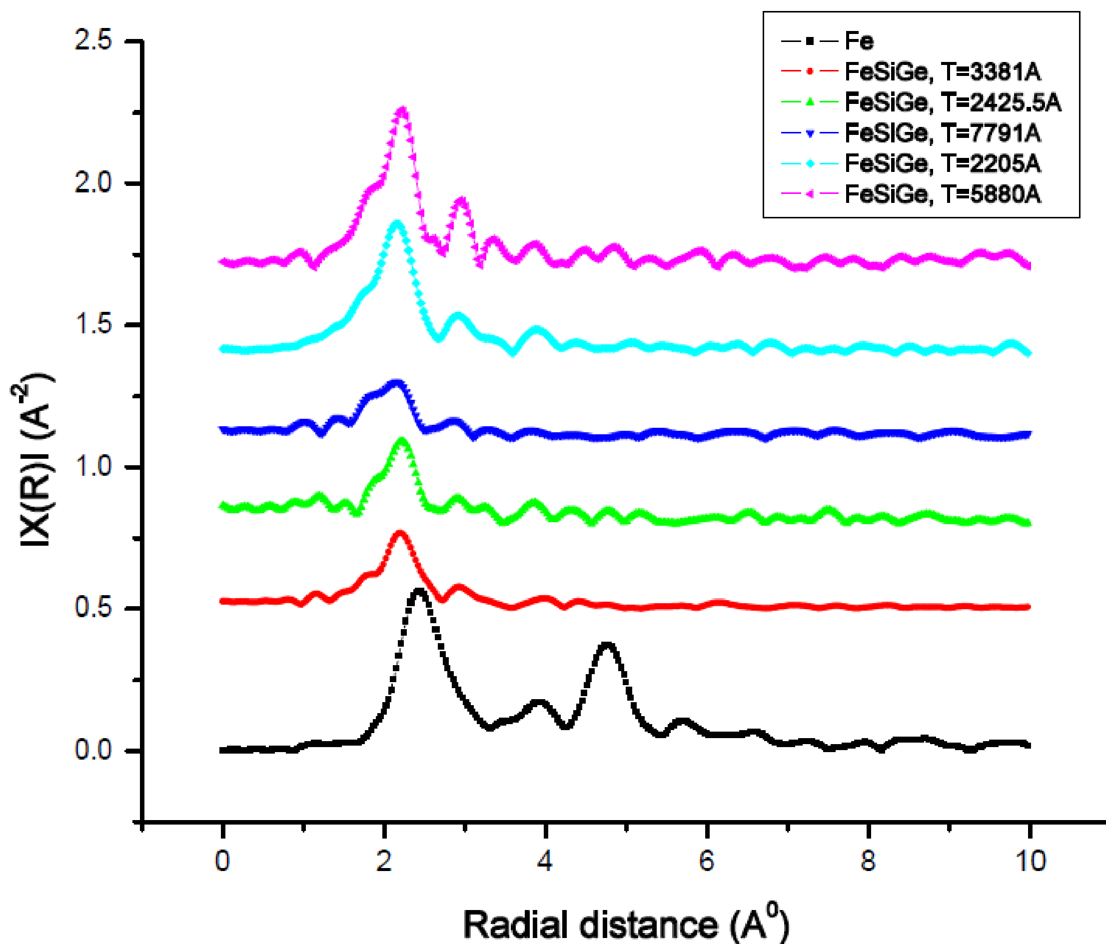

Figure 4.6 The Fourier Transform of the EXAFS of the $Fe(Si_{1-x}Ge_x)_2$ thin films samples with the Fourier Transform of the pure metallic Fe reference.

The d_{nn} values for the series of $Fe(Si_{1-x}Ge_x)_2$ thin film samples are in close agreement with the known standard d_{nn} values for β-phase $FeSi_2$, for example one of the samples in the series has the 1st d_{nn}, 2nd d_{nn} and 3rd d_{nn} as 2.21 Å, 2.94 Å and 4.0 Å respectively which is in very close agreement with the 1st d_{nn}, 2nd d_{nn} and 3rd d_{nn} of the β-phase $FeSi_2$ which are 2.33 Å, 2.96 Å and 4.02 Å respectively. As stated earlier, iron silicide and silicides in general exist in more than one stable phase and stoichiometric ratio, a comparison of the known nearest neighbor distances of the different phases of $FeSi_2$ as well as the known nearest neighbor distances of the various stoichiometries of iron silicide, namely α-$FeSi_2$, β-$FeSi_2$, γ-$FeSi_2$, FeSi, and Fe_2Si, is shown in Table 1.

Phase	1st d_{nn}	2nd d_{nn}	3rd d_{nn}
α-$FeSi_2$	2.38	2.69	2.87
β-$FeSi_2$	2.33	2.96	4.02
γ- $FeSi_2$	1.90	2.70	
FeSi	2.29	2.51	2.78
Fe_2Si	2.36	2.59	2.73
Ours	2.21	2.94	4.0

Table 4.1 Nearest neighbor distances of $FeSi_2$ phases and iron silicide stoichiometries in comparison with our $Fe(Si_{1-x}Ge_x)_2$ nearest neighbor distances in very close agreement with those of β-$FeSi_2$.

It is clear that the nearest neighbor distances of the $Fe(Si_{1-x}Ge_x)_2$ thin film samples are in very close agreement with the nearest neighbor distances of the β-phase $FeSi_2$. It is worth noting here, as stated earlier, that the β-phase $FeSi_2$ is the semiconducting phase which tells us that our $Fe(Si_{1-x}Ge_x)_2$ thin film samples are in the semiconducting phase.

The $Fe(Si_{1-x}Ge_x)_2$ thin film samples possess a nominal yet different Ge content given the growth conditions of each, the temperature of the Ge effusion cell during Ge deposition, and the time of Ge deposition. For example, *sample x* with $T=3381\ A^0$, was exposed to Ge deposition for 26 minutes while the Ge effusion cell was maintained at 1400 ^{0}C, *sample y* with $T=2425.5\ A^0$, was exposed to Ge deposition for 30 minutes while the Ge effusion cell was maintained at 1395 ^{0}C, and *sample z* with $T=7791\ A^0$, was exposed to Ge deposition for 60 minutes while the Ge effusion cell was maintained at 1495 ^{0}C. If we take a closer look at the absorption edge energy (E_0) values, and 1st, 2nd, and 3rd nearest neighbor distances values, as extracted from the XAFS data, we observe a slight yet noticeable change in these values with respect to increasing or decreasing Ge content. More explicitly, on one hand we observe that the E_0 increases slightly with more Ge deposits into the sample, while on the other hand we observe a slight decrease in the 1st, 2nd, and 3rd nearest neighbor distances with more Ge deposits into the sample. Table 2 illustrates this observation with explicit numerical values.

EXAFS Results	***Sample x***	***Sample y***	***Sample z***
E_0	7111.78 eV	7115.93 eV	7129.68 eV
$1^{st}\ d_{nn}, 2^{nd}\ d_{nn}, 3^{rd}\ d_{nn}$	2.21, 2.94, 4.0 A^0	2.20, 2.91, 3.86 A^0	2.15, 2.85, 3.83 A^0

Table 4.2 Absorption edge energies (E_0) and nearest neighbor distances (d_{nn}) of *samples x, y, and z,* showing slight increase in the absorption edges of the samples with increasing Ge content. While their nearest neighbor distances slightly decrease with increasing Ge content.

4.4 Conclusions

The x-ray absorption fine structure spectroscopy study of the $Fe(Si_{1-x}Ge_x)_2$, ($0 \le x \le 0.15$) thin films grown by MBE show that the samples are not metallic and are in the β- $Fe(Si_{1-x}Ge_x)_2$ semiconducting phase. A slight yet noticeable increase in the E_0 values and a slight decrease in

the nearest neighbor distances, with increased Ge deposits, were observed.

CHAPTER 5

MOLECULAR BEAM EPITAXIAL GROWTH OF RUTHENIUM SILICIDE AND CHARACTERIZATION

In this chapter, the growth and characterization of ruthenium silicide is presented and discussed. The growth of this semi-conductor material system was done by MBE. The state-of-the-art MBE facility used to grow this silicide is different and more capable than the one mentioned in the previous chapter. The MBE growth technique employed to grow these films was a special one, called the template method. The details of this MBE facility, an explanation of the template method, and an explanation of the various methods used are mentioned in the subsequent sections of this chapter. It is worthwhile mentioning that the Office of Naval Research (ONR) supported the work presented in this chapter, (Contract No. N00014-03-1-0820).

The structural similarities and differences of the as-grown vs. annealed films of diruthenium trisilicide thin films are studied. Hence, the meticulous adherence to the chosen growth conditions of such films – explained in later sections of the chapter - while annealing half of them in order to appropriately study these similarities and differences.

The phase, nature, thickness, and surface topology and morphology of the as-grown and annealed MBE grown films are presented and discussed in their respective sections. The variety of *in situ* and *ex situ* characterization techniques used to study include: (a) Reflection High Energy Electron Diffraction (RHEED), (b) Scanning Tunneling Microscopy (STM), (c) Cross-sectional Scanning Electron Microscopy (X-SEM), (d) Atomic Force Microscopy (AFM), (e) X-ray Photoelectron Spectroscopy (XPS), and (f) Micro Raman Spectroscopy.

5.1 Experimental Methods and Equipment

5.1.1 Molecular Beam Epitaxy (MBE) Facility and *In Situ* Characterization Techniques

The growth of epitaxial ruthenium silicide has been achieved using an enhanced and more capable growth facility than the one used for the growth of the iron silicon germanide discussed in the previous chapter. This state-of-the-art MBE facility is complemented with *in-situ* STM, SPM, XPS and UPS. Figure 5.1 and Figure 5.2 show this state-of-the-art MBE facility. It has three oxide based chambers that are configured to carry out a wide range of materials research into silicides, multifunctional oxides on semiconductors to high-k dielectrics on Si for Complimentary Metal-Oxide Semi-conductor (CMOS) device application, high-k dielectrics on compound semiconductors for high performance III-V Metal-Oxide Semi-conductor Field-Effect Transistor (MOSFET) devices, and the exciting field of multifunctional crystalline oxides for a number of applications utilizing the rich properties of oxides.

In addition to the deposition chambers, there are chambers for x-ray photoelectron and ultra-violet photoelectron spectroscopy, and scanning probe microscopy which allow for the probing of the interfaces and surfaces at any time during hetero-epitaxial layer growth without exposure to the atmosphere. The *in-situ* analysis chamber contains a dual anode x-ray source, an ultraviolet source, an ion gun, a flood gun, low energy electron diffraction as well as an electron gun.

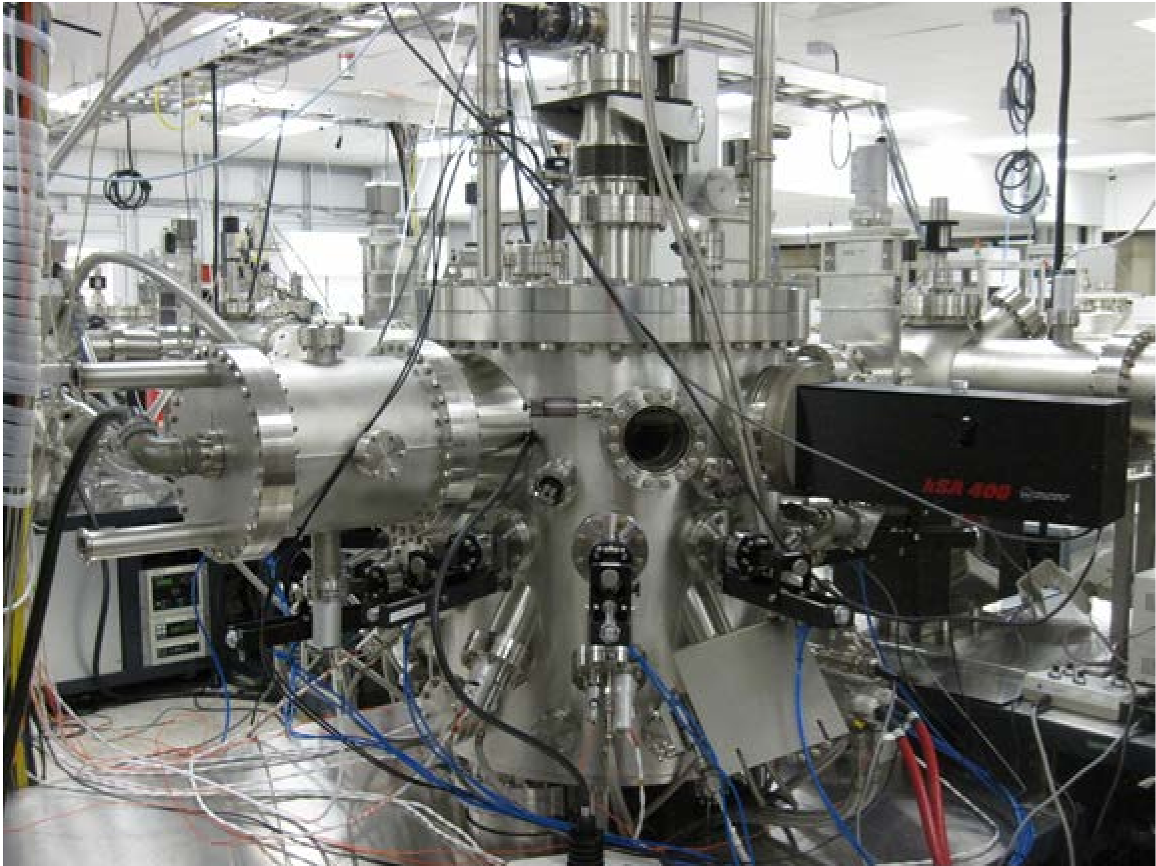

Figure 5.1 The ONR MBE system with Si, Os, and Ru e-beam sources, a Ge effusion cell, and an O plasma source.

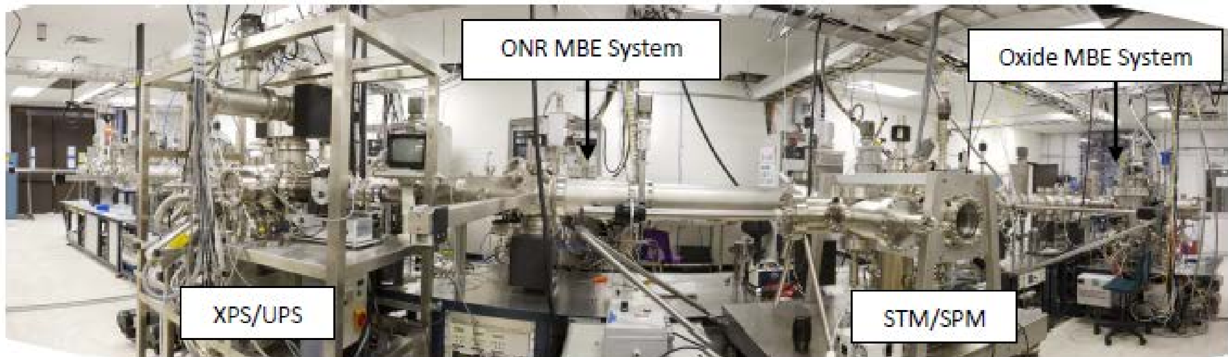

Figure 5.2 The ONR MBE System is shown in relation to the *in situ* XPS/UPS/AES/LEED analysis chamber, STM/SPM/AFM analysis chamber system, and an oxide MBE system.

Additionally, there are a number of connected chambers for the growth of oxides, III-V and II-VI semiconductors, silicon and germanium.

5.1.2 Atomic Force Microscopy (AFM)

The samples were analyzed with Atomic Force Microscopy using a Digital Instruments 5000 model. AFM was in tapping mode, individual scan areas were 2 × 2 µm2 with a 256 ×256 resolution. AFM and cantilever accuracy was confirmed using a NIST traceable standard and a poly-Si control sample. Cu foil was anchored to a scrap Si wafer piece using crystal bond as an adhesive preventing the sample from deforming or moving during analysis.

5.1.3 X-ray Photoelectron Spectroscopy (XPS)

The samples were analyzed using X-ray Photoelectron Spectroscopy (XPS) on a PHI Quantum2000 Scanning ESCA microprobe. 100 micron spot size was used for the analysis with a 500 micron X 500 micron rastered area. Depth of information is from about 30 A^0. Analysis was done using mono-chromated Al Ka lines.

5.1.4 Micro Raman Spectroscopy

Micro Raman Spectroscopy measurements have been performed on the as-grown and annealed diruthenium trisilicide films grown by MBE template method. The measurements were done at 488 nm wavelength.

5.2 Molecular Beam Epitaxial Growth and Characterization of Ruthenium Silicide (Ru_2Si_3) on Si (100)

A series of as-grown and annealed ruthenium silicide (Ru_2Si_3) has been grown by MBE using the template method.[88] The so-called template method is a special and particular two-step process MBE growth technique, in which a very thin layer of the metal is deposited on top of silicon at a low temperature. The choice of this low temperature depends on the temperature at which silicidation occurs for the particular metal-silicon couple. After the thin metal layer is deposited at that low temperature, a subsequent *in situ* annealing takes place at or past the temperature of silicidation in order for a thin silicide layer to form. This thin silicide layer acts as a template for the subsequent growth of the thicker silicide film by the co-deposition of the metal and the silicon at the desired stoichiometric ratio.

3-inch silicon wafers with (100) orientation were used as substrates. Following the oxide removal, cleaning of the 3" Si(100) wafer, and a Si buffer layer growth, a very thin layer of Ru was deposited at a rate of 0.18 A/s for 30 s at 300 ^{0}C. The low substrate temperature prevents instantaneous silicidation which occur around 400 ^{0}C.[28] The substrate temperature was then ramped slowly and held at 400, 500, 600 and 700 ^{0}C. The thin template layer of ruthenium silicide (Ru_2Si_3) is formed by that time. It is important to mention here that the orthorhombic Ru_2Si_3 phase is the only phase that grows in that whole temperature range, see section 1.4.2 for references.

At 700 ^{0}C, Si & Ru were co-evaporated at the desired stoichiometric ratio of 2:3 (Ru:Si::2:3) for 60 min on top of the thin template layer to form the thicker Ru_2Si_3 as-grown film. Some samples were then annealed at 1100 ^{0}C for 300 s. Both of the ruthenium and silicon

are evaporated by electron beaming their respective sources in the MBE chamber. The chamber is under ultra-high vacuum (UHV) at all times during the growth process. All growth rates were calibrated by a quartz crystal monitor (QCM).

5.3 Reflection High Energy Electron Diffraction (RHEED)

RHEED was employed *in situ* to monitor and control the growth process. RHEED of the Ru_2Si_3 template layer after full silicidation at 800 ^{0}C, shown in Figure 5.3, shows a significant difference in the RHEED pattern reconstruction from a typical Si 2x1 – reconstruction RHEED pattern shown in Figure 5.4. RHEED of as-grown Ru_2Si_3 films show a three dimensional crystalline growth pattern with symmetry every 90 degree azimuth as shown in Figure 5.5. The annealed samples appear to regain two dimensional film nature as shown in Figure 5.6.

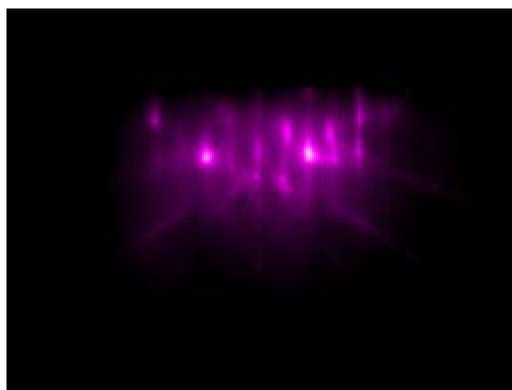

Figure 5.3 RHEED pattern of diruthenium trisilicide template layer at 800 ^{0}C showing a significant difference in the RHEED pattern reconstruction from a typical Si 2x1 – reconstruction shown in Figure 5.4.

Figure 5.4 RHEED pattern of Si after Si buffer layer showing a typical Si 2x1 – reconstruction.

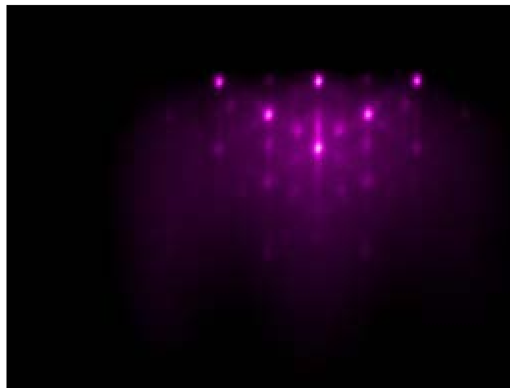

Figure 5.5 RHEED pattern of diruthenium trisilicide as-grown film showing three dimensional crystalline growth pattern with symmetry every 90 degree azimuth.

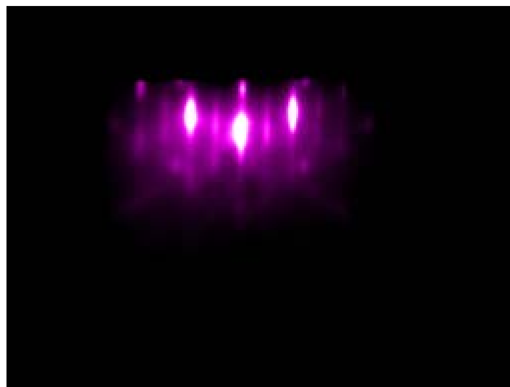

Figure 5.6 RHEED pattern of annealed diruthenium trisilicide film showing that the annealed samples appear to regain two dimensional film nature.

It is worthwhile to mention that the RHEED intensity line profile analysis shows that the lattice constant for Ru_2Si_3 film is twice that of Si. This result is consistent with known lattice constants for Si (5.43095 A^0)[89], and orthorhombic Ru_2Si_3 (11.0 A^0).[8]

5.4 *In Situ* Scanning Tunneling Microscopy (STM)

In situ STM of these diruthenium trisilicide films has been performed on the as-grown and annealed films. The STM image of the as-grown diruthenium trisilicide film, shown in Figure 5.7, shows textured grains of around 0.5 µm in size. The STM image of the annealed film, shown in Figure 5.8, shows a significantly smoother surface with smaller grains.

Figure 5.7 A 2 µm x 2 µm STM image of as-grown diruthenium trisilicide film showing textured grains of around 0.5 µm in size.

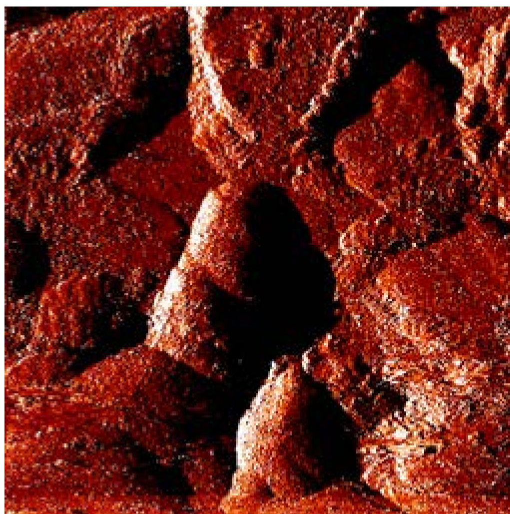

Figure 5.8 A 0.5 µm x 0.5 µm STM image of annealed diruthenium trisilicide film showing a significantly smoother surface with smaller grains in comparison with as-grown film.

5.5 *Ex situ* Cross-sectional Scanning Electron Microscopy (X-SEM)

Ex situ X-SEM measurements of as-grown and annealed diruthenium trisilicide films were done to determine the thicknesses of different sections in the samples. There is a significant obvious difference between the hillock-like surface and structure of the as-grown film and the comparatively smoother surface of the annealed one. The thicknesses of the as-grown range from 25 nm to 125 nm while the annealed thickness is about 40 nm, as shown in Figures 5.9 (a), (b), and 5.9 (c) for the as-grown versus Figures 5.10 (a), (b), and 5.10 (c) for the annealed diruthenium trisilicide.

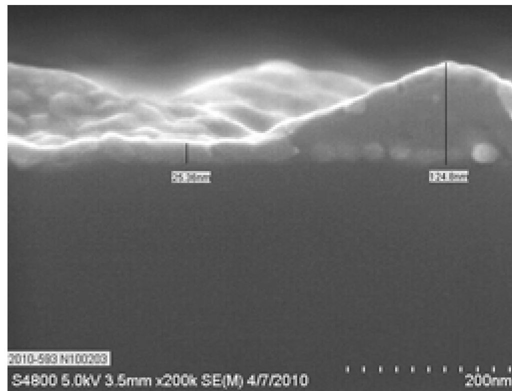

Figure 5.9 (a)

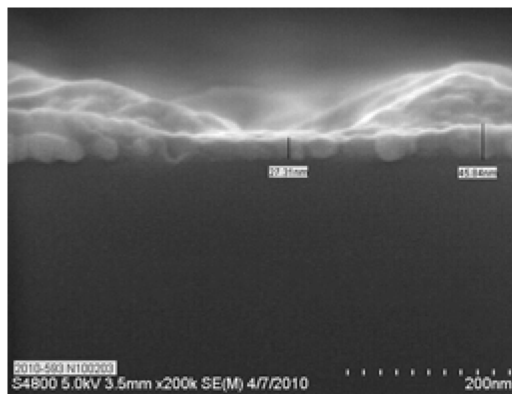

Figure 5.9 (b)

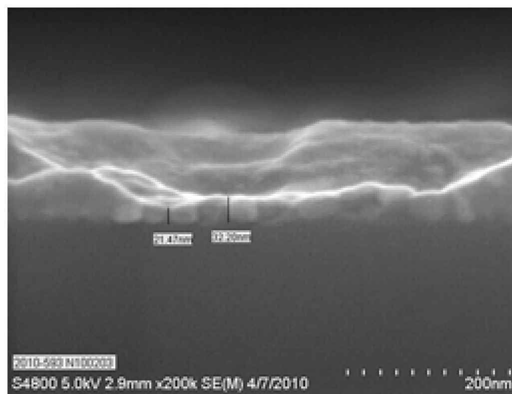

Figure 5.9 (c)

Figure 5.9 X-SEM of as-grown diruthenium trisilicide showing thicknesses ranging from 25 nm to 125 nm showing a hillock-like surface and structure.

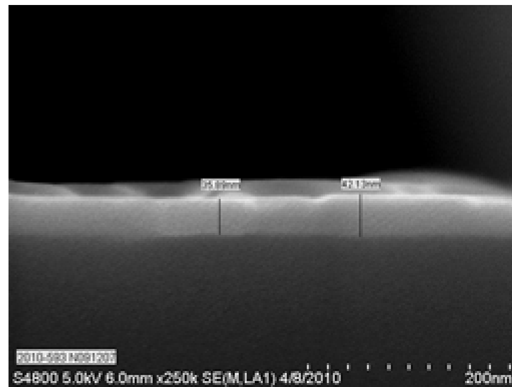

Figure 5.10 (a)

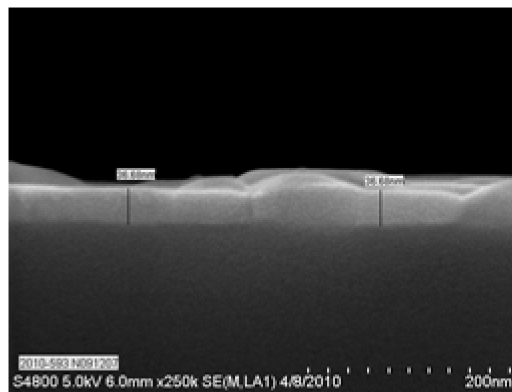

Figure 5.10 (b)

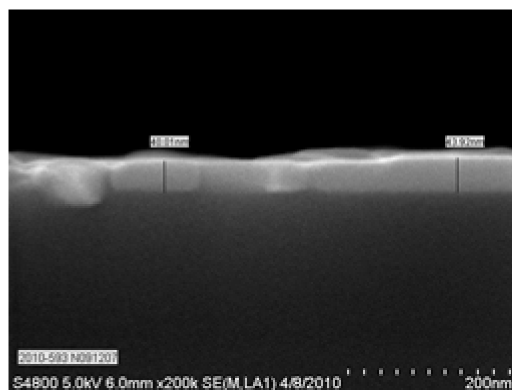

Figure 5.10 (c)

Figure 5.10 X-SEM of annealed diruthenium trisilicide showing thicknesses around 40 nm showing a comparatively smoother surface than the as-grown films.

5.6 *Ex situ* Atomic Force Microscopy (AFM)

Ex situ AFM measurements were done to determine in more detail the size of the hillock-like surface and structure of the as-grown and the size and shape of the grains in the annealed diruthenium trisilicide films.

Figure 5.11 and Figure 5.12, show the significant difference in the root mean square (RMS) surface roughness between the as-grown and the annealed diruthenium trisilicide films respectively.

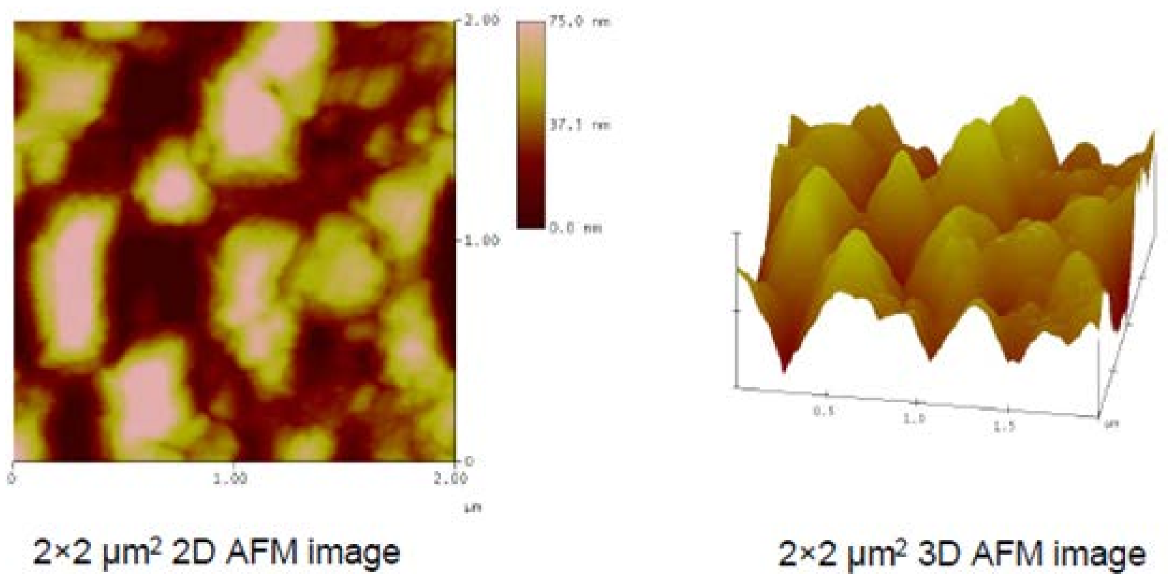

Figure 5.11 AFM of as-grown diruthenium trisilicide films. RMS surface roughness = 22.9 nm

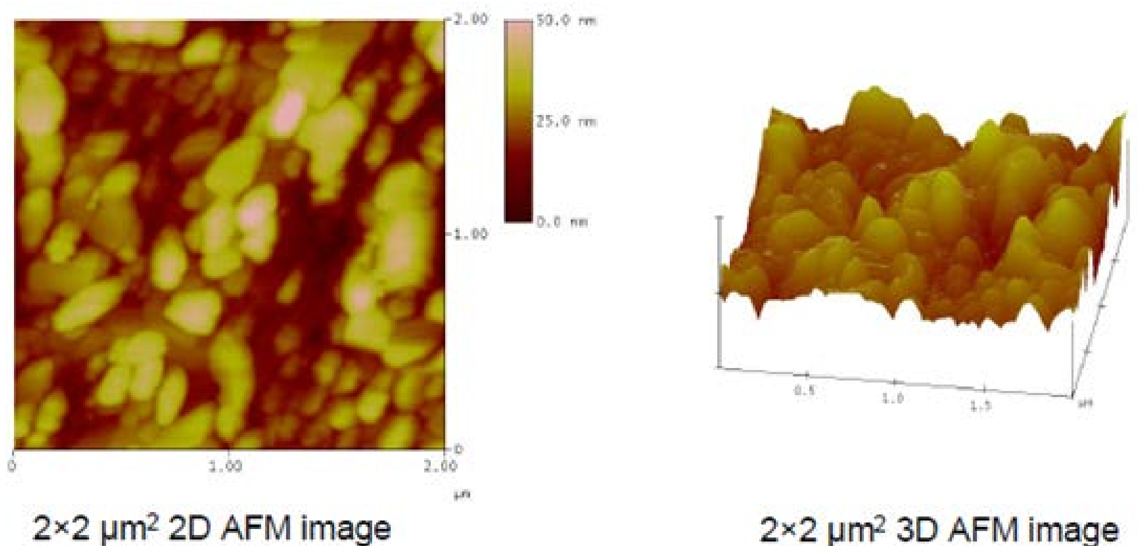

Figure 5.12 AFM of annealed diruthenium trisilicide films. RMS Surface roughness = 8.8 nm

As one can see, the layers clearly exhibit a granular structure. The as-grown film reveal a much more hillock-like structure and bigger grain sizes than the annealed one, with a RMS surface roughness of almost 23 nm. Whereas the annealed film clearly reveal a comparatively much smoother surface with a RMS surface roughness of less than 9 nm, and much smaller grain sizes.

5.7 *Ex situ* X-ray Photoelectron Spectroscopy (XPS)

Ex situ X-ray Photoelectron Spectroscopy (XPS) measurements were performed on the as-grown and annealed diruthenium trisilicide films to verify stoichiometry, and determine the binding energies of the silicide. XPS was performed at the surface as well as after Argon (Ar) sputtering to make sure the films have not been oxidized.

Figure 5.13 (a) and (b) show the stoichiometric ratios and binding energies of the pre-sputtered as-grown diruthenium trisilicide. Figure 5.14 (a) and (b) show the stoichiometric

ratios and binding energies of the post-sputtered as-grown diruthenium trisilicide. Figure 5.15 (a), (b), and 5.15 (c) show the stoichiometric ratios and binding energies of the pre-sputtered annealed diruthenium trisilicide. Figure53.16 (a) and 5.16 (b) show the stoichiometric ratios and binding energies of the post-sputtered annealed diruthenium trisilicide.

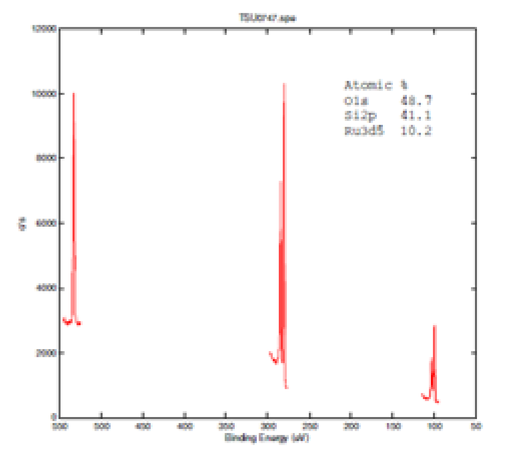

Figure 5.13 (a)

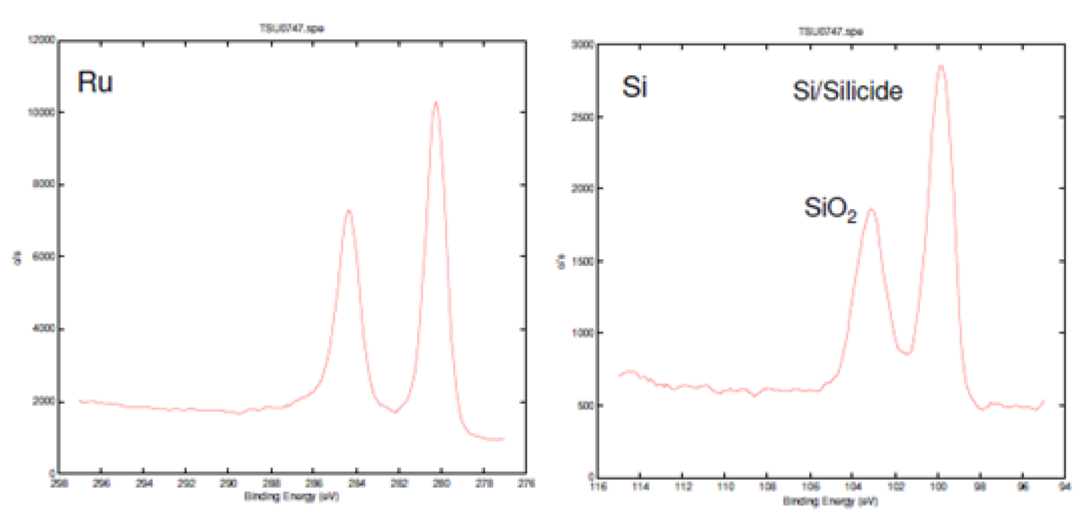

Figure 5.13 (b)

Figure 5.13 Pre-sputtering stoichiometric ratios and binding energies of as-grown diruthenium trisilicide films showing a bit far ratio of ruthenium to silicon from the desired stoichiometric ratio of 2:3. The oxygen presence and silicon dioxide binding energy peak, clearly indicate that very surface of the films have been oxidized due to exposure to air.

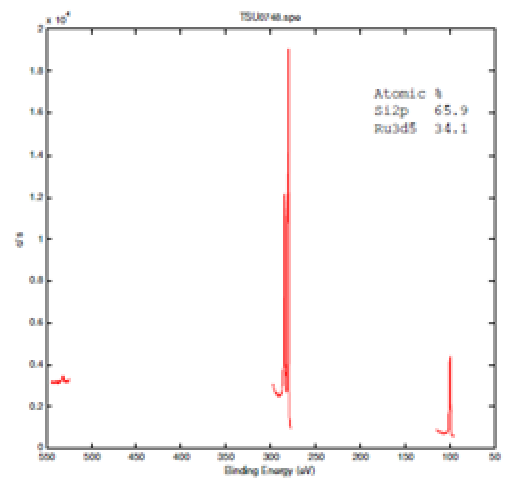

Figure 5.14 (a)

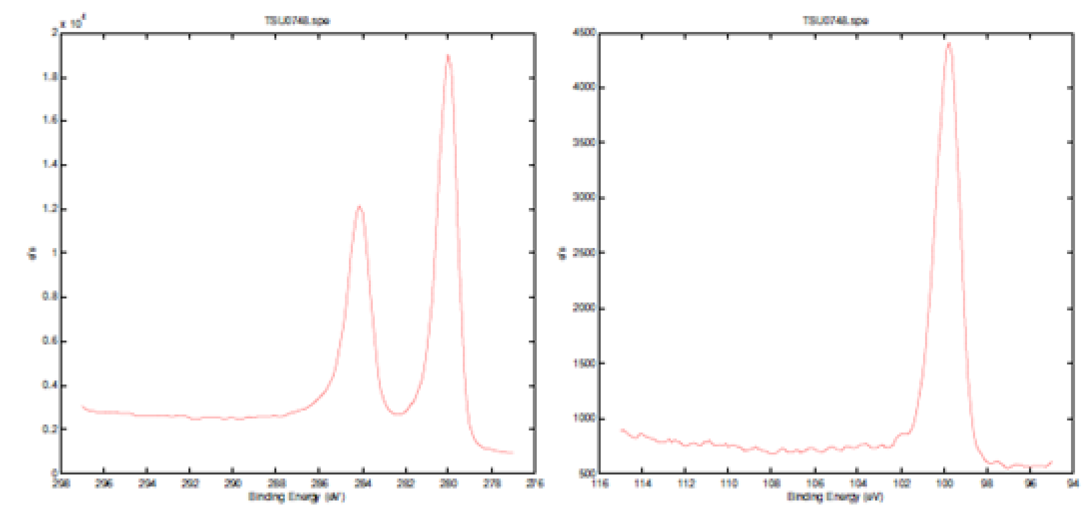

Figure 5.14 (b)

Figure 5.14 Post-sputtering stoichiometric ratios and binding energies of as-grown diruthenium trisilicide films showing the Ru:Si ratio in close agreement with the desired stoichiometric ratio of Ru_2Si_3. Ar-sputtering is only from around 30 A^0 deep.

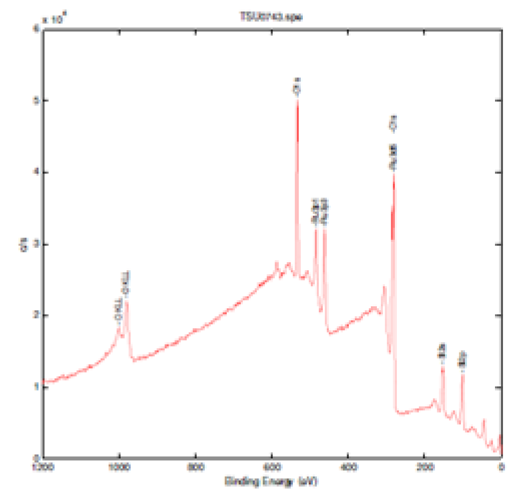

Figure 5.15 (a)

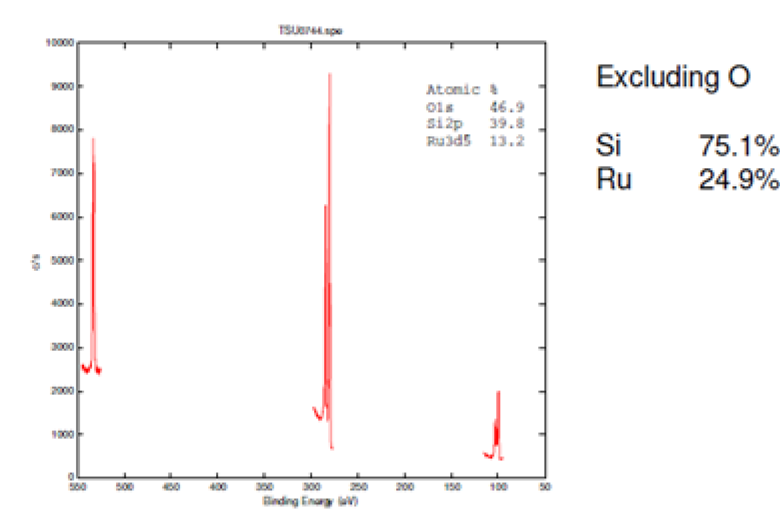

Figure 5.15 (b)

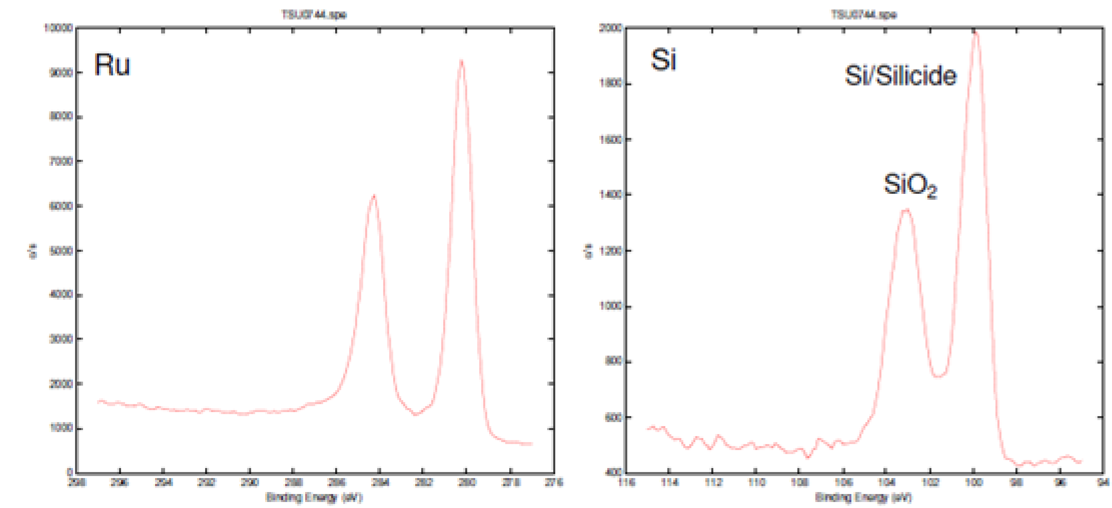

Figure 5.15 (c)

Figure 5.15 Pre-sputtering survey spectrum, stoichiometric ratios and binding energies of annealed diruthenium trisilicide films showing an off Ru:Si ratio in comparison with stoichiometrically desired ratio of 2:3. The oxygen presence and silicon dioxide binding energy peak, clearly indicate that very surface of the films have been oxidized due to exposure to air.

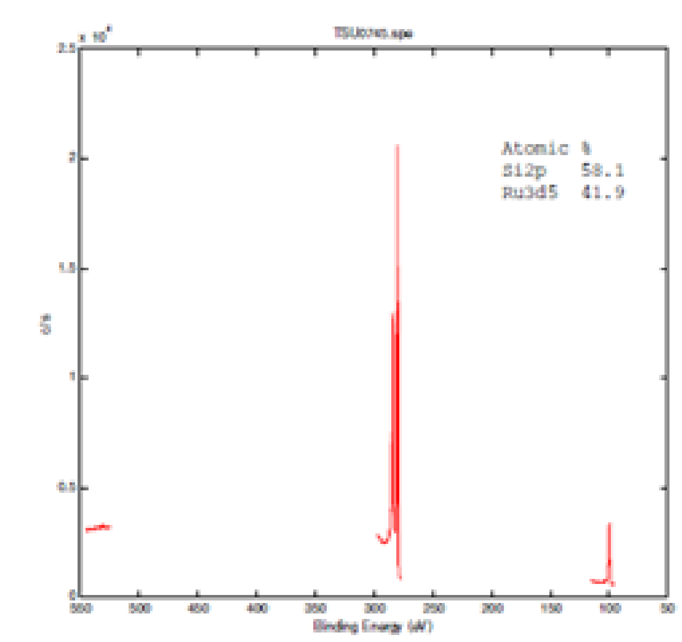

Figure 5.16 (a)

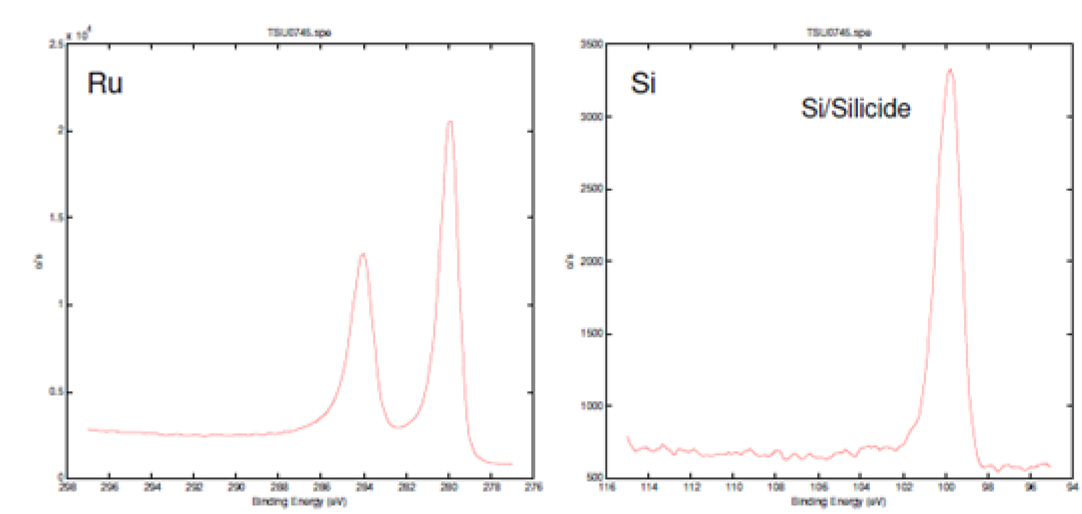

Figure 5.16 (b)

Figure 5.16 Post-sputtering stoichiometric ratios and binding energies of annealed diruthenium trisilicide films showing the Ru:Si ratio in close agreement with the desired stoichiometric ratio of Ru_2Si_3. Ar-sputtering is also from around 30 A^0 deep.

One can see that the ratio of ruthenium to silicon in the pre-sputtered as-grown and annealed films is a bit far from the desired stoichiometric ratio of 2:3 respectively. This, together with the oxygen presence and silicon dioxide binding energy peak, clearly indicate that very surface of the films have been oxidized, which is normal due to the exposure to atmospheric air. The good news is that the ratio of ruthenium to silicon in the post Argon (Ar)-sputtered as-grown and annealed films is in close agreement with the desired stoichiometric ratio of Ru_2Si_3. It is adequate to stress the fact that the Ar-sputtering is only around 30 A^0 deep, which confirms that the oxygen presence and oxidation in the pre-sputtered films is only on the very surface due to exposure to air.

5.8 Micro Raman Spectroscopy

Micro Raman Spectroscopy measurements have been performed on the as-grown and

annealed diruthenium trisilicide films grown by MBE template method. The measurements were done at 488 nm wavelength.

Figure 5.17 shows a comparison of the Raman spectra of the as-grown and the annealed diruthenium trisilicide films with Si as a reference. Signature oscillations and active shifts are observed at shifts less than 500 cm^{-1}. They are expanded for a clearer view in Figure 5.18.

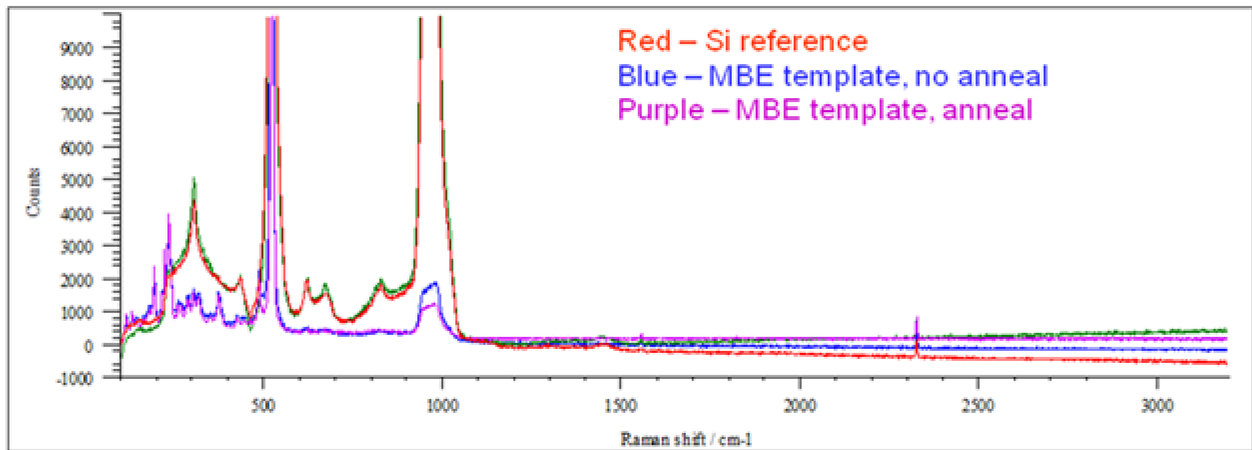

Figure 5.17 Micro Raman Spectroscopy of as-grown and annealed diruthenium trisilicide films showing signature peaks at Raman shifts less than 500 cm^{-1}.

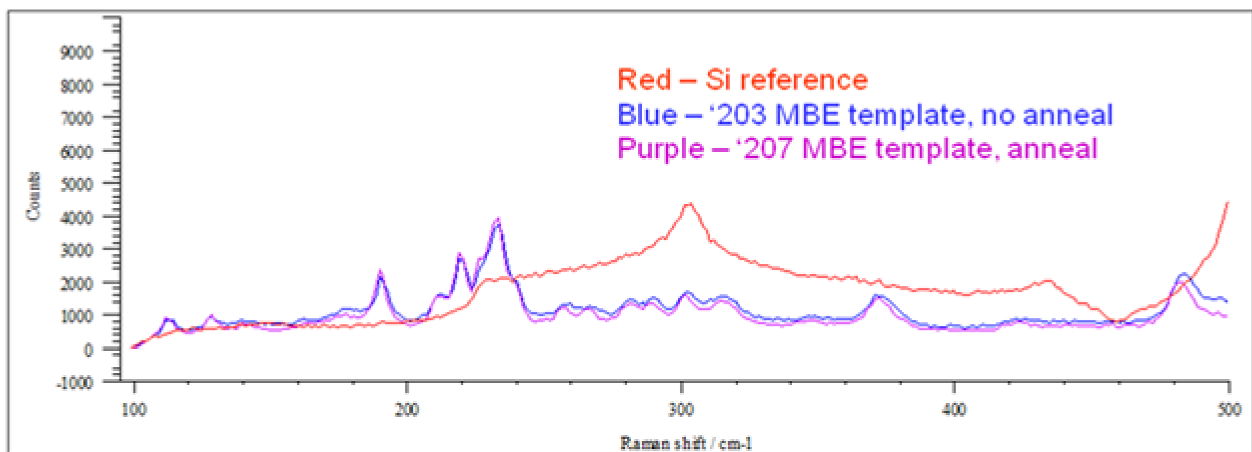

Figure 5.18 A clearer view of the shifts less than 500 cm^{-1} of the Raman Spectroscopy of as-grown and annealed diruthenium trisilicide films showing distinct active Raman shifts from pure Si, at around 190, 220, 235, 370, and 485 cm^{-1}.

One can see that the active Raman shifts in the first 500 cm^{-1} present the signature oscillations and peaks of the diruthenium trisilicide. It is worth noting that there is a clear distinction between the oscillation and their peaks between the diruthenium trisilicide films and the pure Si reference. Also, there is no difference that can be clearly seen between the peaks of the as-grown vs. the annealed films.

CHAPTER 6

MOLECULAR BEAM EPITAXIAL GROWTH OF OSMIUM SILICIDE AND CHARACTERIZATION

In this chapter, the growth and characterization of osmium silicide is presented and discussed. The growth of this semi-conductor material system was done by MBE. The state-of-the-art MBE facility used to grow this silicide is the same as the one used for the growth of the ruthenium silicide films; see section 5.1.1 for the facility's details. It should be noted at this point, that a few efforts were made in the past years to grow the semi-conducting silicides of osmium. This is perhaps due to the highly toxic nature of OsO_4 which is easily formed and sublimates at room temperature. In this work, the MBE growth techniques employed to grow the osmium silicide films were the so-called template method as well as the regular MBE growth method. To our knowledge, this is the first attempt to grow osmium silicide films by MBE employing the special template method. The details of the template method are mentioned in section 5.2. An explanation of the regular MBE growth method and the various methods used to characterize these osmium silicide films are mentioned in the subsequent sections of this chapter. The Office of Naval Research (ONR) supported the work presented in this chapter, (Contract No. N00014-03-1-0820).

The study of the structural similarities and differences of the as-grown vs. annealed films of the osmium silicide thin films grown by the template method and the regular method is discussed. This chapter's study is double-fold in comparison with the previous chapter which was only single-fold, since the study of the similarities and differences are not only with respect to the as-grown vs. the annealed films, but are also with respect to the MBE template growth vs. MBE regular growth. Hence, the meticulous adherence to the chosen growth conditions of

such films – explained in later sections of the chapter - while annealing half of each group, the template growth group and the regular growth group, in order to appropriately study these similarities and differences.

The phase, nature, thickness, and surface topology and morphology of the as-grown and annealed MBE grown films, by both methods, are presented and discussed in their respective sections. The variety of *in situ* and *ex situ* characterization techniques used to study include: (a) Reflection High Energy Electron Diffraction (RHEED), (b) Scanning Tunneling Microscopy (STM), (c) Cross-sectional Scanning Electron Microscopy (X-SEM), (d) Atomic Force Microscopy (AFM), (e) X-ray Photoelectron Spectroscopy (XPS), and (f) Micro Raman Spectroscopy.

6.1 Template and Regular MBE Growth and Characterization of osmium silicide thin films on Si(100)

Osmium silicide films have been grown for the first time, to the best of our knowledge, using the same template MBE technique adopted in Ru_2Si_3 samples detailed in the previous chapter, see section 5.2, except for the temperature at which the template layer is grown. A very thin Os layer is deposited at 200 ^{0}C at a rate of 0.023 A^0/s for 300 s which serves as a template layer of osmium silicide for the film growth at 700 ^{0}C by co-deposition of Si and Os at 0.1 A^0/s and 0.023 A^0/s respectively maintaining a Si/Os flux ratio of around 4 for 60 minutes. Some samples were then annealed *in situ* at 1100 ^{0}C for 70 min, while others are preserved "as-grown" (i.e. without this annealing step).

Osmium silicide films have been also grown by conventional/regular MBE growth technique without using a template layer at 200 ^{0}C, in which the Si buffer layer is deposited at a

550 ^{0}C after Si(100) substrate cleaning, after which immediate film growth at 700 ^{0}C is done by the co-deposition of Si and Os from their respective sources. The co-evaporation of both Si and Os was done by electron beaming their sources. The Si/Os fluxes were maintained at around 4 in an attempt to grow and obtain single phase Os_2Si_3 films according to prior work of our research group and previous findings during phase I of this project.[90]

6.2 Reflection High Energy Electron Diffraction (RHEED)

RHEED was employed *in situ* to monitor and control the growth process. It is evident from RHEED patterns before and after annealing that the osmium silicide samples grown by the template method have better crystalline quality for the as-grown and the annealed than the ones grown by regular MBE growth as shown in Figures 6.1 and 6.2 in comparison with Figures 6.3 and 6.4.

Figure 6.1 RHEED pattern of as-grown osmium silicide grown by the template method showing 3d-growth and great similarity to that of Ru_2Si_3. Chapter 1 mentions that Ru_2Si_3 and Os_2Si_3 are isostructural[2].

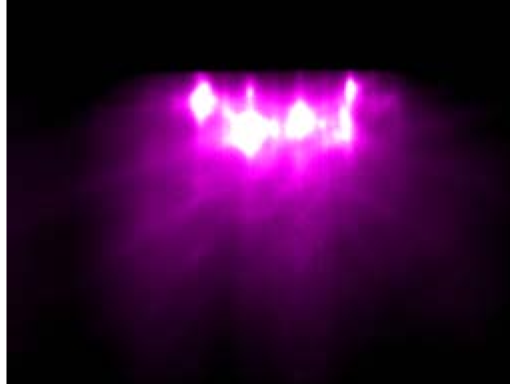

Figure 6.2 RHEED pattern of annealed osmium silicide grown by the template method showing 2d-growth and great similarity with that of annealed Ru_2Si_3 as in the previous chapter. Ru_2Si_3 and Os_2Si_3 are isostructural[2].

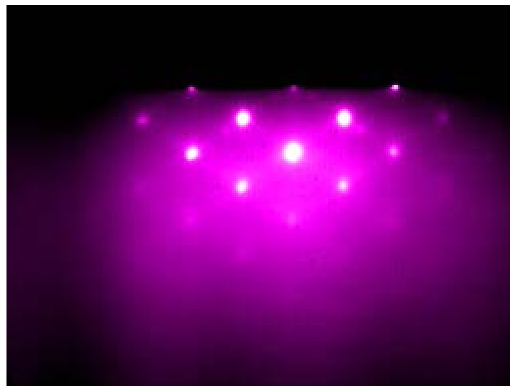

Figure 6.3 RHEED pattern of as-grown osmium silicide by the regular method showing three dimensional growth with distinct difference to typical Si-2x1 RHEED pattern reconstruction.

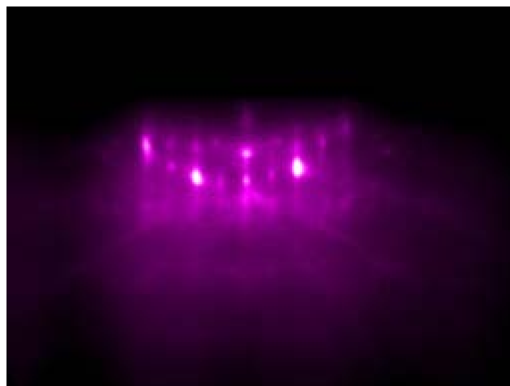

Figure 6.4 RHEED pattern of annealed osmium silicide grown by the regular method showing streaks revealing that the film regained 2d-growth. However, different from the annealed film grown by the template method.

The osmium silicide grown films by the template method show RHEED patterns before and after anneal that are to a greater extent identical to that of Ru_2Si_3 as shown in Figures 5.5 and 5.6 of the previous chapter. It is worthwhile mentioning the fact that the MBE grown Ru_2Si_3 films of the previous chapter are orthorhombic and belong to the *Pbcn* space group, also Os_2Si_3 is orthorhombic and belong to the same space group. One can also see that the RHEED pattern of the as-grown and the annealed grown by both MBE methods is very different from the typical Si 2x1-reconstruction shown in Figure 5.4 in the previous chapter. It is evident that the as-grown films of both MBE methods exhibit three-dimensional growth behavior while the annealed ones seem to regain two-dimensional growth structure, given the streaked RHEED pattern in case of the annealed films vs. the dotty pattern in case of the as-grown.

6.3 *In situ* Scanning Tunneling Microscopy (STM) and *In situ* Atomic Force Microscopy

It is evident from the *in situ* STM and *in situ* AFM before and after annealing that the osmium silicide samples grown by the template method have much more uniformity and crystalline pattern for the textured grains in the as-grown and the annealed, and better crystalline quality in general than the ones grown by regular MBE growth as shown in Figures 6.5 and 6.6 in comparison with Figures 6.7 and 6.8.

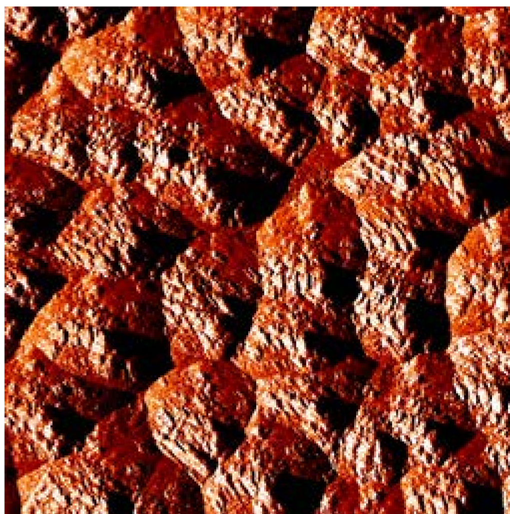

Figure 6.5 A 2 µm x 2 µm *in situ* STM image of as-grown osmium silicide grown by the template method showing hillock-like surface and structure with uniformity for the textured grains.

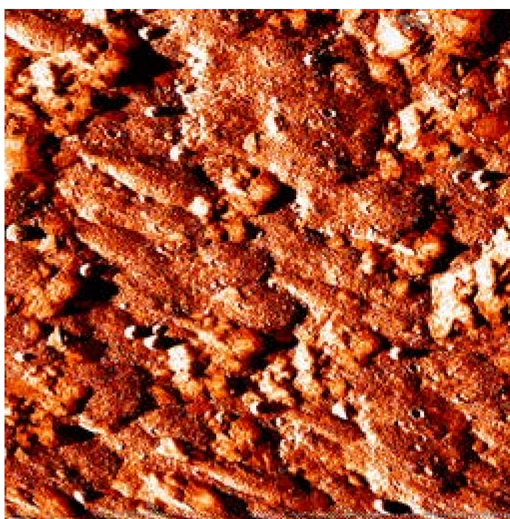

Figure 6.6 A 2 µm x 2 µm *in situ* AFM image of annealed osmium silicide grown by the template method showing an obvious reduction in the size and height of the hillocks together with smaller grain sizes.

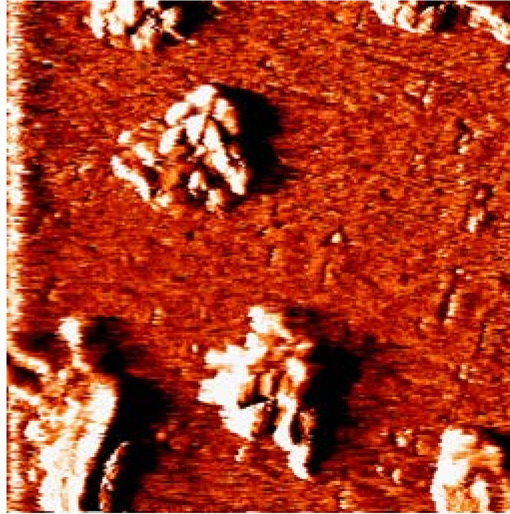

Figure 6.7 A 2 µm x 2 µm *in situ* AFM image of as-grown osmium silicide grown by the regular method showing more of an island-like growth with less uniformity than the as-grown films by the template method.

Figure 6.8 A 2 µm x 2 µm *in situ* AFM image of annealed osmium silicide grown by the regular method showing an overall smoother surface and structure in comparison with the as-grown of the same method. Annealing of films grown by the regular method leads to an overall better quality film.

One can see a clear hillock-like surface and structure with textured grains in the as-

grown films by the template method. This hillock-like structure is sizably bigger, more ordered and uniform than in the as-grown films by the regular method. There is an obvious reduction in the size and height of the hillocks together with smaller grain sizes in the annealed films grown by the template method. Whereas the annealed films grown by the regular MBE method appear to have a much smoother surface and structure in comparison with the as-grown ones by the same method. However, uniformity and crystalline quality are still much more of a signature of the as-grown and annealed films grown by the MBE template method in comparison with the regular MBE method.

6.4 *Ex situ* Cross-sectional Scanning Electron Microscopy (X-SEM)

X-SEM measurements of as-grown and annealed osmium silicide films grown by the template and the regular methods were done to determine the thicknesses of different sections in the samples and observe any interactions of the films with the silicon below. Figures 6.9 (a), (b), (c), (d), and (e) show the cross-sectional SEM of the as-grown osmium silicide films grown by the template method, while Figures 6.10 (a), (b), and (c) show the cross-sectional SEM of as-grown osmium silicide film grown by the regular method. Figures 6.11 (a), (b), and (c) show the cross-sectional SEM of annealed osmium silicide film grown by the template method, while Figures 6.12 (a), (b), and (c) show the cross-sectional SEM of annealed osmium silicide film grown by the regular method.

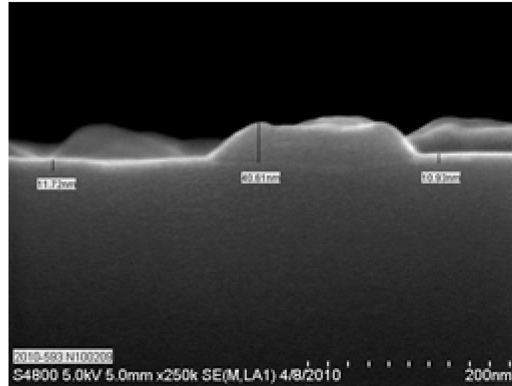

Figure 6.9 (a)

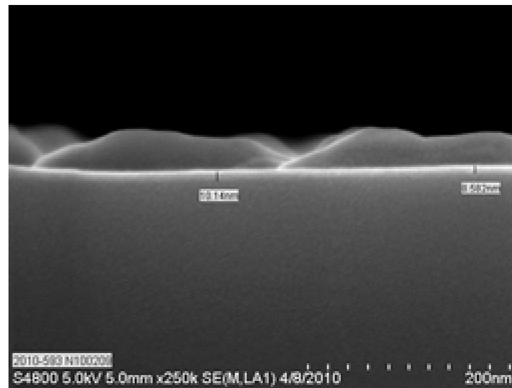

Figure 6.9 (b)

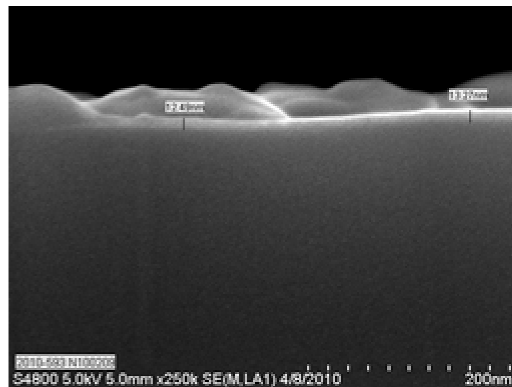

Figure 6.9 (c)

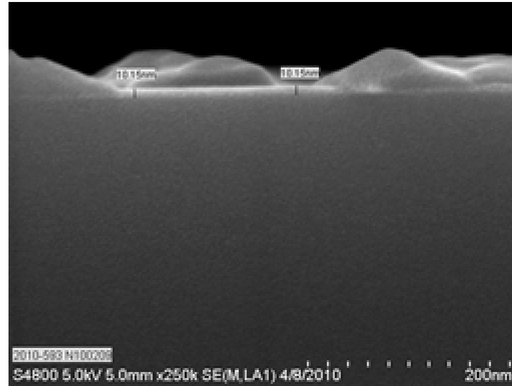

Figure 6.9 (d)

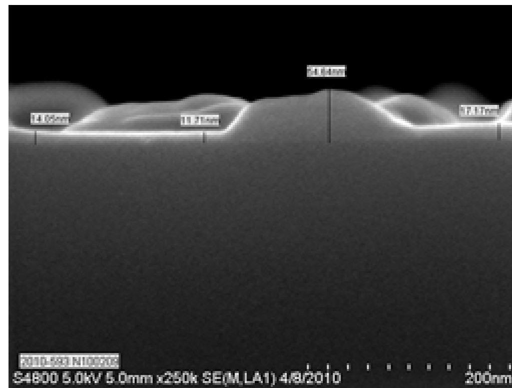

Figure 6.9 (e)

Figure 6.9 (a), (b), (c), (d), and (e) Cross-sectional SEM of as-grown osmium silicide film grown by the template method showing clear hillock-like structure with no interaction between the film and the Si substrate below. Thicknesses of various parts of the film are around 8.5, 10, 17, 13, 41, 55 nm.

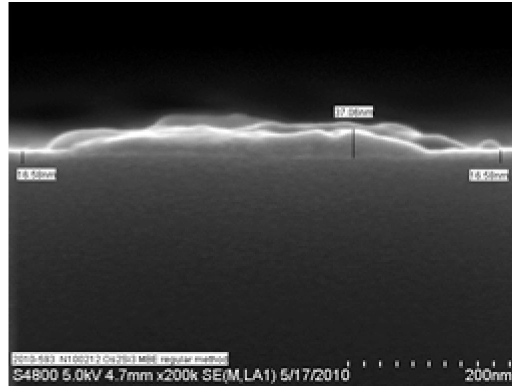

Figure 6.10 (a)

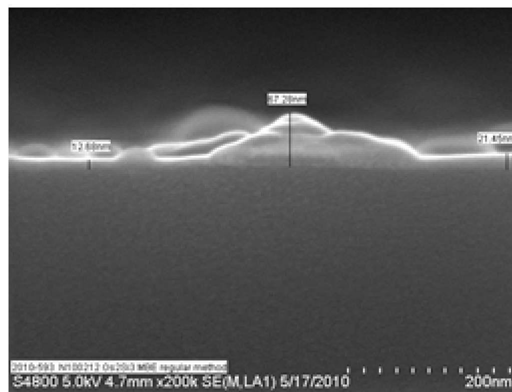

Figure 6.10 (b)

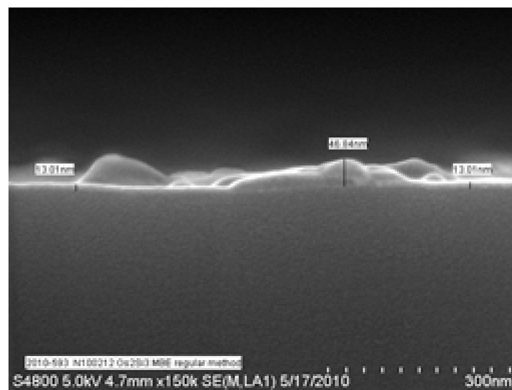

Figure 6.10 (c)

Figure 6.10 (a), (b), and (c) Cross-sectional SEM of as-grown osmium silicide film grown by the regular method showing no interaction of the film with the Si substrate below. Thicknesses of various parts of the film are around 13, 16, 21, 37, 47, and 67 nm.

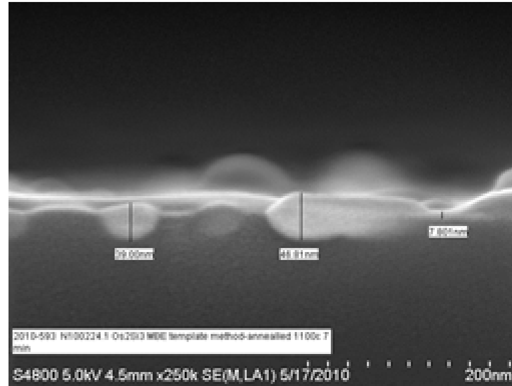

Figure 6.11 (a)

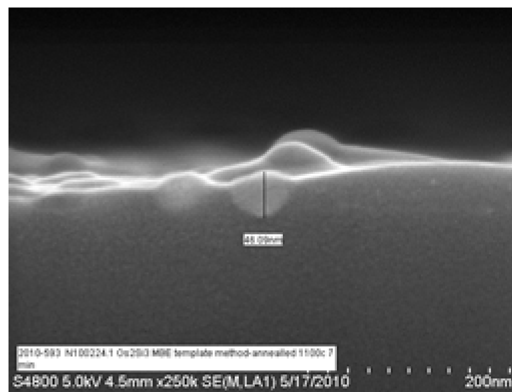

Figure 6.11 (b)

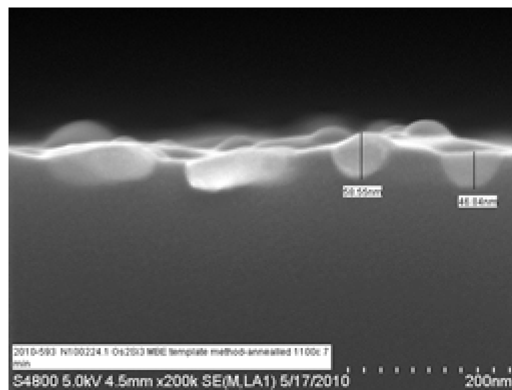

Figure 6.11 (c)

Figure 6.11 (a), (b), and (c) Cross-sectional SEM of annealed osmium silicide film grown by the template method, showing a less hillock height in comparison with the as-grown by the same method. Also, a clear interaction between the film and the Si substrate below is shown. Thicknesses of various parts of the films are around 39, 47, and 58 nm.

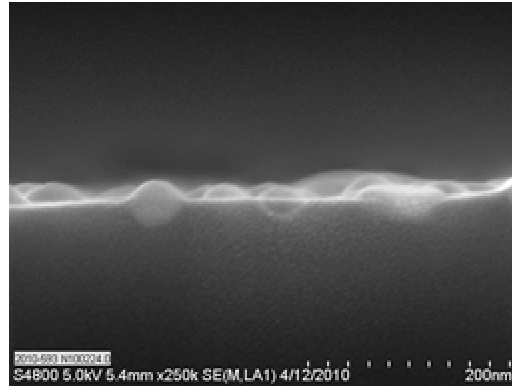

Figure 6.12 (a)

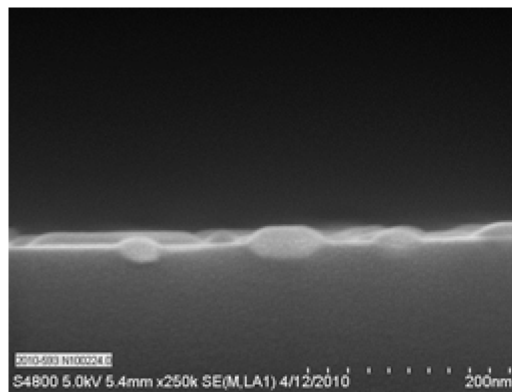

Figure 6.12 (b)

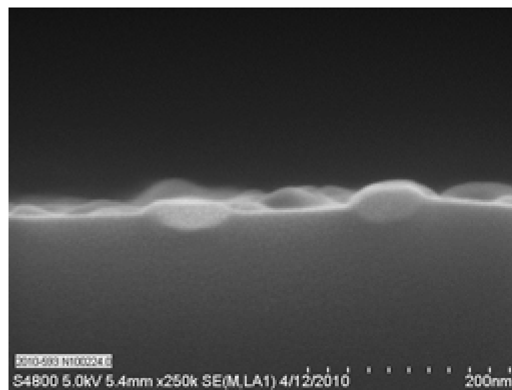

Figure 6.12 (c)

Figure 6.12 (a), (b), and (c) Cross-sectional SEM of annealed osmium silicide film grown by the regular method shows comparatively smoother (lesser thickness) than annealed films grown by the template method. Also, a clear interaction between the film and the Si substrate is evident in annealed films grown by the template and the regular methods.

There is a significant obvious difference between the hillocks of the as-grown film and the smooth surface of the annealed one, grown by both methods. Also, there is a clear interaction between the formed silicide by both MBE methods and the silicon below for the annealed films. The thicknesses of the as-grown range from 9 nm to 67 nm while the annealed thickness is about 46 nm, as shown in Figures 6.9 and 6.10 for the as-grown by the template and the regular method respectively versus Figures 6.11 and 6.12 for the annealed osmium silicide grown by the template and the regular method respectively.

6.5 *Ex situ* Atomic Force Microscopy (AFM)

Ex situ AFM measurements were done to determine in more detail the size of the hillocks of the as-grown and the size and shape of the grains in the annealed osmium silicide films MBE grown by the template and the regular method. The surface roughness was also measured in terms of its root mean square (RMS). The samples were analyzed with Atomic Force Microscopy using a Digital Instruments 5000 model. AFM was in tapping mode, individual scan areas were $2 \times 2\ \mu m^2$ with a 256×256 resolution. AFM and cantilever accuracy was confirmed using a NIST traceable standard and a poly-Si control sample. Cu foil was anchored to a scrap Si wafer piece using crystal bond as an adhesive preventing the sample from deforming or moving during analysis.

Figures 6.13 and 6.14 show two-dimensional and three-dimensional AFM images of as-grown and annealed osmium silicide films respectively, grown by the MBE template method. They also show the root mean square (RMS) surface roughness of each. Figures 6.15 and 6.16 show two-dimensional and three-dimensional AFM images of as-grown and annealed osmium

silicide films respectively, grown by the MBE regular method. They also show the RMS surface roughness of each.

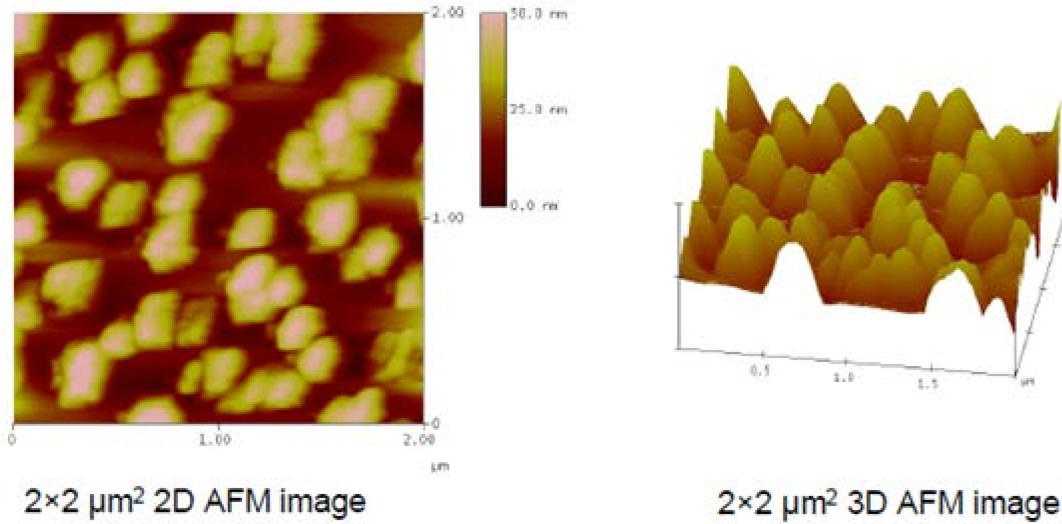

Figure 6.13 AFM of as-grown osmium silicide film grown by the template method. RMS surface roughness = 11.8 nm.

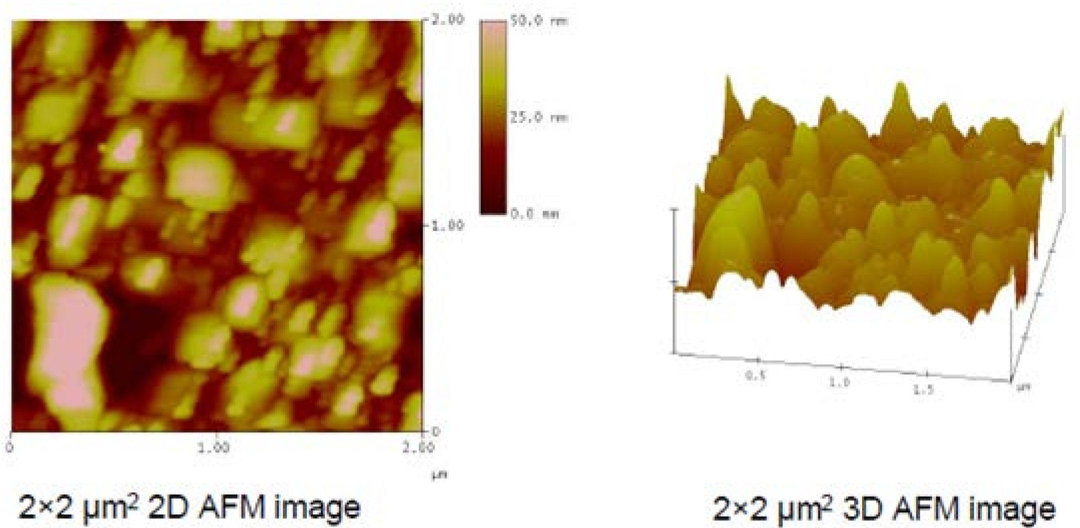

Figure 6.14 AFM of annealed osmium silicide film grown by the template method. RMS surface roughness = 11.4 nm.

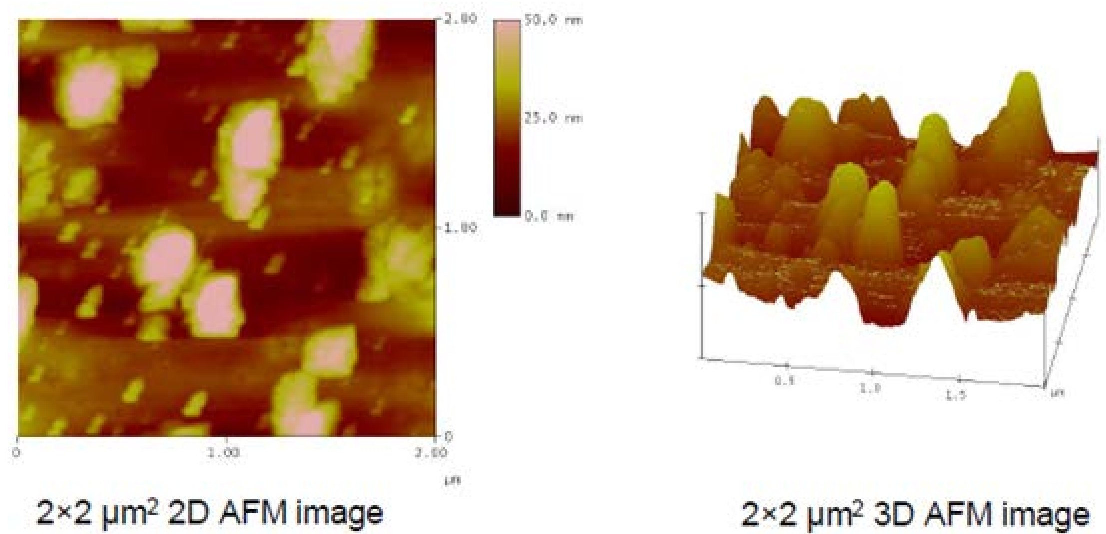

Figure 6.15 AFM of as-grown osmium silicide film grown by the regular method. RMS surface roughness = 10.5 nm

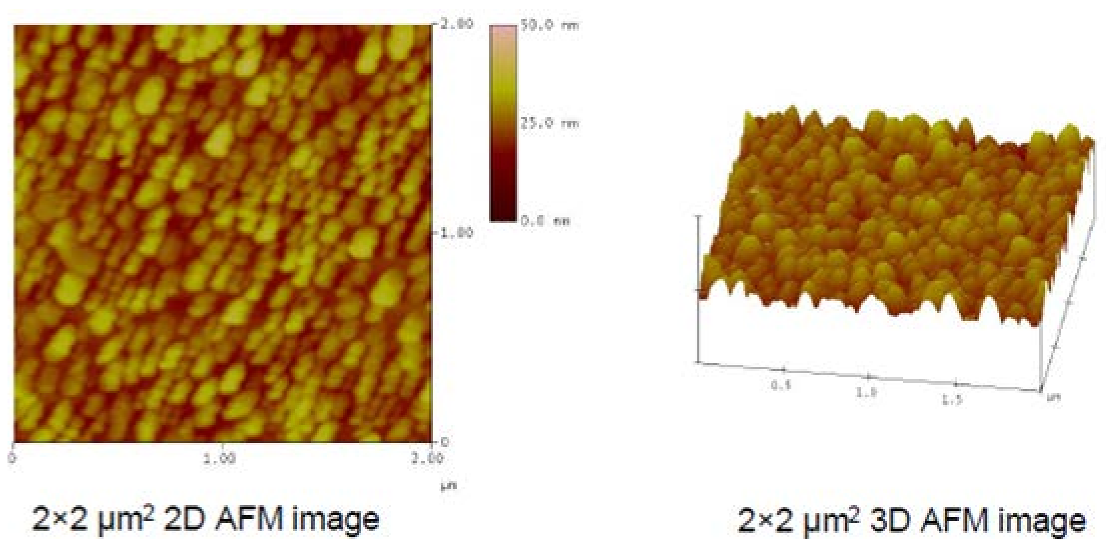

Figure 6.16 AFM of annealed osmium silicide film grown by the regular method. RMS surface roughness = 4.6 nm

One can see that the *ex situ* AFM images reveal less RMS surface roughness for the films grown by the regular MBE method than by the template method. The template method annealed films yield a RMS surface roughness of 11.4 nm, while the regular method annealed

films yield a 4.6 nm RMS surface roughness. The hillock-like surface and structure of the template method as-grown films still show more order and uniformity yet with bigger grains size and height than the regular method as-grown ones. However, it is clear that there is more order and uniformity, and a much smoother surface in the annealed films of the regular method.

6.6 *Ex situ* X-ray Photoelectron Spectroscopy (XPS)

Ex situ XPS measurements were performed on the as-grown and annealed osmium silicide films MBE grown by the template and the regular method to verify stoichiometry, and determine the binding energies of the silicide. XPS was performed at the surface as well as after Argon (Ar) sputtering to make sure the films have not been oxidized.

The samples were analyzed using X-ray Photoelectron Spectroscopy on a PHI Quantum 2000 Scanning ESCA microprobe. 100 micron spot size was used for the analysis with a 500 micron X 500 micron rastered area. Depth of information is from around 30 A^0. Analysis was done using mono-chromated Al Ka lines.

Figures 6.17 (a) and 6.17 (b) show the stoichiometric ratios and binding energies of pre-sputtered as-grown osmium silicide films by the template method, while Figures 6.18 (a) and 6.18 (b) show the post sputtering stoichiometric ratios and binding energies of as-grown osmium silicide films by the template method. While excluding oxygen from the percentages, Figures 6.19 (a) and 6.19 (b) show the stoichiometric ratios and binding energies of pre-sputtered annealed osmium silicide films grown by the template method. Figure 6.20 (a) and 6.20 (b) show the post sputtering stoichiometric ratios and binding energies of annealed

osmium silicide films by the template method. Also, excluding oxygen from the percentages, Figures 6.21 (a) and 6.21 (b) show the stoichiometric ratios and binding energies of pre-sputtered as-grown osmium silicide films by the regular method, while Figures 6.22 (a) and 6.22 (b) show the post sputtering stoichiometric ratios and binding energies of as-grown osmium silicide films by the regular method.

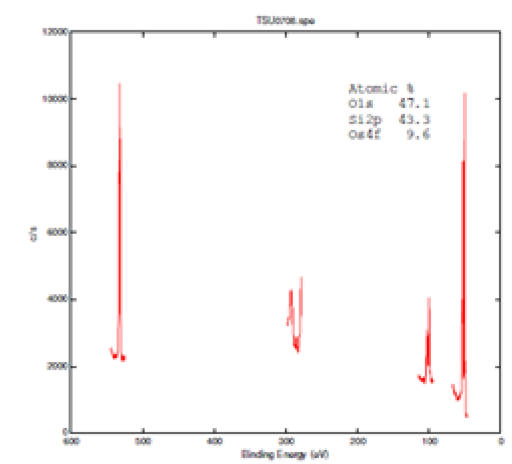

Figure 6.17 (a)

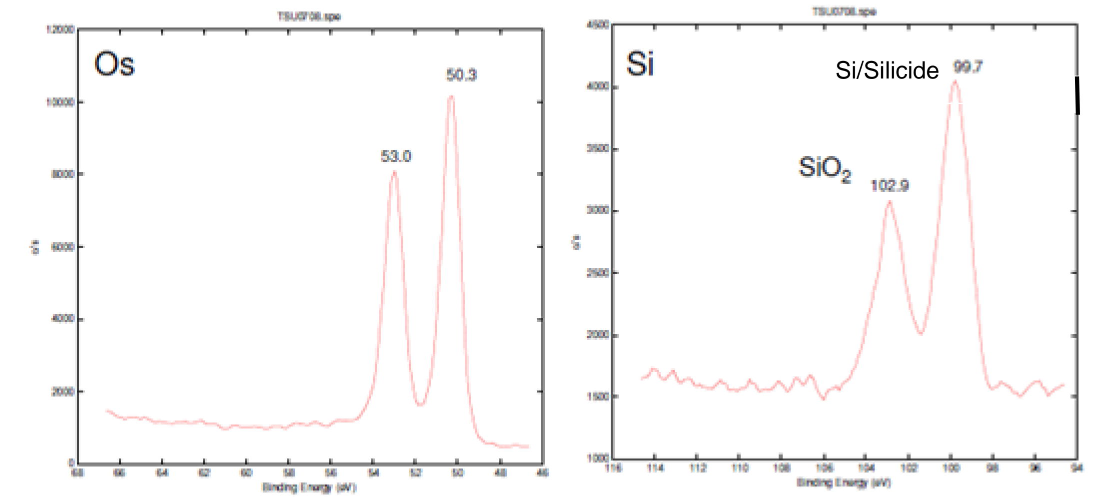

Figure 6.17 (b)

Figure 6.17 (a) and (b) Pre-sputtering stoichiometric ratios and binding energies of as-grown osmium silicide films by the template method showing the oxidation of the surface of the films as confirmed by the SiO_2 binding energy peak. The Os:Si cannot be confirmed here unless the oxygen is removed from the elemental percentages, as it is shown in Figure 6.19 and Figure 6.21.

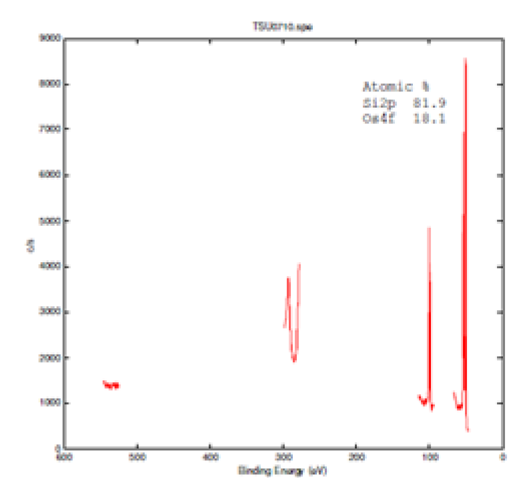

Figure 6.18 (a)

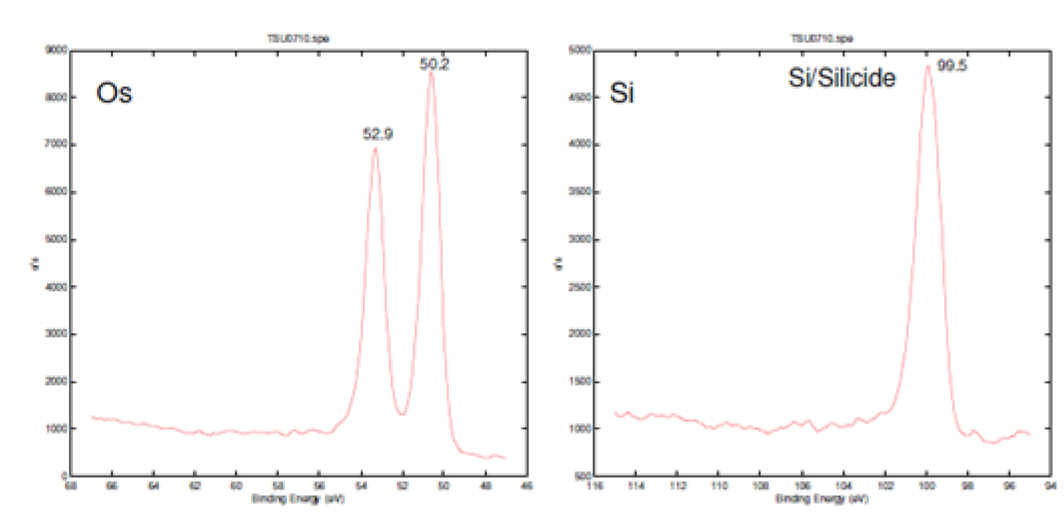

Figure 6.18 (b)

Figure 6.18 (a) and (b) Post sputtering stoichiometric ratios and binding energies of as-grown osmium silicide films by the template method showing no oxygen peak confirming that the surface oxidation in the pre-sputtered films was due to exposure to air. Ar sputtering is only from around 30 A[0] deep into the film. Also, the Os:Si ratios are close to 4, as desired and maintained during growth by the Os and Si flux controls. This Si rich ratio results in the growth of single phase Os_2Si_3[90].

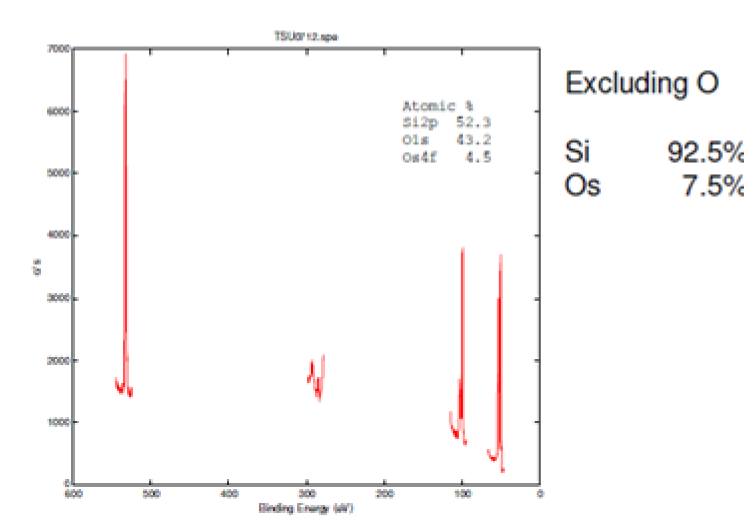

Figure 6.19 (a)

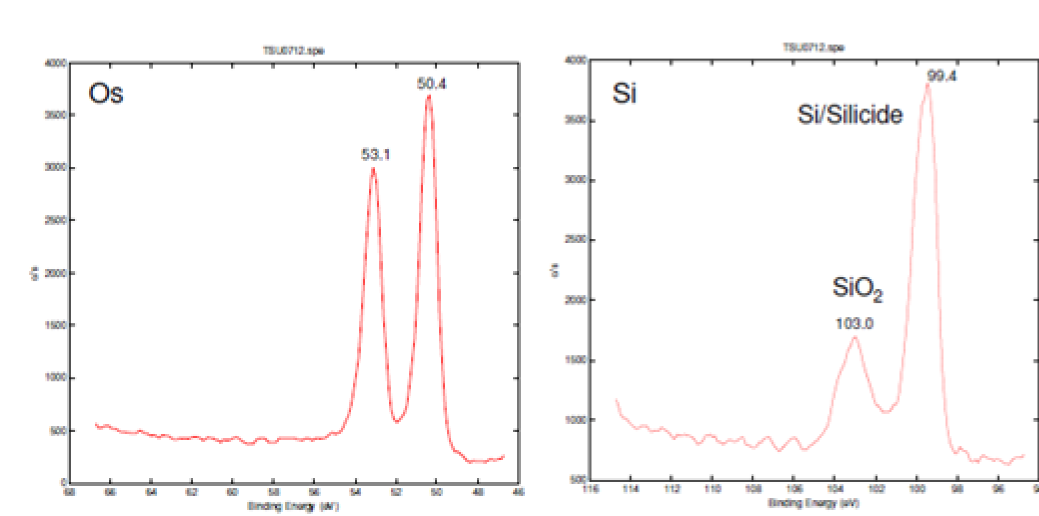

Figure 6.19 (b)

Figure 6.19 (a) and (b) Pre-sputtering stoichiometric ratios and binding energies of annealed osmium silicide films by the template method showing surface oxidation as well as an off Os:Si ratio, with a very much Si rich film, this may be attributed to the interaction of the annealed film with the Si substrate below as evident from the cross-sectional SEM images in section 6.4 of this chapter.

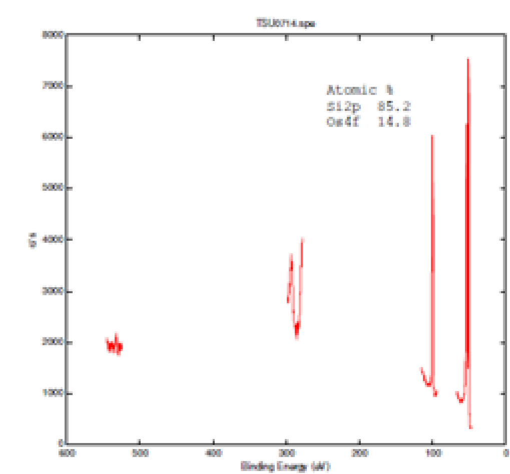

Figure 6.20 (a)

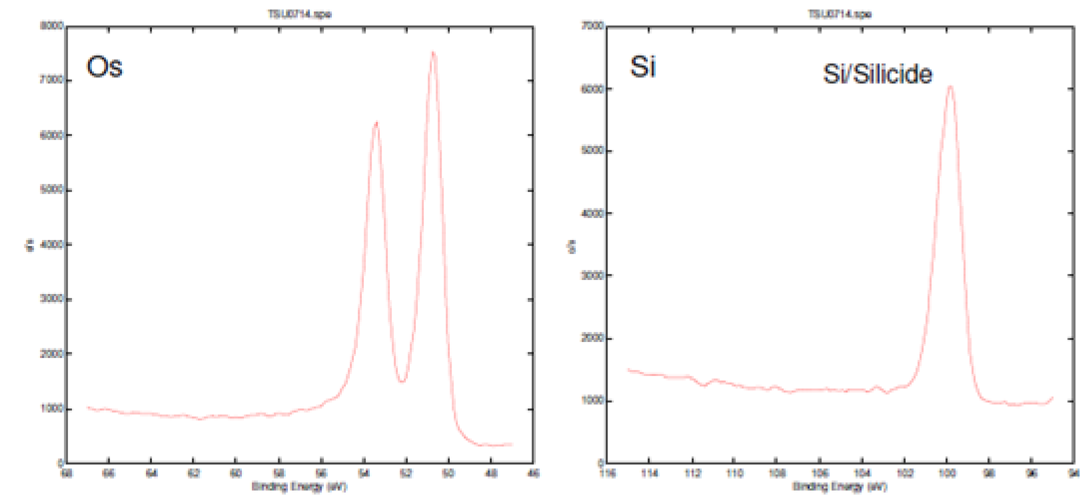

Figure 6.20 (b)

Figure 6.20 (a) and (b) Post sputtering stoichiometric ratios and binding energies of annealed osmium silicide films by the template method showing an off Os:Si ratio that is very much Si rich. This is consistent with the pre-sputtered annealed films grown by the same method shown in Figure 6.19.

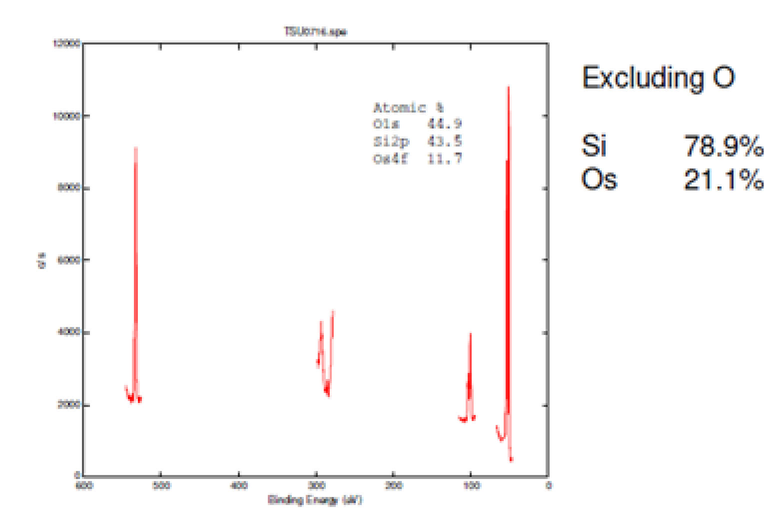

Figure 6.21 (a)

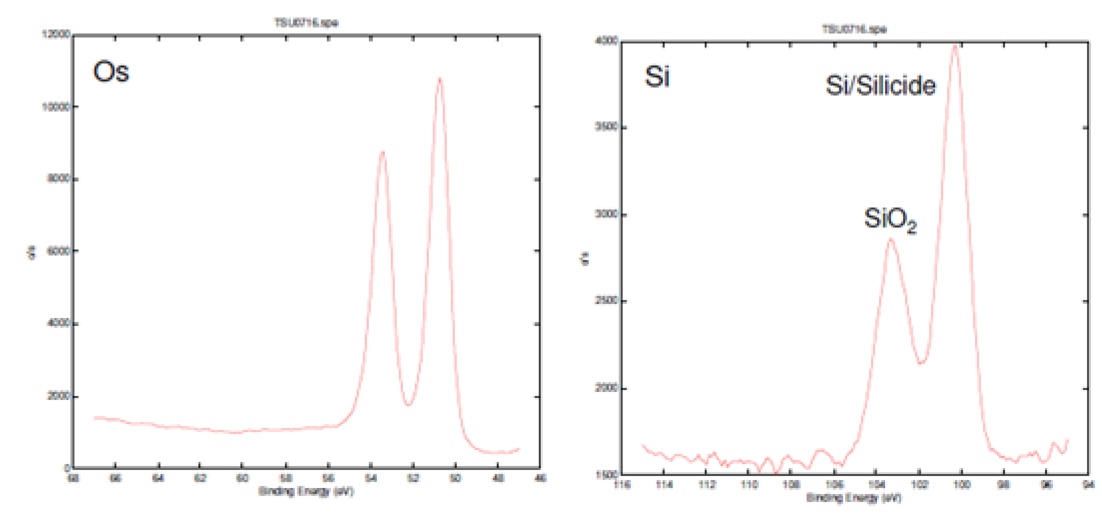

Figure 6.21 (b)

Figure 6.21 (a) and (b) Pre-sputtering stoichiometric ratios and binding energies of as-grown osmium silicide films by the regular method showing oxidation of the surface of the film. However, excluding oxygen, yields the desired Si rich Os:Si ratio of 4 in order to obtain single phase Os_2Si_3[90].

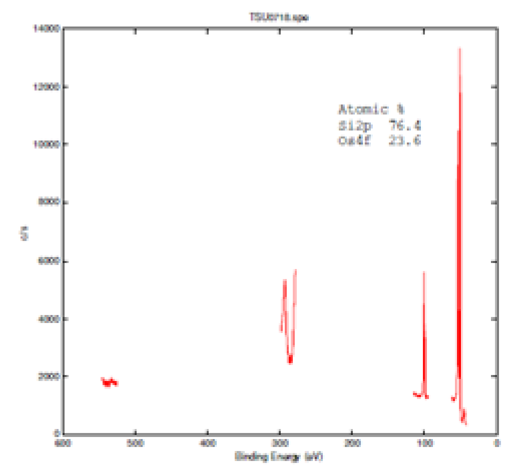

Figure 6.22 (a)

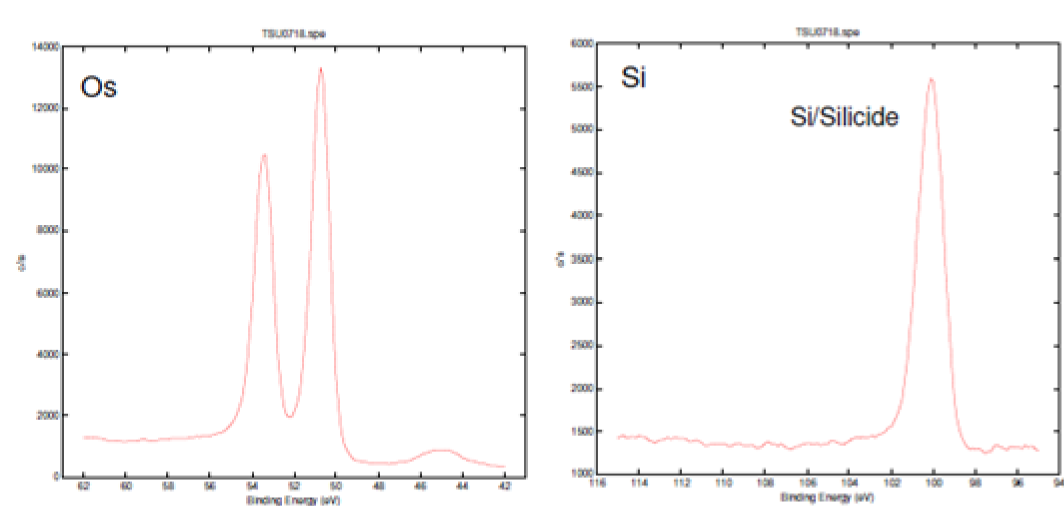

Figure 6.22 (b)

Figure 6.22 (a) and (b) Post sputtering stoichiometric ratios and binding energies of as-grown osmium silicide films by the regular method showing no surface oxidation as well as comparatively close agreement with the desired Si rich Os:Si ratio. This is consistent with the pre-sputtered as-grown films shown in Figure 6.21 if oxygen is removed from the elemental percentage.

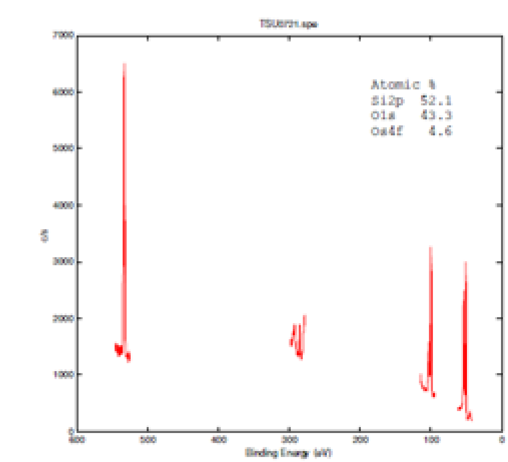

Figure 6.23 Pre-sputtering stoichiometric ratios and binding energies of annealed osmium silicide films by the regular method. Again, pre-sputtered films show surface oxidation and once again, annealed films by both growth methods show a clear off Os:Si ratio which is very Si rich due to the film-substrate interaction during annealing.

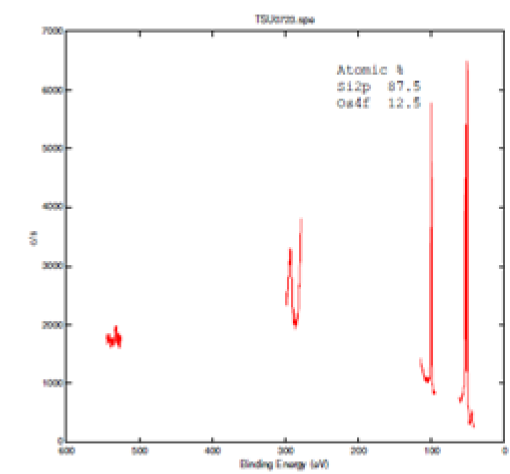

Figure 6.24 Post puttering stoichiometric ratios and binding energies of annealed osmium silicide films by the regular method showing no surface oxidation, yet reveals a consistent off Os:Si ratio of annealed films, which is greatly attributed to the film interaction with the Si substrate during the annealing process.

One can firstly see that oxygen does exist in all pre-sputtered films grown by both MBE methods whether they are as-grown or annealed, as confirmed by the binding energy peak of SiO_2 and the binding energy peak of oxygen in the stoichiometric ratio of elements present. However, neither oxygen nor the oxide binding energy peaks are present in the post-sputtered films grown by both MBE techniques, whether as-grown or annealed. It is very worthy at this point to stress the fact that the depth of Argon (Ar) sputtering is only about 30 A^0. These observations together with this fact clearly tell us that the films have been oxidized at the very surface only due exposure to atmospheric air which is a normal process to occur.

One can also see that the MBE template method and the regular MBE growth method, in which the Si/Os fluxes were maintained at around 4 (section 6.1), yields percentages of osmium and silicon in the as-grown films that are very close to their flux ratios during growth, according to XPS results for both of the pre-sputtered, pre-sputtered (excluding oxygen) and post-sputtered films. This is only seen in the as-grown films. It is important to stress that the

choice of the Si/Os ratio of 4 should result in single phase Os_2Si_3 films.[90] However, in the annealed films, one can clearly see that both MBE methods yield a significant increase in the silicon percentages over the osmium ones, which means that the annealed films are very much silicon-rich. This may be attributed to the interaction of the silicide as-grown film with the silicon underneath as illustrated by the cross-sectional scanning electron microscopy (X-SEM) images of the annealed films, see section 6.3.

6.7 Micro Raman Spectroscopy

Micro Raman Spectroscopy measurements have been performed on the as-grown and annealed osmium silicide films grown by the MBE template and regular method. The measurements were done at 488 nm wavelength.

Figure 6.25 and Figure 6.26 show comparisons of the Raman spectra of the as-grown and the annealed films, with Si as a reference, for both of the growth methods. Signature oscillations are observed at shifts less than 500 cm^{-1} and are expanded for a clearer view in Figures 6.27 and 6.28.

One can see that the regular MBE growth method clearly yields the signature peaks for the as-grown and the annealed films and that the template MBE method clearly yields for the annealed ones only. This means that annealing the osmium silicide as-grown films by the template method enhances the overall film quality of the osmium silicide phase grown. It is worthwhile mentioning that these signature peaks are in the Raman shifts that are 500 cm^{-1} or less. The sharp signature peaks that define the phase grown are at 126, 140, 162, 184 and 196 cm^{-1}.

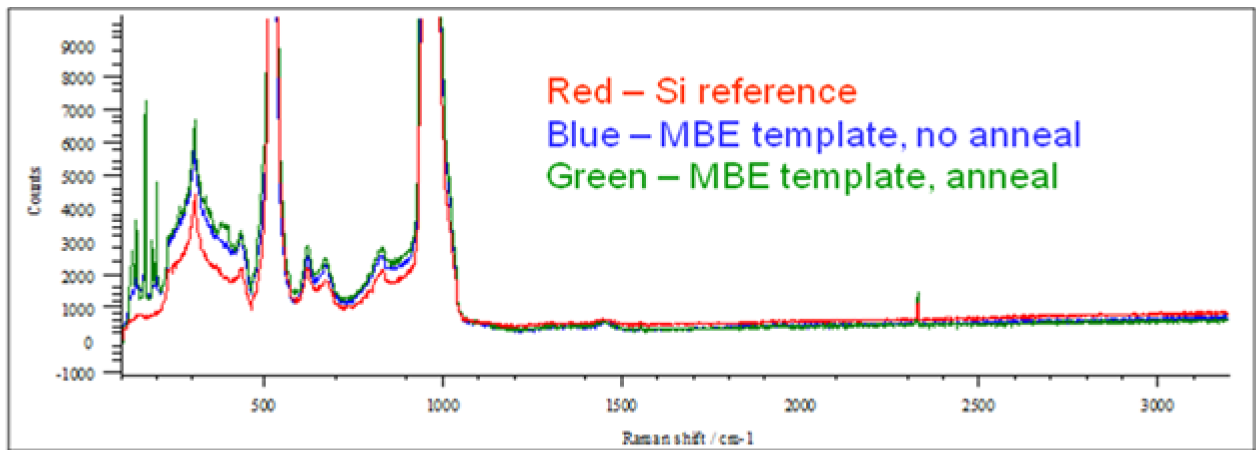

Figure 6.25 Micro Raman Spectroscopy of as-grown and annealed osmium silicide films MBE grown by the template method showing signature peaks in the region less than 500 cm^{-1} that are distinct from pure Si.

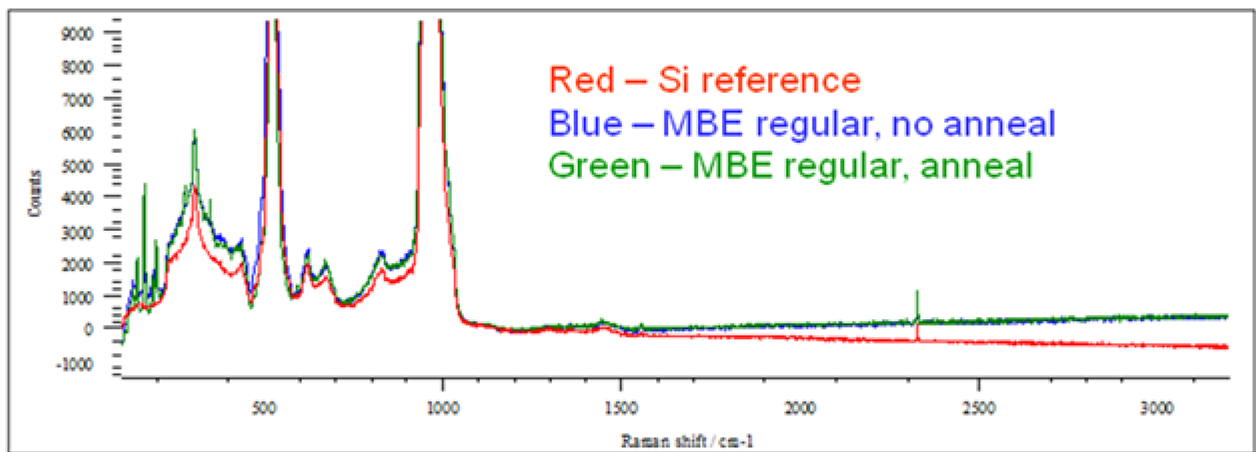

Figure 6.26 Micro Raman Spectroscopy of as-grown and annealed osmium silicide films MBE grown by the regular method showing active Raman shifts less than 500 cm^{-1} which are clearly different from those of pure Si.

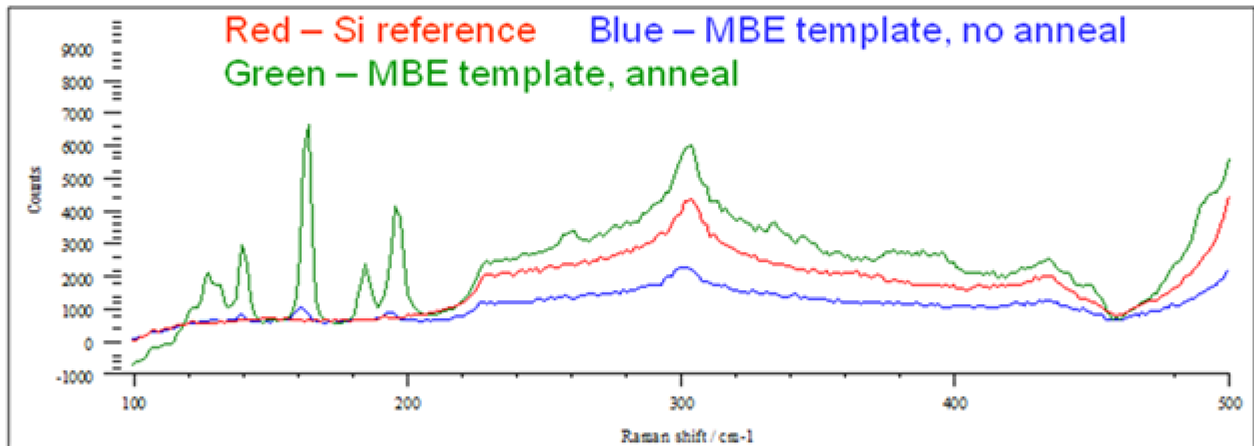

Figure 6.27 A clearer view of the Raman spectra at shifts less than 500 cm^{-1} of the as-grown and annealed osmium silicide films grown by the MBE template method. Annealing results in several sharp peaks at 126, 140, 162, 184 and 196 cm^{-1}. The peaks are significantly sharper – better film quality- in the annealed films grown by the template method in comparison with annealed ones grown by the regular method.

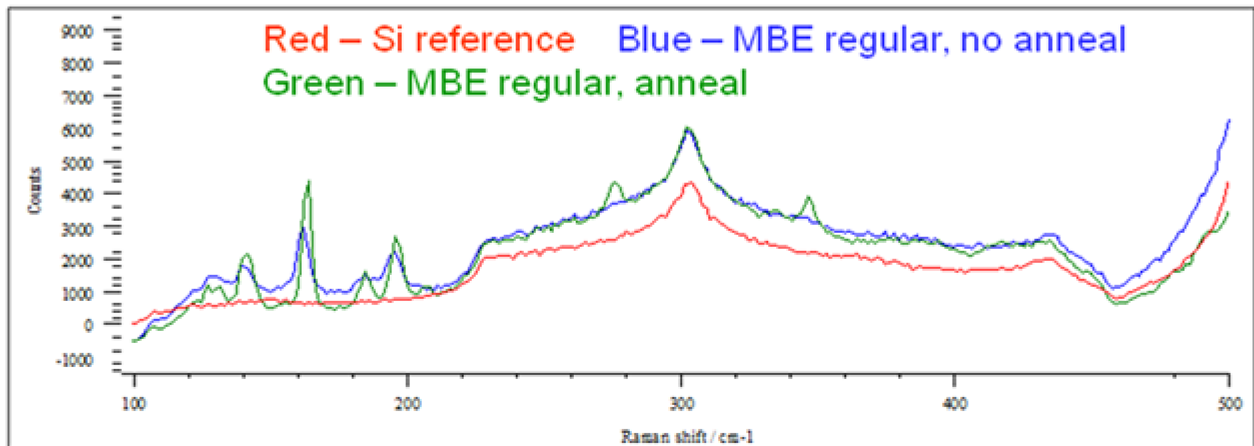

Figure 6.28 A clearer view of the Raman spectra at shifts less than 500 cm^{-1} of the as-grown and annealed osmium silicide films grown by the regular MBE method. The peaks of the annealed template-grown films appear in the regular-grown films in both the as-grown and the annealed. The sharp peaks are at 126, 140, 162, 184 and 196 cm^{-1}. The peaks of the as-grown films by the regular method are certainly sharper -better film quality- than the as-grown ones by the template method.

CHAPTER 7

A BIRD'S EYE VIEW AND SUMMARY OF CONCLUSIONS

7.1 Overview

While silicon is the material of choice for most of the semi-conductor industry applications due to its low cost and the immense amount semi-conductor industry processes that are available for its use in semi-conductor technology, the imperfection of silicon is the fact that it is not a direct band-gap semi-conductor, or else, it would have been the greatest and most perfect semi-conductor material. In order to bridge this gap, which is the motivation behind this work, what is ideally required is a Si-based material system where the band structure can be engineered and hetero-structures with tailorable offsets in both the valence and conduction bands can be realized. In other words, what is required is a semiconductor materials system that is based on Si, but has significantly greater versatility.

The one very road that has been little studied is the semi-conducting silicides material systems. The vast majority of silicides are metallic and not semi-conducting, most famous for their use as interconnects in silicon-based integrated circuits due to their thermal stability, low resistivity, and resistance to oxidation. Only around a dozen of them are semi-conducting. Many of these semi-conducting silicides have direct/quasi-direct band gaps. Table 1.1 shows all twelve semi-conducting silicides while grouping them based on similarities and iso-structural features of their crystal structure, space group, and lattice parameters.

Prior to this work, during phase I of the project, the focus was on group A in Table 1.1 and most heavily on the iron silicide material systems, its growth by molecular beam epitaxy and characterization, due to its reported band-gap of around 0.8 eV and prior reports of light

emission which makes it a promising candidate for opto-electronic applications see sections 1.1 and chapter 2 for more details and references.

The work presented in this dissertation is focused mainly on group C semi-conductor material systems of Table 1.1, which have been sparsely studied, namely, ruthenium silicide (Ru_2Si_3) and osmium silicide (Os_2Si_3) material systems. Also, important structural characterization of iron silicide is part of the scope of this work. It is worthwhile mentioning that the entirety of the work presented in this dissertation has been supported by the Office of naval Research (ONR) (Contract No. N00014-03-1-0820).

Chapter 1 pours heavily on the physics of this work, background, and motivation behind this study. Chapter 2 focuses on the foundation and theory of the electronic band structure, and presents the details of the band structure and band gaps of the silicides of choice. The theoretical foundation, physical premises, and methods of the growth and characterization techniques employed in this work are in chapter 3. Chapter 4 discusses the molecular beam epitaxial growth of iron silicon germanide and characterization by x-ray absorption spectroscopy, namely, x-ray absorption fine structure (XAFS). Chapter 5 dwells on the molecular beam epitaxial growth of diruthenium trisilicide by the MBE template method and its characterization using a variety of structural characterization techniques. Chapter 6 discusses in depth the attempted growth of osmium silicide by the MBE template method for the first time, to the best of our knowledge, and by the regular MBE growth method as well. This is together with an in-depth study of the structure and the pros and cons of both growth methods via various characterization methods.

7.2 Summary of Analysis

A brief summary of the conclusions can be briefly put together in the bulleted format below:

- The x-ray absorption fine structure spectroscopy study of the $Fe(Si_{1-x}Ge_x)_2$, ($0 \leq x \leq 0.15$) thin films grown by MBE show that the samples are not metallic and are in the β- $Fe(Si_{1-x}Ge_x)_2$ semiconducting phase, according to their nearest neighbor distances (d_{nn}) values, and their very close agreement with the d_{nn}'s of the *beta* semi-conducting phase. A slight yet noticeable increase in the absorption edge energy (E_0) values and a slight decrease in the nearest neighbor distances, with increased Ge deposits, were observed.
- Reflection High Energy Electron Diffraction (RHEED) intensity line profile analysis of MBE grown Ru_2Si_3 films shows that the lattice constant for Ru_2Si_3 film is twice that of Si. This result is consistent with known lattice constants for Si (5.43095 A), and orthorhombic Ru_2Si_3 (11.0 A^0). Also, RHEED patterns of the as-grown Ru_2Si_3 films indicate three-dimensional growth while the RHEED pattern of the annealed films show regaining of two-dimensional nature of film growth.
- *In situ* scanning tunneling microscopy (STM) of MBE grown diruthenium trisilicide films has been performed on the as-grown and annealed films. The STM images of the as-grown diruthenium trisilicide films show textured grains of around 0.5 µm in size. While, the STM images of the annealed films show a significantly smoother surface with smaller grains.

- *Ex situ* cross sectional scanning electron microscopy (X-SEM) measurements of as-grown and annealed diruthenium trisilicide films confirms the significant obvious difference between the hillock-like surface and structure of the as-grown film and the comparatively smoother surface of the annealed one. Quantitatively, this is illustrated by the thicknesses of the as-grown which range from 25 nm to 125 nm while the annealed thickness is about 40 nm.
- *Ex situ* atomic force microscopy (AFM) measurements indicate that the layers of the MBE grown diruthenium trisilicide clearly exhibit a granular structure. The as-grown film reveal a much more hillock-like structure and bigger grain sizes than the annealed one, with a RMS surface roughness of almost 23 nm. Whereas the annealed film clearly reveal a comparatively much smoother surface with a RMS surface roughness of less than 9 nm, and much smaller grain sizes.
- *Ex situ* x-ray photoelectron spectroscopy (XPS) measurements of the ruthenium silicide films show the ratio of ruthenium to silicon in the pre-sputtered as-grown and annealed films is a bit far from the desired stoichiometric ratio of 2:3 respectively. This, together with the oxygen presence and silicon dioxide binding energy peak, clearly indicate that very surface of the films have been oxidized, which is normal due to the exposure to atmospheric air. The good news is that the ratio of ruthenium to silicon in the post Argon (Ar)-sputtered as-grown and annealed films is in close agreement with the desired stoichiometric ratio of Ru_2Si_3. It is adequate to stress the fact that the Ar-sputtering is only around 30 A^0

deep, which confirms that the oxygen presence and oxidation in the pre-sputtered films is only on the very surface due to exposure to air.

- Micro Raman spectroscopy of Ru_2Si_3 reveals the active Raman shifts in the first 500 cm^{-1} presenting the signature oscillations and peaks of the diruthenium trisilicide. The active Raman shifts are at around 190, 220, 235, 370, and 485 cm^{-1}. It is worth noting that there is a clear distinction between the oscillation and their peaks between the diruthenium trisilicide films and the pure Si reference. Also, there is no difference that can be clearly seen between the peaks of the as-grown vs. the annealed films.
- RHEED of the osmium silicide grown films by the MBE template method show RHEED patterns before and after anneal that are to a greater extent identical to that of Ru_2Si_3 which is not surprising due to the fact that the MBE grown Ru_2Si_3 films are orthorhombic in structure and belong to the *Pbcn* space group, also Os_2Si_3 is orthorhombic and belong to the same space group. One can also see that the RHEED pattern of the as-grown and the annealed osmium silicide grown by both MBE methods is very different from the typical Si 2x1-reconstruction. It is evident that the as-grown films of both MBE methods exhibit three-dimensional growth behavior while the annealed ones seem to regain two-dimensional growth structure, given the streaked RHEED pattern in case of the annealed films vs. the dotty pattern in case of the as-grown.
- *In situ* scanning tunneling microscopy (STM) of the MBE grown osmium silicide films gives evidence that the as-grown and annealed films grown by the

template method have much more uniformity and crystalline pattern for the textured grains in the as-grown and the annealed, and better crystalline quality in general than the ones grown by regular MBE growth. *In situ* STM shows a clear hillock-like surface and structure with textured grains in the as-grown films by the template method. This hillock-like structure is sizably bigger, more ordered and uniform than in the as-grown films by the regular method. There is an obvious reduction in the size and height of the hillocks together with smaller grain sizes in the annealed films grown by the template method. Whereas the annealed films grown by the regular MBE method appear to have a much smoother surface and structure in comparison with the as-grown ones by the same method. However, uniformity and crystalline quality are still much more of a signature of the as-grown and annealed films grown by the MBE template method in comparison with the regular MBE method.

- *Ex situ* cross sectional scanning electron microscopy (SEM) of the osmium silicide films reveals a significant obvious difference between the hillocks of the as-grown film and the smooth surface of the annealed one, grown by both methods. Also, there is a clear interaction between the formed silicide by both MBE methods and the silicon below for the annealed films. Quantitatively, this is illustrated by the thicknesses of the as-grown films which range from 9 nm to 67 nm while the annealed thickness is about 46 nm.
- *Ex situ* AFM images of the MBE grown osmium silicide show less RMS surface roughness for the films grown by the regular MBE method than by the template

method. The template method annealed films yield a RMS surface roughness of 11.4 nm, while the regular method annealed films yield a 4.6 nm RMS surface roughness. The hillock-like surface and structure of the template method as-grown films still show more order and uniformity yet with bigger grains size and height than the regular method as-grown ones. However, it is clear that there is more order and uniformity, and a much smoother surface in the annealed films of the regular method.

- *Ex situ* XPS of the pre-sputtered osmium silicide films confirms that the very surface of the films have been oxidized due to exposure to air. The Si/Os fluxes were maintained at around 4 to obtain single phase Os_2Si_3 films according to results of prior work during phase I of this project, and XPS also reveals that the MBE template method and the regular MBE growth method yield percentages of osmium and silicon in the as-grown films that are very close to their flux ratios during growth, according to XPS results for both of the pre-sputtered, pre-sputtered (excluding oxygen) and post-sputtered films. I stress again that this is only seen in the as-grown films. However, in the annealed films, one can clearly see that both MBE methods yield a significant increase in the silicon percentages over the osmium ones, which means that the annealed films are very much silicon-rich. This may be attributed to the interaction of the silicide as-grown film with the silicon underneath as illustrated by the cross-sectional scanning electron microscopy (X-SEM) images of the annealed films.

- Micro Raman Spectroscopy of the MBE grown osmium silicide films shows that the regular MBE growth method clearly yields the signature peaks for the as-grown and the annealed films. These peaks are only clearly present in the annealed films grown by the template MBE method. This means that annealing the osmium silicide as-grown films by the template method enhances the overall film quality of the osmium silicide phase grown. It is worthwhile mentioning that these signature peaks are in the Raman shifts that are 500 cm^{-1} or less. The sharp signature peaks that define the phase grown are at 126, 140, 162, 184 and 196 cm^{-1}.

7.3 Summary of Conclusions

Fe-Si-Ge System:

(a) MBE growth of β- $Fe(Si_{1-x}Ge_x)_{2\ y}$ yields the semiconducting phase; not the metallic phase.

(b) The films do not contain agglomerated Fe.

(c) According to theoretical predictions, in Chapter 4, incorporating Ge into the lattice of β-$FeSi_2$, results in an increase of the lattice constant which leads to a reduction in its band gap with increasing Ge content

(d) Absorption edges (E_0) of β- $Fe(Si_{1-x}Ge_x)_2$ increases with increasing Ge content.

(e) While, nearest neighbor distances (d_{nn})decreases with increasing Ge content.

Ru-Si System:

(a) Annealing the Ru_2Si_3 thin films enhances the surface topology and roughness significantly and regains films 2-D growth.

(b) In terms of phase, crystalline quality, both as-grown and annealed films are similar.

(c) Ru_2Si_3 phase and stoichiometry are established by the MBE growth flux ratio and confirmed by RHEED pattern reconstruction and intensity profile, XPS and Raman active shifts.

Os-Si System:

(a) In terms of surface topology, morphology and roughness, certainly the MBE regular method yields better results for the annealed films only, yet as-grown films are broken into islands.

(b) In terms of periodicity, uniformity and crystalline quality and overall quality, the template yields better results for the as-grown and the annealed films.

(c) Os_2Si_3 phase and stoichiometry are established by the MBE growth flux ratio according to previous MBE reports and confirmed by the RHEED pattern reconstruction & the Raman Spectroscopy signature peaks.

7.4 Significance of Results and Future Implications

(a) Successful molecular beam epitaxial growth of orthorhombic Ru_2Si_3 phase and stoichiometry; the stable semi-conducting silicide in the Ru-Si system.

(b) Successful molecular beam epitaxial growth of orthorhombic Os_2Si_3 phase & stoichiometry.

(c) MBE has unique features: non-equilibrium technique, precise atomic control and full manipulation of growth conditions with extremely slow growth rates under UHV conditions.

(d) Ru_2Si_3 and Os_2Si_3 are very promising semi-conductors due to their direct band gaps for opto-electronic and multi-functional applications and the best of all; they are Si-based which means they can be easily integrated into Si technology.

(e) While the overall quality of the grown films has room for improvement, being able to grow them by MBE together with their promising features opens a wide world of exciting optimization to their growth quality together with optical, electrical and magnetic characterization.

(f) Ru_2Si_3 and Os_2Si_3 have a remarkable lattice match (0.6% max). Thus, this combination is extremely promising for at least reasonable heterostructures and super lattices and MBE can certainly do that.

(g) It is striking that Ru_2Ge_3 and Os_2Ge_3 are same crystal structure as their silicides counterparts not only suggesting that silicon/germanium heterostructure combinations would be achievable, but that within any system we could almost certainly alloy across the composition range; MBE can certainly do that too.

(h) But for MBE to do that, we had to grow these silicide phases & stoichiometries by MBE, determine the quality of the as-grown films vs. annealed, attempt the template technique and find out if it yields better quality films than the regular method.

(i) So, we can build on that for future optimization and growth of these

heterostructures, ternaries, and superlattices.

REFERENCES

(1) Cottier, R. J., Elmarhoumi, Nader M., Golding, Terry D. In *Joint Fall Meeting of the Texas and Four Corners Sections of the American Physical Society* El Paso, TX, 2008.

(2) Borisenko, V. E. *Semi-conducting Silicides*; Springer: Berlin, Germany, 2000.

(3) Mason, K.; Müller-Vogt, G. *Journal of Crystal Growth* **1983**, *63*, 34-38.

(4) Leong, D.; Harry, M.; Reeson, K. J.; Homewood, K. P. *Nature* **1997**, *387*, 686-688.

(5) Cottier, R. J. Dissertation, University of North Texas, 2009.

(6) Dusausoy, Y.; Protas, J.; Wandji, R.; Roques, B. *Acta Crystallographica Section B Structural Crystallography and Crystal Chemistry* **1971**, *27*, 1209-1218.

(7) Samsonov, G. V.; Vinitskii, I. M. In *Handbook of Refractory Compounds* IFI/Plenum, New York, 1979.

(8) Poutcharovsky, D. J.; Parthe, E. *Acta Crystallographica Section B* **1974**, *30*, 2692-2696.

(9) Maex, K.; Van Russum, M.; Reader, A. In *Properties of Metal Silicides* INSPEC, IEE, London, 1995, p 3-14.

(10) Engström, I. *Acta Chemica Scandinavica* **1970**, *24*, 2117-2125.

(11) Behar, M.; Bernas, H.; Desimoni, J.; Lin, X. W.; Maltez, R. L. *Journal of Applied Physics* **1996**, *79*, 752-762.

(12) Massalski, T. B.; Okamoto, H.; Subramanian, P. R. *Binary Alloy Phase Diagrams*; 2nd ed.; American Society for Metals: Metals Park, OH, 1990; Vol. 1-2.

(13) Schlesinger, M. E. *Chemical Reviews* **1990**, *90*, 607-628.

(14) Zephirov, A. P. *Thermodynamic Properties of Inorganic Matter* Moscow, Russia, 1965.

(15) Poutcharovsky, D. J.; Yvon, K.; Parthe, E. *J. Less-Common Met.* **1975**, *40*, 139-144.

(16) Fanciulli, M.; Rosenblad, C.; Weyer, G.; Von Kanel, H.; Onda, N.; Nevolin, V.; Zenkevich, A. In *Silicide Thin Films - Fabircation, Properties, and Applications*; Tung, R. T., Mason, K., Pellgrinni, P. W., Allen, L. H., Eds.; MRS: Pittsburgh, PA, 1996, p 319-324.

(17) Gallego, J. M.; Miranda, R. *Journal of Applied Physics* **1991**, *69*, 1377-1383.

(18) Baldwin, N. R.; Ivey, D. G. *Journal of Materials Science* **1996**, *31*, 31-37.

(19) Amesz, P. H.; Jorgensen, L. V.; Libezny, M.; Poortmans, J.; Nijs, J.; Van Veen, A.; Schut, H.; De Hosson, J. T. M. In *Silicide Thin Films - Fabircation, Properties, and Applications*; Tung, R. T., Mason, K., Pellgrinni, P. W., Allen, L. H., Eds.; MRS: Pittsburgh, PA, 1996, p 373-378.

(20) Cheng, H. C.; Yew, T. R.; Chen, L. J. *Journal of Applied Physics* **1985**, *57*, 5246-5250.

(21) Zhu, Q.-G.; Iwasaki, H.; Williams, E. D.; Park, R. L. *Journal of Applied Physics* **1986**, *60*, 2629-2631.

(22) Dimitriadis, C. A.; Werner, J. H. *Journal of Applied Physics* **1990**, *68*, 93-96.

(23) Borisenko, V. E.; Zarovskii, D. I.; Ivanenko, L. I. *Mikroelektronika* **1992**, *21*, 27-30.

(24) Radermacher, K.; Mantl, S.; Dieker, C.; Lüth, H.; Freiburg, C. *Thin Solid Films* **1992**, *215*, 76-83.

(25) Lau, S. S.; Feng, J. S. Y.; Olowolafe, J. O.; Nicolet, M. A. *Thin Solid Films* **1975**, *25*, 415-422.

(26) Alvarez, J.; de Parga, A. L. V.; Hinarejos, J. J.; de la Figuera, J.; Michel, E. G.; Ocal, C.; Miranda, R.; 4 ed.; AVS: Chicago, Illinois (USA), 1993; Vol. 11, p 929-933.

(27) d'Heurle, F. M. *Thin Solid Films* **1987**, *151*, 41-50.

(28) Petersson, C. S.; Baglin, J. E. E.; Dempsey, J. J.; d'Heurle, F. M.; La Placa, S. J. *Journal of Applied Physics* **1982**, *53*, 4866-4883.

(29) Donoval, D.; Stolt, L.; Norde, H.; Pires, J. d. S.; Tove, P. A.; Petersson, C. S. *Journal of Applied Physics* **1982**, *53*, 5352-5353.

(30) Gottlieb, U.; Laborde, O.; Rouault, A.; Madar, R. *Applied Surface Science* **1993**, *73*, 243-245.

(31) Chang, Y. S.; Chou, M. L. *Journal of Applied Physics* **1989**, *66*, 3011-3013.

(32) Ridley, B. K. *Quantum Processes in Semiconductors*; 2nd ed.; Clarendon Press: Oxford, Britain, 1988.

(33) Peyghambarian, N.; Koch, S. W.; Mysyrowicz, A. *Introduction to Semiconductor Optics*; Printice Hall: Englewood Cliffs, NJ, 1993.

(34) Klingshirn, C. F. *Semiconductor Optics*; Springer: Belin, Germany, 1995.

(35) Yu, P. Y.; Cardona, M. *Fundamentals of Semiconductor*; Springer: Berlin, Germany, 1996.

(36) *Density Functionals: Theory and Applications*; Springer: Berlin, Germany, 1998.

(37) Omar, M. A. *Elementary Solid State Physics: Principles and Applications*; Addison-Wesley, 1975.

(38) Kittel, C. *Introduction to Solid State Physics*; 6th ed.; Wiley, 2004.

(39) Pankove, J. I. *Optical Processes in Semiconductors*; Dover Publications: New York, NY, 1971.

(40) Filonov, A. B.; Migas, D. B.; Shaposhnikov, V. L.; Dorozhkin, N. N.; Petrov, G. V.; Borisenko, V. E.; Henrion, W.; Lange, H. *Journal of Applied Physics* **1996**, *79*, 7708-7712.

(41) Antonov, V. N.; Jepsen, O.; Henrion, W.; Rebien, M.; Stauss, P.; Lange, H. *Physical Review B (Condensed Matter and Materials Physics)* **1998**, *57*, 8934-8938.

(42) van Ek, J.; Turchi, P. E. A.; Sterne, P. A. *Physical Review B* **1996**, *54*, 7897-7908.

(43) Eppenga, R. *Journal of Applied Physics* **1990**, *68*, 3027-3029.

(44) Miglio, L.; Malegori, G. *Physical Review B* **1995**, *52*, 1448-1451.

(45) Miglio, L.; Meregalli, V. *Journal of Vacuum Science & Technology B: Microelectronics and Nanometer Structures* **1998**, *16*, 1604-1609.

(46) Ozvold, M.; Gasparik, V.; Dubnicka, M. *Thin Solid Films* **1997**, *295*, 147-150.

(47) Giannini, C.; Lagomarsino, S.; Scarinci, F.; Castrucci, P. *Physical Review B* **1992**, *45*, 8822-8824.

(48) Lefki, K.; Muret, P. *Journal of Applied Physics* **1993**, *74*, 1138-1142.

(49) Isoda, Y.; Okamoto, M. A.; Ohkoshi, T.; Nishida, I. A. In *Proceedings of the 12th International Conference on Thermoelectrics* Yokohama, Japan, 1993, p 192-196.

(50) Ware, R. M.; McNeill, D. J. *Electrical Engineers, Proceedings of the Institution of* **1964**, *111*, 178-182.

(51) Kojima, T. *physica status solidi (a)* **1989**, *111*, 233-242.

(52) Susz, C. P.; Muller, J.; Yvon, K.; Parthé, E. *Journal of the Less Common Metals* **1980**, *71*, P1-P8.

(53) Wolf, W.; Bihlmayer, G.; Blügel, S. *Physical Review B* **1997**, *55*, 6918-6926.

(54) Henrion, W.; Rebien, M.; Antonov, V. N.; Jepsen, O.; Lange, H. *Thin Solid Films* **1998**, *313–314*, 218-221.

(55) Filonov, A. B.; Migas, D. B.; Shaposhnikov, V. L.; Dorozhkin, N. N.; Borisenko, V. E.; Heinrich, A.; Lange, H. *Physical Review B* **1999**, *60*, 16494-16498.

(56) Vinning, C. B., Allevato, C. E In *10th International Conference on Thermoelectric Energy Conversion*; Babrow Press: Cardiff, 1991, p 167.

(57) Ohta, T., Vining, C. B., Allevato, C. E. In *26th Intersociety Energy Conversion Engineering Conference*; American Nuclear Society: La Grand Park, IL, 1991; Vol. 3, p 196-201.

(58) Schellenberg, L.; Braun, H. F.; Muller, J. *Journal of the Less Common Metals* **1988**, *144*, 341-350.

(59) Filonov, A. B.; Migas, D. B.; Shaposhnikov, V. L.; Dorozhkin, N. N.; Borisenko, V. E.; Lange, H. *Applied Physics Letters* **1997**, *70*, 976-977.

(60) Cho, A. Y. *Journal of Crystal Growth* **1995**, *150, Part 1*, 1-6.

(61) Marian, M. A., Sitter, H. *Molecular Beam Epitaxy: Fundamentals and Current Studies*; Springer-Verlag: Berlin, Germany, 1989.

(62) Oura, K., Lifshits, V.G, Saranin, A.A, Zotov, A.V, and Katayama, M. *Surface science: an introduction*; Springer-Verlag: Berlin, 2003.

(63) Golding, T. D. Dissertation, University of Cambridge, 1989.

(64) Ichimiya, A., Cohen, P. I. *Reflection High Energy Electron Diffraction*; Cambridge University Press: Cambridge, UK, 2004.

(65) Lytle, F. *Journal of Synchrotron Radiation* **1999**, *6*, 123-134.

(66) Prins, R. *X-ray Absorption: Principles, Applications, Techniques of EXAFS, SEXAFS & XANES*; Wiley, John & Sons, Inc., 1988.

(67) Sayers, D. E.; Stern, E. A.; Lytle, F. W. *Physical Review Letters* **1971**, *27*, 1204-1207.

(68) Bryant, P. J.; Miller, R. G.; Yang, R. *Applied Physics Letters* **1988**, *52*, 2233-2235.

(69) Cappella, B.; Dietler, G. *Surface Science Reports* **1999**, *34*, 1-104.

(70) Binnig, G.; Quate, C. F.; Gerber, C. *Physical Review Letters* **1986**, *56*, 930-933.

(71) Jandt, K. D. *Surface Science* **2001**, *491*, 303-332.

(72) Zhong, Q.; Inniss, D.; Kjoller, K.; Elings, V. B. *Surface Science Letters* **1993**, *290*, L688-L692.

(73) Gross, L.; Mohn, F.; Moll, N.; Liljeroth, P.; Meyer, G. *Science* **2009**, *325*, 1110-1114.

(74) Siegbahn, K.; Edvarson, K. *Nuclear Physics* **1956**, *1*, 137-159.

(75) Gardiner, D. In *Practical Raman Spectroscopy*; Gardiner, D., Graves, P., Eds.; Springer Berlin Heidelberg: 1989, p 1-12.

(76) Binnig, G.; Rohrer, H. *IBM J. Res. Dev.* **2000**, *44*, 279-293.

(77) Chen, C. J. *Introduction to Scanning Tunneling Microscopy*; Oxford University Press: Columbia University, New York, 2008.

(78) Bonnell, D. A. In *Scanning probe microscopy and spectroscopy: Theory, techniques, and applications* 2nd ed.; Wiley: New York, 2001.

(79) Bai, C. *Scanning tunneling microscopy and its applications*; Springer Verlag: New York, 2000.

(80) Abelev, E.; Sezin, N.; Ein-Eli, Y. *Review of Scientific Instruments* **2005**, *76*, -.

(81) Ardenne, M. *Zeitschrift für Physik* **1938**, *109*, 553-572.

(82) Tani, J.-i.; Kido, H. *Journal of Solid State Chemistry* **2002**, *169*, 19-23.

(83) Ishizaka, A.; Shiraki, Y. *Journal of The Electrochemical Society* **1986**, *133*, 666-671.

(84) Elmarhoumi, N. M., Cottier, R. J., Gregory, M., Roy, A., Geisler, H., Golding, Terry D., Ventrice, C. In *Texas Section of the American Physical Society* College Station, TX, 2007.

(85) Elmarhoumi, N. M., Cottier, R. J., Gregory, M., Roy, A., Geisler, H., Ventrice, C., Golding, Terry D. In *Joint Fall Meeting of the Texas and Four Corners Sections of the American Physical Society* El Paso, TX, 2008.

(86) Elmarhoumi, N. M., Cottier, R. J., Gregory, M., Roy, A., Geisler, H., Ventrice, C., Golding, Terry D. In *March Meeting of the American Physical Society* New Orleans, LA, 2008.

(87) Elmarhoumi, N. M., Cottier, R. J., Lohn, C., Gregory, M., Roy, A., Geisler, H., Ventrice, C., Golding, Terry D. In *2009 March Meeting of the American Physical Society* Pittsburg, PA, 2009.

(88) Lenssen, D.; Lenk, S.; Bay, H. L.; Mantl, S. *Thin Solid Films* **2000**, *371*, 66-71.

(89) Nan, S., Yi-huan, L. *Acta Physica Sinica* **1964**, *20*, 699-704.

(90) Cottier, R. J.; Amir, F. Z.; Zhao, W.; Hossain, K.; Gorman, B. P.; Golding, T. D.; Anibou, N.; Donner, W.; 3 ed.; AVS: 2006; Vol. 24, p 1488-1491.